Structure and Dynamics of Microcavity Exciton-Polaritons in Acoustic Square Lattices

D I S S E R TAT I O N

zur Erlangung des akademischen Grades

d o c t o r r e r u m n a t u r a l i u m

(Dr. rer. nat.)

im Fach Physik

eingereicht an der

Mathematisch-Naturwissenschaftlichen Fakultät

Humboldt-Universität zu Berlin

von

M. Sc. Jakov Buller

Präsidentin der Humboldt-Universität zu Berlin:

Prof. Dr.-Ing. Dr. Sabine Kunst

Dekan der Mathematisch-Naturwissenschaftlichen Fakultät:

Prof. Dr. Elmar Kulke

Gutachter:
(i) Prof. Dr. Henning Riechert
(ii) Prof. Dr. Oliver Benson
(iii) Dr. Dimitry Krizhanovskii

eingereicht am: 14.12.2017
Tag der mündlichen Prüfung: 13.07.2018

Abstract

Microcavity (MC) exciton-polaritons can form condensates, i.e. macroscopic quantum states (MQSs), as well under a periodic potential modulation. The modulation by a surface acoustic wave (SAW) provides a powerful tool for the formation of tunable lattices of MQSs in semiconductor microcavities. The modulation of MQSs by a SAW arises from the change of the excitonic bandgap energy and the thickness of the sample structure layers induced by the strain fields of the SAW. The frequency of the acoustic modulation of MQSs is limited by the thickness of the upper distributed Bragg reflector (DBR) of the MC. The MQSs were resonantly excited in an optical parametric oscillator configuration. In this work, fundamental aspects regarding the structure and the dynamics of exciton-polariton condensate in acoustic square (2D) lattices were investigated by probing its wavefunction in real- and momentum space using spectral- and time-resolved studies.

The tomographic study revealed that the exciton-polariton condensate structure excited by a Gaussian laser beam self-organise in a concentric structure, which consists of a single, two-dimensional gap soliton (2D GS) surrounded by one-dimensional (1D) MQSs with lower energy. While the size of the 2D GS tends to saturate with increasing particle density, the emission region of the surrounding 1D states increases. The existence of these MQSs in acoustic lattices is quantitatively supported by a theoretical model based on the variational solution of the Gross-Pitaevskii equation. The formation of the 1D states in a ring around the central 2D GS is attributed to the energy gradient in this region, which reduces the overall symmetry of the lattice.

Time-resolved studies clearly showed the evolution of the 2D GS wavefunction at the acoustic velocity. Interestingly, the photoluminescence (PL) intensity emitted by the 2D GS as well as its coherence length oscillate with the position of the acoustic lattice sites relative to the exciting laser beam. The coherence length and the PL intensity are correlated. The PL oscillation amplitude depends on both the intensity and the size of the exciting laser spot, and increases considerably for excitation intensities close to the optical threshold power for the formation of the MQS. The oscillations are explained by a model that takes into account the combined effects of SAW reflections, which dynamically distort the amplitude of the potential, and the spatial phase of the acoustic lattice within the exciting laser spot.

In the outlook, the formation of Tamm-Plasmon/Exciton-Polariton (TPEP) hybrid states and their modulation by SAWs was theoretically discussed. Here, the upper DBR is partly replaced by a thin metal layer placed on top of the MC. In this case, TPEP form by the superposition of Tamm plasmons at the metal-semiconductor interface and the exciton-polaritons in the MC. This technique enables one (i) to create potential barriers of several meV and (ii) to modulate exciton-polaritons or TPEP by SAWs at higher frequencies.

Keywords: exciton-polariton, macroscopic quantum states, condensation, surface acoustic waves, tomographic measurements, time-resolved, Tamm plasmon

Zusammenfassung

Exziton-Polaritonen in Mikrokavitäten sind Quasi-Teilchen, die unter bestimmten physikalischen Konditionen kondensieren und damit in einen energetisch gleichen, gemeinsamen makroskopischen Quantenzustand (MQZ) übergehen können. Es ist möglich, die Exziton-Polariton-Kondensate mithilfe von akustischen Oberflächenwellen zu modulieren und dadurch ihre Eigenschaften zu ändern. Dies ist insbesondere im Hinblick auf die möglichen Anwendungsbereiche von Exziton-Polaritonen von bedeutender Relevanz. Akustische Oberflächenwellen bieten den Vorteil, dass die durch sie erzeugte Modulation dynamisch ist und dass die Modulationsstärke durch die Amplitude der Oberflächenwelle kontrolliert werden kann. Die Frequenz der akustischen Modulation ist durch die Dicke des oberen Bragg-Spiegels der Mikrokavität bestimmt. In dieser Arbeit wurden die fundamentalen Aspekte bezüglich der Struktur sowie der Dynamik der Exziton-Polariton-Kondensate in den durch die akustischen Oberflächenwellen erzeugten quadratischen Gittern experimentell untersucht. Es wurde dazu die Wellenfunktion der Exziton-Polariton-Kondensate im Rahmen der spektroskopischen und zeitaufgelösten Messungen im Orts- und Impulsraum abgebildet. Die MQZ wurden in einer optisch-parametrischen Oszillatorkonfiguration resonant angeregt. Um die gewonnenen experimentellen Ergebnisse qualitativ zu erklären, wurden theoretische Modelle entwickelt.

Die spektroskopischen Messungen zeigten, dass Exziton-Polariton-Kondensate in akustischen quadratischen Gittern aus unterschiedlichen MQZ, nämlich aus einem zwei-dimensionalen Gap-Soliton (2D GS) umgeben von mehreren ein-dimensionalen (1D) MQZ, und einem inkohärenten Strahlungshintergrund zusammengesetzt sind. 2D GS befindet sich in einem energetisch höheren Zustand als 1D MQZ. Die Größe des 2D GS steigt mit der Anregungsleistung bis zu einem bestimmten Sättigungswert und ist danach unabhängig von dieser, während 1D MQZ keinen Größensättigungswert zeigen.

Im Rahmen der zeitaufgelösten Experimente wurde die Dynamik der Wellenfunktion des 2D GS untersucht. Die zeitaufgelösten Ergebnisse zeigten, dass sowohl die Intensität der von dem 2D GS emittierten Photolumineszenz (PL) als auch die Kohärenzlänge des 2D GS zeitlich oszillieren. Die Intensität der PL und die Kohärenzlänge hängen von der Anregungsleistung, der Größe des Laserspots sowie von der relativen Position des akustischen Gitters und dem Laserspot ab.

Im Ausblick dieser Arbeit wurde theoretisch die Anregung von Tamm-Plasmon/Exziton-Polaritonen (TPEP) sowie deren Modulation mithilfe von akustischen Oberflächenwellen diskutiert. TPEP entstehen durch die Superposition der in der Grenzschicht zwischen Mikrokavität und Metall angeregten Tamm-Plasmonen und den in der Mikrokavität erzeugten Exziton-Polaritonen. Zur Anregung von Tamm-Plasmonen muss eine dünne Metallschicht auf die Mikrokavität angebracht werden, dies ermöglicht es (i) Potentialbarrieren für Exziton-Polaritonen von mehreren meV zu erzeugen und (ii) die Dicke des oberen Bragg-Spiegels der Mikrokavität zu reduzieren, sodass die akustische Modulation von Exziton-Polaritonen bzw. TPEP im höheren Frequenzbereich erreicht werden kann.

Stichwörter: Exziton-Polariton, makroskopische Quantenzustände, Kondensation, akustische Oberflächenwellen, Spektroskopie, zeitaufgelöst, Tamm-Plasmon

Acknowledgment

First, I would like to thank everyone for the support, which I have received during my time in the Paul Drude Institute, without you all my work would not have been possible! It was a great time and I will always keep it in memory. I have learned a lot, not only professionally but also a lot about myself, which is priceless.

Especially, I would like to thank Dr. P. V. Santos, Dr. E. A. Cerda-Méndez and Prof. Dr. H. Riechert. I am really thankful for have been given the opportunity to be part of the Paul Drude Institute and to carry out my research in such a great environment. Thank you for giving me the great conditions to work on this thesis. Not every student has such good equipment in the lab. Not every student gets to visit as many conferences as I could.

Dr. P. V. Santos and Dr. E. A. Cerda-Méndez, I would like to thank you for guidance and for showing me day by day what it means to be a scientist: the exactness and the patience, the enthusiasm and the joy of discovering the truth, I hope to keep all of this in myself. Thank you very much for introducing me to the vast and fascinating field of exciton-polaritons. Thank you very much for the fruitful discussions we had, for your insight and your eye for the detail.

I would like to thank Dr. O D. D. Couto Jr. and Dr. R. E. Balderas-Navarro for their great support during my first year. I wish we could have discussed and worked together longer.

Dr. K. Biermann, thank you very much for growing the samples! Also, I would like to thank A. Tahraoui, S. Rauwerdink, W. Seidel and B. Drescher for sample processing. Without your work, my thesis would not have been possible.

I would like to thank Dr. A. Hernández-Mínguez and Colin M. Hubert for their great insight into the topic of surface acoustic waves, excitons and indirect excitons. Thank you for answering my many questions, your support and all the useful, knowledgeable discussions.

Finally, I would like to thank a lot my family and my friends! Thank you very much for your support, your wise and motivational words guided me through good and difficult times. Mom and Dad, thank you for arouse my interest in science!

Statement of Originality

I declare that I have completed the thesis independently using only the aids and tools specified. I have not applied for a doctor's degree in the doctoral subject elsewhere and do not hold a corresponding doctor's degree. I have taken due note of the Faculty of Mathematics and Natural Sciences PhD Regulations, published in the Official Gazette of Humboldt-Universität zu Berlin no. 126/2014 on 18/11/2014.

I certify that the intellectual content of this thesis is the product of my own work and that all the assistance received in preparing this thesis and sources have been acknowledged.

Jakov (V. T.) Buller

List of publications

Publications of parts of this work

J. V. T. Buller, E. A. Cerda-Méndez, R. E. Balderas-Navarro, K. Biermann and P. V. Santos, *Spatial self-organization of macroscopic quantum states of exciton-polaritons in acoustic lattices*, New J. Phys. **18**, 073002 (2016)

J. V. T. Buller, E. A. Cerda-Méndez, R. E. Balderas-Navarro, K. Biermann and P. V. Santos, *Exciton-polariton gap soliton dynamics in moving acoustic square lattices*, Phys. Rev. B **94**, 125432 (2016)

J. V. T. Buller, E. A. Cerda-Méndez, R. E. Balderas-Navarro, K. Biermann and P. V. Santos, *Dynamical and Tuneable Modulation of Tamm-Plasmon/Exciton-Polariton Hybrid States using Surface Acoustic Waves Source*, Acta Physica Polonica A **129**, A-26 (2016)

Further publications

C. Chèze, M. Siekacz, F. Isa, B. Jenichen, F. Feix, J. Buller, T. Schulz, M. Albrecht, C. Skierbiszewski, R. Calarco and H. Riechert, *Investigation of interface abruptness and In content in (In,Ga)N/GaN superlattices*, J. Appl. Phys. **120**, 125307 (2016)

H. Zimmermann, J. Buller, S. Eilzer and U. Eichmann, *Strong-Field Excitation of Helium: Bound State Distribution and Spin Effects*, Phys. Rev. Lett. **114**, 123003 (2015)

Conference presentations

J. V. T. Buller, R. E. Balderas-Navarro, K. Biermann, E. A. Cerda-Méndez and P. V. Santos, *Probing the dynamics of self-localised exciton-polariton condensates in moving 2D lattices*, Spring Meeting of the German Physical Society (DPG), Regensburg (Germany), March 2016

J. V. T. Buller, E. A. Cerda-Méndez, R. E. Balderas-Navarro, K. Biermann and P. V. Santos, *Structure and temporal dynamics of exciton-polariton condensates in acoustic 2D lattices*, International Conference on Optics of Excitons in Confined Systems, Jerusalem (Israel), October 2015

J. V. T. Buller, J. Chana, E. A. Cerda-Méndez, R. E. Balderas-Navarro, K. Biermann, F. Fras, D. N. Krizhanovskii, M. S. Skolnick and P. V. Santos, *Temporal*

dynamics of polariton condensates in acoustic lattices, 17th International Conference on Modulated Semiconductor Structures, Sendai (Japan), July 2015

J. V. T. Buller, E. Cerda-Méndez, R. Balderas-Navarro, K. Biermann and P. V. Santos, *Dynamical modulation of Tamm-plasmon/exciton-polariton hybrid states using surface acoustic waves*, 44th "Jaszowiec" Conference on the Physics of Semiconductors, Wisla (Poland), June 2015

J. V. T. Buller, E. A. Cerda-Méndez, R. E. Balderas-Navarro, K. Biermann, D. N. Krizhanovskii, M. S. Skolnick and P. V. Santos, *Structure of polariton macroscopic quantum phases in 2D acoustic lattices*, Spring Meeting of the German Physical Society (DPG), Berlin (Germany), March 2015

J. V. T. Buller, E. A. Cerda-Méndez, R. Balderas-Navarro, K. Biermann, D. Sarkar, D. N. Krizhanovskii, M. S. Skolnick and P. V. Santos, *Momentum and real space tomography of exciton-polaritons gap solitons in 2D lattices*, International School on the Physics of Indirect Excitons, Erice (Italy), July 2014

J. V. T. Buller, O. D. D. Couto Jr., E. A. Cerda-Méndez, S. Rauwerdink, A. Tahraoui and P. V. Santos, *Design and fabrication of acoustic devices in ZnO/SiO2 planar microcavities*, Spring Meeting of the German Physical Society (DPG), Dresden (Germany), April 2014

Abbreviations

1D	one-dimensional
2D	two-dimensional
CCD	charge-coupled device
cw(-PL)	continuous-wave (photoluminescence)
FWHM	full width at half maximum
2D GS	gap soliton
IDT	interdigital transducer
LP	lower polariton branch
MBE	molecular beam epitaxy
MBZ	mini-Brillouin zone
MQS	macroscopic quantum state
OPO	optical parametric oscillator
PL	photoluminescence
QW	quantum well
RF	radio-frequency
SAW	surface acoustic wave
TPEP	Tamm-Plasmon/Exciton-Polariton hybrid state
UP	upper polariton branch

List of main symbols

Symbol	Name	Unit
c	speed of light in the medium	$m\,s^{-1}$
ΔE_{blue}	blue-shift energy	eV
E_G	bandgap energy	eV
E_{kin}	kinetic energy	eV
E_{pot}	potential energy	eV
E_X	exciton energy	eV
f_{SAW}	surface acoustic wave frequency	s^{-1}
f_X	exciton oscillator strength	
Φ_{SAW}	surface acoustic wave potential	eV
g	exciton-polariton interaction constant	$10\,\mu eV\,\mu m^2$
$I_{PL(T)}$	(time-resolved) photoluminescence	
k	wavevector or reciprocal space vector	m^{-1}
L_{coh}	coherence length	m
λ_C	microcavity resonance wavelength	m
λ_{SAW}	surface acoustic wave wavelegth	m
m_e	electron rest mass (9.109×10^{-31})	kg
m^*	(exciton-polariton) effective mass	m_e
m_X	reduced exciton mass	kg
n	refractive index of the medium	
P_L	laser power	W
P_{th}	condensation threshold	W
P_{RF}	surface acoustic wave power	W
$\hbar\Omega$	Rabi-splitting energy	eV
T	temperature	K
τ	lifetime	s
Q	microcavity quality factor	

List of Figures

List of Tables

Contents

Chapter 1

Introduction

In the past two decades, a new type of a two-dimensional half-light half-matter system called microcavity (MC) exciton-polaritons (in the following shortly polaritons) has emerged. Polaritons can exhibit spontaneous coherence and thus, undergo condensation. Polariton condensates show similar properties like Bose-Einstein condensates (BEC) known from atomic systems. However, there are some differences. In contrast to atomic BEC, polaritons are bosonic quasi-particles, which have a short lifetime of only a few picoseconds. The origin of this lies in their photonic component. Due to their short lifetime, polariton condensates possess an inherently non-equilibrium nature. This may be seen as a disadvantage at first glance. On the other hand, a MC polariton system is a unique one, which enables one to study condensation processes and related phenomena like superfluidity, superradiance, entanglement, vortex formation, BKT (Berezinskii-Kosterlitz-Thouless) and BCS (Bardeen-Cooper-Schrieffer) physics in semiconductors. In addition to the study of the fundamental physical questions, all these properties make them promising candidates for various future quantum device applications.

Nowadays, polaritons are on the forefront of the research in the solid state physics. They are rich in fundamental physics and their intriguing potential applications are the reason that has attracted the attention of several research groups around the world. And it is forecasted that already in the coming decade a new generation of opto-electronic devices based on MC polaritons will appear. Recently, breaking through concepts have been realised, which include polariton-based light-emitting diodes, lasers and transistors. For example, polariton-based lasers are a new type of ultra-low threshold coherent light-sources (lasers without a population inversion), whereas polariton-based transistors should make it possible to design and build integrated optical circuits operating at higher frequencies than conventional electronic ones. One of the reasons that these concepts could be realised is the fast developments in the fabrication and processing of MC structures and the rapid progress in crystal growth techniques. The quality of the MC plays a central role for realisation of MC polaritons. Another important parameter in polariton-based devices and/or functionalities, which needs to be mentioned, is the ability to apply a controllable and, desirably, a tuneable modulation of polaritons as well as to be able to guide

or even to trap them. The latter may lead to the formation of low-dimensional polariton condensates and discrete polaritonic modes. The use of well-defined lattice potentials opens a way to study polariton coherence changes, polariton-polariton interactions as well as the interactions among several condensates or even to create different types of condensates as will be discussed later in this work.

MC polaritons can be modulated by modifying their photonic and/or excitonic component. One promising way to do so, is to pattern the MC surface structure by placing thin semi-transparent metal disk layers, which changes first the total MC thickness and second its optical transmission. In this way, the photonic component is modulated. However, although it is a promising way and also a way, which enables the formation of interesting and worth studying Tamm-Plasmon/Exciton-Polariton hybrid states as will be discussed in the outlook of this thesis, it has its disadvantages. For example, the modulation potential set by the metal thickness is fixed and not tuneable. This disadvantage can be overcome if surface acoustic waves (SAWs) are used. SAWs are periodic mechanical vibrations, which propagate along the MC surface carrying strain-induced fields and thus, creating periodic lattice potentials for MC polaritons. Their strain field modulates mainly the excitonic component of MC polaritons. SAWs can be generated using interdigital transducers (IDTs), a technology, which has been being available for several decades. The SAW lattice potential is tuneable and set by the SAW power. In addition, the SAW wavelength determines the periodicity of the lattice potential. The fabrication of IDTs for SAWs with wavelengths in the range of a few micrometres is easily possible using the optical lithography techniques, whereas smaller wavelength, i.e. in the nanometre range, can be realised using e-beam lithography. Nowadays, using the latter technique, SAWs with wavelengths of only a few hundreds of nanometres can be generated using IDTs. SAWs can be applied along several crystallographic directions on the MC and thus, different lattice geometries can be introduced to polaritonic systems. For instance, in a trigonal acoustic lattice the possibility is given to form topological insulating polariton states. The topic of typological insulators is a strongly up-rising research field. SAWs are a powerful tool to create artificial potentials and therefore, they are ideal candidates to apply modulation potentials to MC polaritons, which will be used in this work.

Recently, in 2013 Edgar A. Cerda-Méndez *et al.* have experimentally demonstrated that MC polaritons in two-dimensional (2D) shallow potentials can form spatially self-localised macroscopic quantum states (MQSs), where the MQSs occupy a single energy state within the dispersion bandgap. Furthermore, these polariton states show analogies to the gap solitons well-known from nonlinear photonic crystals and atomic BEC in optical lattices and, therefore, they have been dubbed as exciton-polariton gap solitons (2D GS). Interestingly, polaritons in 2D GS are not in the ground state, they are in an energetically excited state with a momentum at a well-defined value far away from the centre of the Brillouin zone. Similar results have been reported in the same year by D. Tanese *et al.*
2D GS properties open the way for the realisation of novel topological phases and other polariton quantum phases such as a Bose glass. They are foreseen as a building

block for polaritonic circuits, where polariton propagation and localisation can be controlled as well as reconfigured by the optical excitation power and the lattice potential amplitude.

However, some fundamental questions related to 2D GS physics remained unanswered, which are the subject of this work. The main open questions regard the dependence of the 2D GS formation and their number within the excitation area on the optical power as well as the temporal dynamics of the 2D GS wavefunction in acoustic 2D lattices. In order to answer the first question, a tomography-like technique was applied to spectrally resolve the 2D GS structure. This is the topic of the Chapter 4 Section 2 and will be discussed there in detail. Time-resolved studies have been additionally performed to investigate the temporal evolution of the 2D GS wavefunction. For that purpose, a streak-camera with a temporal resolution of 50 picoseconds was used. The corresponding results are presented in Chapter 4 Section 3. The experimental results are summerised in Chapter 5. In Chapter 6 an outlook is given, where the formation and SAW mediated modulation of hybrid states between Tamm plasmons and exciton-polaritons is discussed.

Chapter 2

Theoretical background

In this chapter the theoretical background of this work is presented in a detailed and brief form. Microcavity exciton-polaritons are quasi-particles, which result from strong light-matter interactions in a semiconductor, thus first the concept of quasi-particles, i.e. excitons, is discussed, followed by the discussion of semiconductor microcavities, which have the purpose to confine light and to enhance its electric field next to the excitons in order to increase the light-matter interactions and to strongly couple excitons and photons. Furthermore, this chapter gives an overview of surface acoustic waves and how their potential is used to coherently modulate microcavity exciton-polaritons and exciton-polariton condensates. The structure of the investigated sample is aslo presented in this Chapter.

2.1 Wannier-Mott exciton as a matter particle for creating polaritons

A solid-state system, such as a semiconductor, consists of trillion of trillion atoms per cm^3. It consists only of protons, neutrons and electrons. Since a solid-state system is a very large system, it is impossible to describe e.g. the interactions of these particles in detail. However, instead of treating all atoms, it is convenient to see the ground state of the solid-state system as a quasi-vacuum, where elementary excitations are described by quasi-particles.
The quasi-vacuum of an intrinsic semiconductor is the state with a filled valence band and an empty conduction band. A semiconductor is a material whose energy bandgap E_G for electronic excitations lies between 0 and a few eV [1], [2]. The best known semiconductor is silicon (Si). However, a large number of elements and compounds have semiconducting properties. One of them is *gallium arsenide* (GaAs), which is the chosen material for the studies of this work. One of the many advantages of GaAs is its direct bandgap that allows electrons to be excited from the valence band to the conduction band by keeping the same crystal momentum (k) in the Brillouin zone. Thus, an electron in GaAs can directly absorb and/or emit a photon. The energy bandgap E_G of GaAs is 1.4 eV at 300 K for the Γ-valley.

The temperature dependence of E_G of GaAs for the Γ-valley is given by [3]:

$$E_G(T) = 1.519\,eV - \frac{5.405\,\frac{eV}{K} \times 10^{-4}\,T^2}{T + 204\,K}. \tag{2.1.1}$$

A typical quasi-particle in a semiconductor is an *exciton*. An exciton is created when a photon, whose energy corresponds to or lies above E_G, is absorbed in the semiconductor. In this case, an electron with the charge -e is excited from the valence band into the conduction band. The excited electron leaves a vacancy in the valence band, which can be described by the quasi-particle "hole". The hole has the charge $+e$ and an effective mass m_h^* given by $m_h^* = \hbar^2 \left(d^2E/dk^2\right)^{-1}$, i.e. dispersion of the hole, where E is the energy and k the crystal momentum of the hole, respectively. Since the excited electron and the hole have opposite charges, they are bound by the electrostatic Coulomb force F_C. This bound state is the exciton. It has a dipole moment and is electrically neutral. The Bohr-radius a_B of an exciton is determined by F_C and, considering the large dielectric constant of semiconductors, is on the order of 150 $\mathring{A}$ for GaAs, extending over many unit cells of the crystal [4], [5]. This type of the exciton is called Wannier-Mott exciton and is used in this work.
The most relevant properties of the exciton for this work are its effective mass, its energy and its oscillator strength describing the interaction of the exciton with light, i.e. electromagnetic fields. Most importantly, excitons are composite bosons with a radiative lifetime on the order of 10^{-9} s [6]. As will be discussed later, under right conditions these properties allow one to form exciton-polariton condensates.

In a simple picture, when only an electron and a hole are considered, the Schrödinger equation of the exciton reads:

$$\left(-\frac{\hbar^2}{2m_e^*}\nabla_e^2 - \frac{\hbar^2}{2m_h^*}\nabla_h^2 - \frac{e^2}{4\pi\varepsilon_0\epsilon\,|\mathbf{r}_e - \mathbf{r}_h|}\right)\Psi = E\,\Psi, \tag{2.1.2}$$

where m_e^* and m_h^* are the effective masses of the electron in the conduction band and the hole in the conduction and valence bands, respectively. ϵ is the dielectric constant of the semiconductor and $\mathbf{r}_e$ and $\mathbf{r}_h$ are the coordinates of the electron and hole, respectively. m_e^* and m_h^* arise from the periodic potential of the remaining electrons and cores in the valence band. In GaAs, the electron in the Γ-valley has $m_e^* = 0.063\,m_e$ and the (heavy) hole $m_h^* = 0.51\,m_e$, where m_e is the mass of a free electron.
The solution of the above Schrödinger equation yields the free exciton wavefunction:

$$\Psi = \frac{1}{\sqrt{V}} e^{i\mathbf{k}\cdot\mathbf{R}} F\left(r_{e-h}\right), \tag{2.1.3}$$

where $\mathbf{k}$ is the crystal momentum vector, V is the crystal volume, $F\left(r_{e-h}\right)$ denotes a function describing the relative motion of both particles and $\mathbf{R}$ gives the coordinates of the centre-of-mass of the exciton. The total energy E_X of the exciton in bulk is:

$$E_X = E_G + \frac{\hbar^2 k^2}{2(m_e^* + m_h^*)} - \frac{\mu_X\,Ry}{m_e\,n^2\,\epsilon^2}, \tag{2.1.4}$$

where the second term represents the kinetic energy E_{kin} of the exciton and third term represents the exciton binding energy E_B, which depends on the principle number n in analogy to Rydberg states of atoms [2]. Ry is the Rydberg energy and m_X is the reduced exciton mass, i.e. $m_X = (1/m_e^* + 1/m_h^*)^{-1}$. Note, the binding energy E_B of the 1S exciton, i.e. $n = 1$, in GaAs is $4\,meV$. Thus, the GaAs exciton is only stable at low temperatures, i.e. where the thermally induced fluctuations, i.e. $\propto k_B T$, are smaller than E_B.

2.1.1 Oscillator strength

Since an electron and a hole have opposite electrical charges, an exciton is a dipole that interacts with electromagnetic fields of light. The strength of this interaction with light of frequency f is given by the exciton oscillator strength f_X [7]:

$$f_X \propto m_X\, f\, |\langle\psi_e|\, \mathbf{d}\, |\psi_h\rangle|^2 \left(\pi a_B^3\right)^{-1}, \tag{2.1.5}$$

where ψ_e and ψ_h are the electron and hole wave functions, respectively, and $\mathbf{d}$ is the exciton dipole moment. The term $(\pi a_B^3)^{-1}$ reflects the increase of the exciton-light interaction in comparison to the interaction between light and the unbound pair of the electron and hole. The probability of an optical transition for exciton is increased since the electron and hole have an averaged relative separation of a_B in comparison to their unbound state. Thus, the oscillator strength f_X results from the overlap of the electron and hole wave functions. The oscillator strength f_X plays an important role in the creation of exciton-polaritons since a strong f_X favours the strong coupling between excitons and photons. A way to enhance f_X is to increase the electron and hole wavefunctions overlap by spatial confinement, e.g., in quantum wells.

2.1.2 Quantum well (QW) excitons

A semiconductor quantum well (QW) is a thin layer of the thickness d, which is sandwiched between two layers of a material with a bigger energy bandgap, e.g. *aluminium arsenide* (AlAs) around a GaAs QW (cf. Fig. 2.1). The thickness of the QW is usually smaller than the exciton Bohr-radius a_B^{3D} in bulk forcing the excitons to have a smaller Bohr-radius a_B^{2D} that is determined by the QW thickness. Consequently, the oscillator strength of QW excitons is enhanced by a factor $\left(a_B^{3D}/a_B^{2D}\right)^3$.
A QW provides a potential well for the excitons and confines them in one spatial direction. Consequently, QW excitons can be considered as 2D quasi-particles. Due to momentum conservation they couple only to light with the same planar momentum $k_{||}$.

The total energy of the 1S exciton, i.e. $n = 1$, in a $15\,nm$ GaAs QW at $10\,K$ (experimental conditions) is $1.54\,eV$ corresponding to the wavelength of light of $805\,nm$.

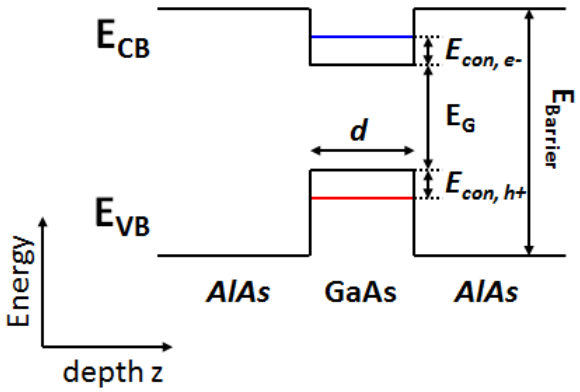

Figure 2.1: Schematic representation of a quantum well (QW) potential - a GaAs QW with the thickness d is placed between two AlAs layers with a larger energy bandgap $E_{Barrier}$. The electron and hole energies are influenced by the GaAs QW thickness d, i.e. $E_{con,\,e^-/h^+}$ is a function of d.

Additionally, to enhance in the exciton-light interactions, it is necessary to increase the overlap of light fields with the excitons, i.e. to confine the light field close to the QW. As discussed in the next Section, this is achieved by the use of semiconductor microcavities.

Remarks

For this work only the heavy hole, i.e. a hole with the total angular momentum $J = \pm\frac{3}{2}$, is considered. Thus, there was previously no discussion about the types of holes, i.e. heavy and light holes, and their differences. For more information on this topic, the reader is referred to the corresponding literature, e.g. Ref. [8] and [9]. The confinement energy for the light hole exciton in a $15\,nm$ thick GaAs QW is approximately $20\,meV$ higher than for the heavy hole. Comparing this result to the thermal energy $\propto k_B T$ and following the Boltzmann distribution of statistical mechanics, i.e. probability distribution of particles in a system of various possible states, one finds that the thermal occupation of the light hole state is negligible for temperatures well below $50\,K$ (cf. Fig. 2.2). Hence, when the measurements are performed at lower temperatures - the measurements were carried out at $8\,K$ for this work - the light hole excitons can be neglected.

2.2 Semiconductor microcavities

Semiconductor microcavities play an important role in the nowadays semiconductor technology. Novel device concepts like VCSELs [10], [11], polariton-based lasers [12], [13] and polariton-based transistors [14] could not have been probably realised

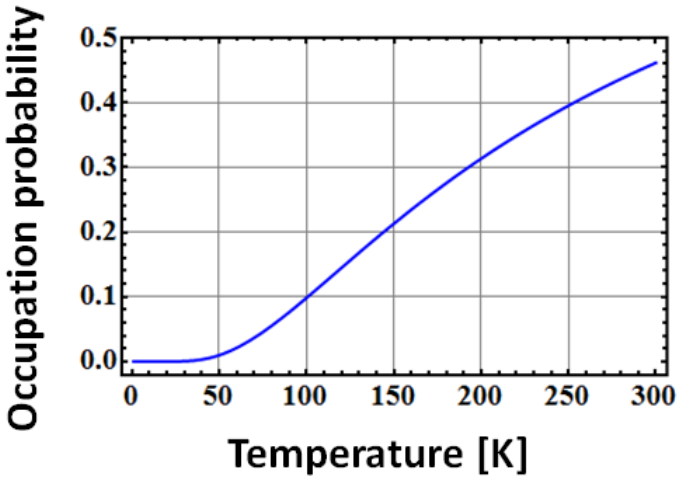

Figure 2.2: Thermal occupation of the light hole state in dependence on the temperature

without them. The development of microcavities was strongly boosted by the innovations in the growth techniques by molecular beam epitaxy (MBE) and is still a topic of research in these areas. The name microcavity stems from its thickness, which is often only a few micrometers.

Semiconductor microcavities (MCs) consist of a microcavity active region sandwiched between two highly reflective mirrors as presented in the Fig. 2.3(a). MCs trap light of the wavelength λ_C, i.e. forming standing electromagnetic waves and enhancing the amplitude of the electromagnetic waves in the MC active region. λ_C is set by the optical length L_C of the MC active region, which is given by $L_C = d_C\, n_C$, where d_C is the thickness and n_C is the refractive index of the MC active region.

By embedding an active medium, e.g. GaAs QWs, into the MC active region with its excitation energy in resonance with the energy of the confined MC mode and spatially located at the maximum of the electric field of MC mode, the active medium and the MC mode interact and couple to each other. The regime of coupling (weak or strong coupling) is determined by the quality (Q) factor of the MC.

The MC material systems and geometries may vary from a simple planar MC geometry with metallic mirrors to sophisticated pillar MCs [15], [16]. In the following, the discussion is focused on planar MCs with alternating layers of dielectric media to form the distributed Bragg reflectors as used for the experimental part of this work. Nevertheless, most of the theoretical properties discussed here apply to other MC geometries.

2.2.1 Distributed Bragg reflectors

Distributed Bragg reflectors (DBRs) are multiple repeats of alternating layers of dielectric media with different refractive indexes n_1 and n_2. The optical thickness

of the dielectric layers is $m \times \lambda_{DBR}/4$, where $m \ni \mathbb{N}$ and uneven and λ_{DBR} is the central wavelength of the DBR stopband. A photon traveling through such a structure experiences multiple reflections due to the periodic change of refractive indexes and the DBR will act as an interference mirror for incident light. The width $\Delta\lambda_{DBR}$ of the photonic stopband and as well the reflectivity R_{DBR} of the DBR are dependent on the contrast between n_1 and n_2 and the number N of pairs of the alternating dielectric DBR layers. For $m = 1$, $\Delta\lambda_{DBR}$ can be expressed by [17]

$$\Delta\lambda_{DBR} = \frac{4\lambda_{DBR}}{\pi} \arcsin\left(\frac{|n_1 - n_2|}{n_1 + n_2}\right). \tag{2.2.1}$$

R_{DBR} is approximately given by [18]

$$R_{DBR} = \left(\frac{n_O\, n_2^{2N} - n_T\, n_1^{2N}}{n_O\, n_2^{2N} + n_T\, n_1^{2N}}\right)^2, \tag{2.2.2}$$

where n_O and n_T are the refractive indexes of the originating and the terminating medium, e.g. of air and substrate, respectively. Neglecting absorption of the dielectric layers in a DBR, the transmission T_{DBR} of the DBR can be deduced from $T_{DBR} = 1–R_{DBR}$.

2.2.2 Microcavity physics

The microcavity mode at wavelength λ_C arises when a $L_C = m\,\lambda_C/\,(2n_C)$ - thick layer ($m \ni \mathbb{N}$) is introduced between two DBRs (cf. Fig. 2.3a-b)). The MC mode can be understood as the result of the interruption of the periodicity of the DBRs. The new structure is called a planar microcavity. The L_C-thick layer with the refractive index n_C is the MC active region, where light of the wavelength λ_C forms a standing wave with an enhanced electromagnetic field. By choosing m as an even integer, the electric field of the MC mode along the confinement direction has an antinode at the centre of the MC (cf. Fig. 2.3(c)).

Planar MCs are very similar to the Fabry-Perot cavities and many results for Fabry-Perot structures apply for the MCs. However, some of the results needs to be modified. For instance, due to the finite reflectivity of the upper and lower DBR, the MC mode penetrates into the DBRs and thus, has a longer effective MC length L_C^{eff} than L_C.

$$L_C^{eff} = L_C + L_{DBR}, \tag{2.2.3}$$

where L_{DBR} is the penetration length into the DBRs, $L_{DBR} = \frac{2\pi}{2n_C}\,\frac{n_1\,n_2}{|n_1-n_2|}$ [19]. The wavelength λ_C^{eff} of the MC mode then reads

$$\lambda_C^{eff} = \frac{L_C^{eff}\,\lambda_C\,\lambda_{DBR}}{L_C\,\lambda_C + L_{DBR}\,\lambda_{DBR}}, \tag{2.2.4}$$

where λ_{DBR} is the wavelength at which the stopband of the DBRs is centred [19]. In the case of a perfectly grown sample: $\lambda_C = \lambda_{DBR} = \lambda_C^{eff}$. In a real sample, there

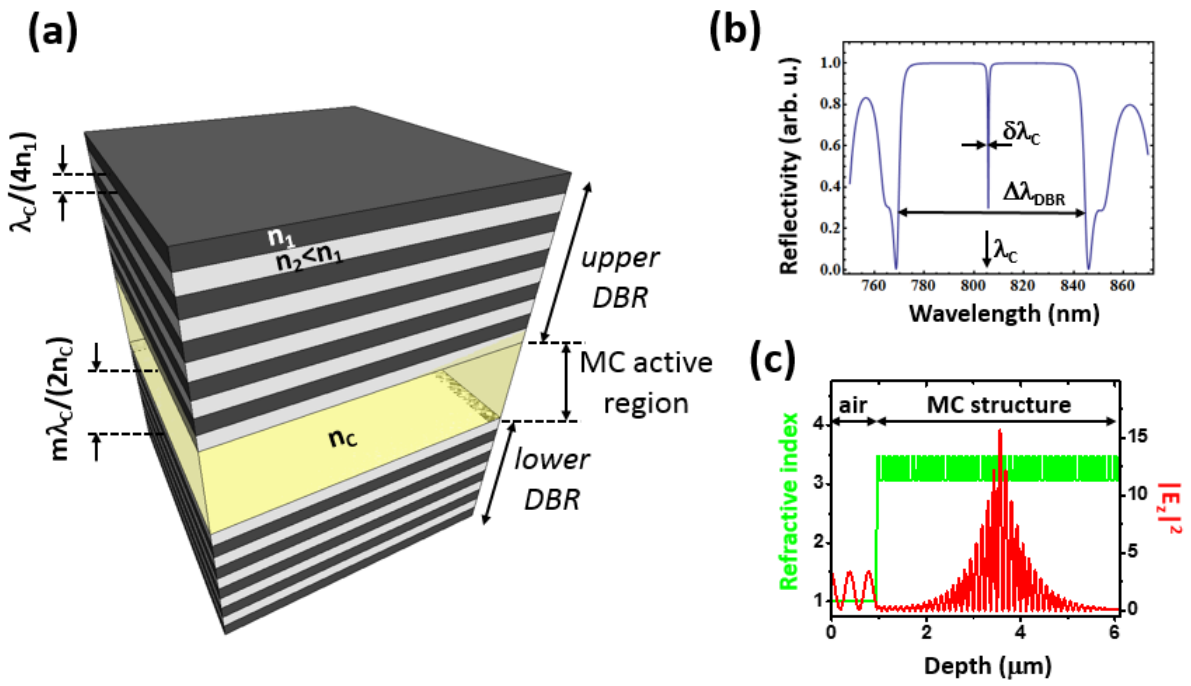

Figure 2.3: (a) Scheme of a (Al, Ga)As-based MC structure ($n_1 = n_{Al_{15}Ga_{85}As}$ and $n_2 = n_{Al_{80}Ga_{20}As}$) with (b) the corresponding calculated reflectivity spectrum for $\lambda_C = 805\,nm$ at $T = 10\,K$. (c) Depth dependence of the refractive index of the MC (green curve) with the distribution of the intensity of the electric field $|E_z|^2$ (red curve) along the confinement direction z

are small deviations between λ_C and λ_C^{eff}. However, as long as the energy of the MC mode is in or close to the resonance energy of the active medium, i.e. GaAs QW excitons, there will be coupling between them. In the studied sample structure λ_C is $805\,nm$.

Due to the finite reflectivity of the DBRs, the MC mode has a finite spectral width δf_C (full width at half-maximum) given by [19]:

$$\delta f_C = \frac{c\,(1 - R_{DBR})}{n_C\,L_C^{eff}}. \tag{2.2.5}$$

δf_C is approximately $90\,GHz$ in the studied sample. Accordingly, the lifetime τ_C of the trapped photons, i.e. that is the time the photons spend in the MC, is around $10\,ps$.

A trapped photon in a planar MC is confined in one direction, i.e. z, whereas it is free in the directions perpendicular to z, i.e. x- and y-direction. The energy dispersion $E_C(k) = \hbar\,c\,|\mathbf{k}_C|/n_C$ of a trapped photon differs from the one of the free photon. $|\mathbf{k}_C|$ is the total momentum of the photon. Since the photon is confined in space along the z-direction, $|\mathbf{k}_C|$ reads

$$|\mathbf{k}_C| = \sqrt{k_z^2 + k_{||}^2}, \tag{2.2.6}$$

where $k_{||} = \sqrt{k_x^2 + k_y^2}$ is the planar momentum. k_z is quantised, i.e. $k_z = 2\pi/L_C$, while $k_{||}$ can take any value. In nearest approximation in terms of the Taylor-series for small $k_{||}$, the energy dispersion $E_C(k)$ reads

$$E_C(k_{||}) = \frac{\hbar\,c}{n_C}\left(\sqrt{k_z^2} + \frac{k_{||}^2}{2\sqrt{k_z^2}} + \mathcal{O}(k_{||})\right) \tag{2.2.7}$$

and can be assumed as parabolic, when only one quantized level of k_z is concerned.

$E_C(k_{||})$ can be rewritten as $E_C(k_{||}) = \frac{2\pi\,\hbar\,c}{n_C\,L_C} + \frac{\hbar^2 k_{||}^2}{2\,m_C}$. Hence, the effective mass m_C of the MC photons is $m_C = \frac{2\pi\,\hbar\,n_C}{c\,L_C}$. The effective photon mass is very small in comparison to the exciton mass as it amounts to $10^{-5} - 10^{-4}\,m_X$, where m_X is the exciton mass.

The planar vector $k_{||}$ is related to the angle of incidence θ of a photon emitted by MC exciton-polariton into free space:

$$k_{||} = \frac{E_C(k=0)}{\hbar\,c\,n_C}\,\sin(\theta) = \frac{2\pi}{\lambda_C}\,\sin(\theta)\,. \tag{2.2.8}$$

2.2.3 Quality (Q) factor

The stored electromagnetic field of light, e.g. the electric field $\mathbf{E}(\mathbf{r}, t)$, in the MC decays exponentially with the time constant τ_C. The decay is due to the absorption, scattering and transmission of light through the DBRs. The lifetime τ_C includes all these losses and can be increased by increasing the reflectivity R_{DBR} of the DBRs.

$$\mathbf{E}(\mathbf{r},t) = E_0(\mathbf{r})\,\exp\left(i\,\omega_C\,t - \frac{t}{\tau_C}\right), \tag{2.2.9}$$

where ω_C is the angular frequency of the stored light. The electric field oscillates in the MC and loses energy per every oscillating cycle. The quality (Q) factor describes these losses and measures the ability of the MC to store light. It is a dimensionless parameter, defined by

$$Q = 2\pi\frac{stored\,energy}{energy\,loss\,per\,cycle} = 2\pi\,\frac{u(t)}{|\frac{du(t)}{dt}|\,T}, \tag{2.2.10}$$

where $u(t)$ is the stored energy of light in the MC and the denominator $|\frac{du(t)}{dt}|\,T$ describes the energy losses per cycle period T, where $T = \frac{2\pi}{\omega_C}$. Assuming an exponential energy decay of $u(t)$, i.e. $u(t) \propto e^{-\Gamma t}$, where Γ is the energy decay rate, one obtains: $|\frac{du(t)}{dt}| = \Gamma\,u(t)$. Thus, the Q-factor can be put into a more handy form. Namely,

$$Q = \frac{\omega_C}{\Gamma} = \frac{\omega_C}{\delta\omega_C} = \frac{\lambda_C}{\delta\lambda_C}, \tag{2.2.11}$$

where Γ can be read out from the full width at half maximum (FWHM), i.e. $\delta\omega_C$ or $\delta\lambda_C$, of the MC mode in the reflectivity spectra (cf. Fig. 2.3(b)).

An additional important parameter is the spatial decay of the electric field $\mathbf{E}(\mathbf{r},t)$ of the MC mode into the DBRs. It is favourable to have a small MC mode volume V_C in order to realise exciton-polaritons. A small V_C leads to a strong confinement of the circulating electric field within the MC active region and thus, to a high circulating intensity of light. For completeness, the definition of V_C reads $V_C = \frac{\int \epsilon(\mathbf{r})|\mathbf{E}(\mathbf{r})|^2 d^3r}{\epsilon(\mathbf{r}_{max})|\mathbf{E}(\mathbf{r}_{max})|^2}$, where $\epsilon(\mathbf{r})$ is the permittivity and $\mathbf{r}_{max}$ is position vector, where the electric field of light has its maximum [20].

2.3 Quantum well microcavity exciton-polaritons

2.3.1 Light-matter interaction

In general, any active medium, i.e. GaAs QW providing excitons, that is placed in a continuum of the radiation field, i.e. light, can be spontaneously excited from an initial state $|i\rangle$ to an excited state $|f\rangle$ by absorbing a photon and afterwards decay spontaneously to $|i\rangle$ by emitting a photon into the continuum. These transitions take place at the rate $\Gamma_{|i\rangle\rightarrow|f\rangle}$ described by the Fermi's Golden rule [21]:

$$\Gamma_{|i\rangle\rightarrow|f\rangle} = \frac{2\pi}{\hbar}\,\rho(\omega)\,|\langle i|\,\mathbf{E}(\mathbf{r})\cdot\mathbf{d}\,|f\rangle|^2, \tag{2.3.1}$$

where $\mathbf{E}(\mathbf{r})$ is the electric field of the radiation field at the position $\mathbf{r}$ of the active medium, $\mathbf{d}$ is its dipole moment and $\rho(\omega)$ is the optical density of states of the radiation field. Thus, by choosing $\rho(\omega)$ the radiation field can be put into resonance

with the excitation energy of the active medium or not. In the case of resonance, the transition rates $\Gamma_{|i\rangle\rightarrow|f\rangle}$ will be enhanced, while in the non-resonant case the radiative transitions will be suppressed. $\rho(\omega)$ is determined by the design of the MC, i.e. the MC mode at the frequency ω_C and its linewidth $\delta\omega_C$. By confining light in a MC and by placing a GaAs QW into the MC active region, the transition rate $\Gamma_{|i\rangle\rightarrow|f\rangle}$ modifies to [68]

$$\Gamma_{MC} = \frac{1}{1+4\,Q^2\left(\frac{\lambda_X}{\lambda_C}-1\right)^2}\frac{|\mathbf{E}(\mathbf{r}_X)|^2}{|\mathbf{E}(\mathbf{r}_{max})|^2}\cos^2(\theta)\;F_P\,\Gamma_0+\Gamma_{LEAK}, \tag{2.3.2}$$

where λ_X and λ_C are the wavelengths of the resonance of the excitons and the MC mode, respectively,[22], [23]. $\mathbf{E}(\mathbf{r}_X)$ is the electric field acting at the GaAs QW, $\mathbf{E}(\mathbf{r}_{max})$ the maximal electric field of the MC mode and θ the angle between the dipole moment of the exciton and electric field of the MC mode. F_P is the so-called Purcell factor. F_P describes the enhancement of the transition rates $\Gamma_{|i\rangle\rightarrow|f\rangle}$. Γ_0 represents the spontaneous transition rate and Γ_{LEAK} accounts all possible leaking modes to which the exciton may decay.

When $\lambda_X = \lambda_C$, $\Gamma_{LEAK} = 0$ and the maximal electric field of the MC spatially overlaps with the GaAs QW, the transition rate Γ_{MC} simply becomes: $\Gamma_{MC} = F_P\,\Gamma_0$. According to [24], the Purcell factor is characterised by the Q-factor and the MC mode volume:

$$F_P = \frac{3}{4\pi^2}\left(\frac{\lambda_C}{n_C}\right)^3\frac{Q}{V_C}. \tag{2.3.3}$$

Obviously, the excitation rate of excitons in a MC and their decay rate depend on the Q-factor and volume V_C of the MC mode. Both, a high Q-factor and small V_C are necessary for high Γ_{MC}.

2.3.2 Weak vs. strong coupling regime

In the situation when a MC photon emitted by an exciton has a negligible probability of being reabsorbed by the GaAs QW and to recreate an exciton, one speaks about the weak coupling regime between the excitons, i.e. active medium, and the radiation field.
In the strong coupling regime, the processes of absorption and emission of a photon by an exciton become reversible when the energy exchange rate between the photons and excitons is faster than their decay and decoherence rates. The emitted photon can be recaptured and recreate an exciton again. Thus, a strongly coupled two-level system is established. This is the birth of a new quasi-particle called exciton-polariton.

The strong coupling regime is experimentally realised by placing GaAs QWs in the maxima of the light field in a MC of high Q-factor. The Q-factor of the used MC for the experimental part of this work is 2000.

2.3.3 Properties of exciton-polaritons

Exciton-polaritons are quasi-particles, which result in the strong coupling regime as described before. The strong coupling between the MC mode and the QW excitons can be described in terms of the coupled oscillator model. The corresponding Hamiltonian reads

$$\hat{H} = \begin{pmatrix} E_X & \frac{\hbar\Omega}{2} \\ \frac{\hbar\Omega}{2} & E_C \end{pmatrix} \tag{2.3.4}$$

in the base $|X\rangle$, $|C\rangle$ of the exciton and photon, respectively. The eigenstates with the corresponding eigenenergies of the coupled light-matter system are

$$|LP\rangle = c_{LP,C}\,|C\rangle + c_{LP,X}\,|X\rangle, \tag{2.3.5}$$

$$|UP\rangle = c_{UP,C}\,|C\rangle + c_{UP,X}\,|X\rangle, \tag{2.3.6}$$

$$E_{LP} = \frac{1}{2}\left(E_X + E_C - \sqrt{\hbar^2\Omega^2 + \delta^2}\right), \tag{2.3.7}$$

$$E_{UP} = \frac{1}{2}\left(E_X + E_C + \sqrt{\hbar^2\Omega^2 + \delta^2}\right), \tag{2.3.8}$$

where $|LP\rangle$ and $|UP\rangle$ are the lower and upper exciton-polariton states, respectively. $\hbar\Omega$ is the so-called Rabi-splitting energy between the two states. δ is the detuning between the energy of the QW exciton E_X and the MC mode energy E_C, i.e. $\delta = E_X - E_C$. The detuning is a function of the planar wavevector $k_{||}$, i.e. $\delta(k_{||})$, due to the dependence of E_X and E_C on $k_{||}$. The strong coupling between the MC mode and the QW excitons is characterised by the anti-crossing of their branches (cf. Fig. 2.4).

$$c_{LP,C} = c_{UP,X} = \sqrt{\frac{1}{2}\left(1 - \frac{\delta}{\sqrt{\hbar^2\Omega^2 + \delta^2}}\right)}, \tag{2.3.9}$$

$$c_{UP,C} = -c_{LP,X} = \sqrt{\frac{1}{2}\left(1 + \frac{\delta}{\sqrt{\hbar^2\Omega^2 + \delta^2}}\right)}, \tag{2.3.10}$$

$c_{LP/UP,C}$ and $c_{LP/UP,X}$ are the Hopfield coefficients [25]. They quantitatively describe the mixing of the photonic state $|C\rangle$ and the excitonic state $|X\rangle$ in the exciton-polariton states $|LP\rangle$ and $|UP\rangle$. The exciton and MC photon fractions in the exciton-polariton states are determined by the Rabi-splitting Ω and the detuning δ. The Hopfield coefficients satisfy the relation: $|c_{LP/UP,C}|^2 + |c_{LP/UP,X}|^2 = 1$. The effective masses of the exciton-polaritons in the lower and upper polariton branch are given respectively by

$$\frac{1}{m_{LP}} = \frac{|c_{LP,C}|^2}{m_C} + \frac{|c_{LP,X}|^2}{m_X}, \tag{2.3.11}$$

$$\frac{1}{m_{UP}} = \frac{|c_{UP,C}|^2}{m_X} + \frac{|c_{UP,X}|^2}{m_C}. \tag{2.3.12}$$

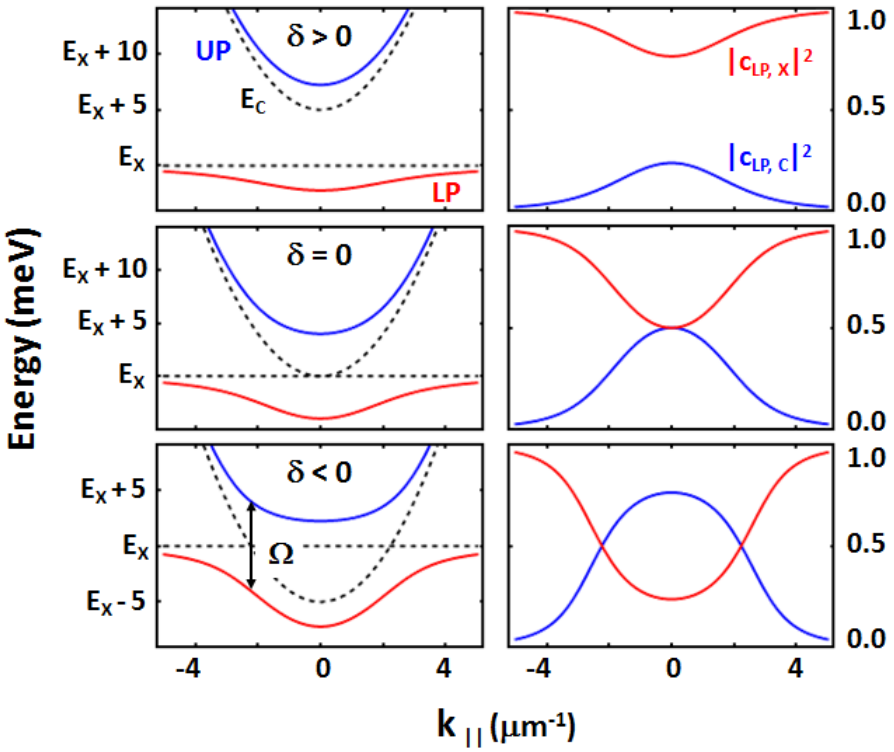

Figure 2.4: Calculated exciton-polariton dispersion (left panels) with the corresponding Hopfield coefficients (right panels) for different energy detuning δ

Since the effective mass m_C of the MC photon is much smaller than the exciton mass m_X, the effective masses m_{LP} and m_{UP} of the exciton-polariton in the lower and upper branch can be approximated by $m_{LP} = m_C/|c_{LP,C}|^2$ and $m_{UP} = m_C/|c_{UP,X}|^2$ for $k_{||} \sim 0$, respectively.

Figure 2.4 displays the lower and upper exciton-polariton states as well as the Hopfield coefficients for different detunings δ. At the resonance between the MC mode and the QW exciton, i.e. $\delta = 0$, there is an equal mixing of the photonic and excitonic states. In the case of negative detuning, i.e. $\delta < 0$, the exciton-polaritons in the lower polariton branch are more photonic-like, thus having a lighter effective mass than in the case of a positive detuning δ, i.e. $\delta > 0$.

Considering a sample design as shown in the Fig. 2.3(a) the Rabi-splitting is given by [26]:

$$\Omega \approx 2\sqrt{\frac{2\Gamma_X\, c\, N_{QW}}{n_C\, L_C^{eff}}}, \tag{2.3.13}$$

where N_{QW} is the number of the embedded QWs in the MC active region and Γ_X is the radiative decay rate of a free exciton. Γ_X is linearly proportional to the exciton oscillator strength per unit area and can be expressed as given in [27] by

$$\Gamma_X = \frac{e^2}{4n_C\,\varepsilon_0\,m_e\,c}\,f_X. \tag{2.3.14}$$

The strong coupling regime can only be achieved when the Rabi-splitting is greater than the linewidth of the MC mode and the radiative linewidth of the exciton. This necessary condition for the strong coupling can be stated by: $\Omega \gg (\Gamma_C + \Gamma_X)/2$, where Γ_C is the decay rate of the MC photons (Γ_C corresponds to Γ_{LEAK} in Eq. 2.3.2). Thus, a high number of QWs and a high Q-factor MC, i.e. highly reflective DBRs, favours the observation of exciton-polaritons in sample structures. Also, the Q-factor of the MC determines the lifetime of the exciton-polaritons. The lifetime τ_X of the exciton is approximately a few hundreds of ps in the studied GaAs QWs. Γ_X is mainly governed by the overlap of the electron and hole wave functions. It is intrinsically set by the material, i.e. GaAs, properties and its geometry, i.e. thickness of the QW. The lifetime τ_C of the MC photon is dependent on the reflectivity of the DBRs of the MC and thus, on the Q-factor. The samples investigated in this work have a Q-factor of 2000 and the experimentally measured linewidth of the MC mode is $0.2\,nm$ corresponding to τ_C of $10\,ps$. The lifetimes τ_{LP} and τ_{UP} of the exciton-polaritons in the lower and upper branch, respectively, are given by:

$$\frac{1}{\tau_{LP}} = \frac{|c_{LP,C}|^2}{\tau_C} + \frac{|c_{LP,X}|^2}{\tau_X}, \tag{2.3.15}$$

$$\frac{1}{\tau_{UP}} = \frac{|c_{UP,X}|^2}{\tau_C} + \frac{|c_{UP,C}|^2}{\tau_X}. \tag{2.3.16}$$

For $\tau_X \gg \tau_C$ follows: $\frac{1}{\tau_{LP}} \approx \frac{|c_{LP,C}|^2}{\tau_C}$ and $\frac{1}{\tau_{UP}} \approx \frac{|c_{UP,X}|^2}{\tau_C}$.

Coherence length

Another property of the exciton-polaritons, which is of importance for this work, is the spatial coherence length L_{coh} of the exciton-polaritons. L_{coh} can be estimated from the de Broglie wavelength λ_{dB}, which reads

$$\lambda_{dB} = \sqrt{\frac{h^2}{2\pi\,m_{LP/UP}\,k_B\,T}}. \tag{2.3.17}$$

At temperatures around $10\,K$, the coherence length of exciton-polaritons at the lower exciton-polariton branch is several micrometer long. Thus, μm-long potentials, e.g. surface acoustic waves with a wavelength of few μm, can be used to coherently modulate exciton-polaritons.

Mapping the momentum and real-space of exciton-polaritons

An exciton-polariton decays by emitting a photon from the MC. The emitted photon has the same planar wavevector and the same energy E_O as the decayed exciton-polariton. This one-to-one correspondence between the exciton-polariton and its corresponding out-coupled photon enables one to probe the exciton-polariton planar

wavevector dependence on the energy by angle-resolved photoluminescence measurements.

The energy E_O of the out-coupled light propagating in air is generally defined by $E_O = \hbar\, c\, \sqrt{k_x^2 + k_y^2 + k_z^2}$, where the refractive index of light is $n_O = 1$ and the x-, y- and z-axes are defined in Fig. 2.5. Due to the conservation of the planar wavevector and energy E_O, the k_z wavevector component is

$$k_z = \sqrt{\left(\frac{E_O}{\hbar\, c}\right)^2 - k_{||}^2}, \tag{2.3.18}$$

where $k_{||} = \sqrt{k_x^2 + k_y^2}$. According to the Fig. 2.5:

$$\tan(\theta_O) = \frac{k_{||}}{k_z} = \frac{k_{||}}{\sqrt{\left(\frac{E_O}{\hbar\, c}\right)^2 - k_{||}^2}} \;\Rightarrow\; k_{||} = \frac{E_O}{\hbar\, c\, \sin(\theta_O)}. \tag{2.3.19}$$

Note that the angle θ_{n_1} is related to θ_O through the Snell's law, i.e. $n_1 \sin\theta_{n_1} = n_O \sin\theta_O$, where n_1 and n_O are the material dependent refractive indices. Accordingly, the planar wavevectors $k_{||,\,n_1}$ and $k_{||}$ are connected by $\frac{k_{||,\,n_1}}{k_{||}} = \frac{\sin\theta_{n_1}}{\sin\theta_O} = \frac{n_O}{n_1}$, since $k_{||/||,\,n_1} = \frac{2\pi}{\lambda_{O/n_1}}$ and $\frac{\sin\theta_{n_1}}{\sin\theta_O} = \frac{\lambda_{n_1}}{\lambda_O}$, where λ_{n_1} and λ_O are the wavelengths of light in the medium with the refractive index n_1 and n_O, respectively. The planar wavevector $k_{||}$ is conserved at all interfaces. Furthermore, thanks to the rotational symmetry, the azimuthal angle ϕ_O is conserved.

The angle θ_O of the out-coupled light from the MC carries information about the planar wavevector of the MC exciton-polaritons. In particular, since in the experiment exciton-polaritons (with different energies) are created, the latter property allows one to map the distribution of the exciton-polariton population, e.g. the exciton-polariton dispersion, and will be used throughout this work.

$$(k_x,\, k_y) \Leftrightarrow (\theta_O,\, \phi_O)$$

A scheme for the experimental set-up to measure the planar wavevector is shown in the Fig. 2.6(a). The corresponding real-space image of the exciton-polaritons can be obtained in the same manner (cf. Fig. 2.6(b)).

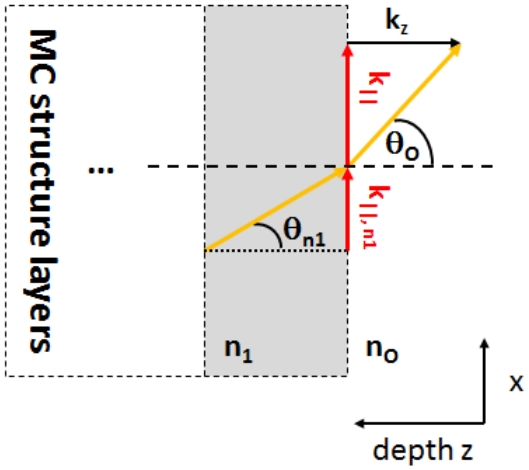

Figure 2.5: Correspondence between the exciton-polaritons and their out-coupled photons thanks to the energy and planar momentum conservation

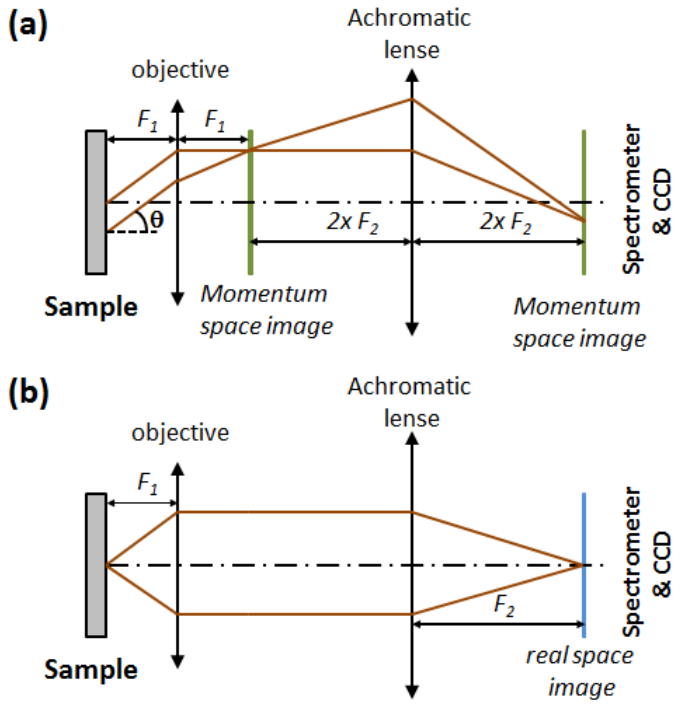

Figure 2.6: Scheme of the experimental set-up to map (a) the momentum and (b) the real-space of exciton-polaritons

2.4 Surface acoustic waves

In analogy to atomic systems, where magnetic and optical traps are applied to control interactions between atoms [28], [29], several strategies have been suggested to control MC exciton-polaritons. For example, Daif *et al.* (2006) and Winkler *et al.* (2015) used overgrowth techniques to create static perturbative potentials for the exciton-polaritons by influencing the thickness of the MC active region [30], [31]. This technique allows one to fabricate MC structures with arbitrary external potentials on a μm-scale and thus, modulate the interactions between the MC photons and the excitons, e.g. to change the detuning δ. However, the external potentials are static and cannot be changed or removed. The disadvantage can be overcome by applying an external mechanical stress on the MC structure, e.g. by using surface acoustic waves.

In this work, surface acoustic waves (SAWs) are used to coherently modulate exciton-polaritons. SAWs are mechanical vibrations that propagate along a surface. Their energy is concentrated close to the surface (within a depth of one SAW wavelength) and their amplitude strongly reduces with depth. The coherent modulation by SAWs is possible when the wavelength λ_{SAW} of SAWs is smaller than the coherence length L_{coh} of exciton-polaritons, i.e. $L_{coh} < \lambda_{SAW}$. As been pointed out previously, L_{coh} is in the range of several μm. For the experimental part of this work, λ_{SAW} was chosen to be $8\,\mu m$. SAWs have an advantage that they provide a periodic, a dynamical as well as a tuneable modulation of the potential for exciton-polaritons. As will be described later, SAWs are generated along the non-piezoelectric directions of (001) GaAs surface, i.e. along [100] and [010], by interdigital transducers (IDTs) placed on piezo-electric ZnO-islands. SAWs can be turned on and off in contrast to static modulation potentials. They are used to affect the in-plane motion of exciton-polaritons and thus, to modulate their properties. Phenomena like the reduction of the excitation power necessary for the non-equilibrium Bose-Einstein condensation (BEC) of exciton-polaritons, condensation in excited states, solitonic behaviour and others can be observed [32], [33] and [75]. The origin of the modulation of exciton-polaritons by SAWs lies in the modulation of the MC thickness and the bandgap energy of GaAs.

2.4.1 Mathematical description

Strain and stress tensor

When external forces are acting on a body, the body will deform. The coordinates of its (infinitesimal) volume elements dV will change as well as the spatial separation between them (cf. Fig. 2.7). In general, the deformation of a solid body in the i-th direction can be expressed by $\partial u_i/\partial x_j$, where $\mathbf{u} = \mathbf{r}$–$\mathbf{r}'$ is the displacement vector, $\mathbf{r}$ and $\mathbf{r}'$ are the positions of dV before and after the deformation of the body, respectively, and the indices i, $j = x$, y, z. dV changes under deformation to

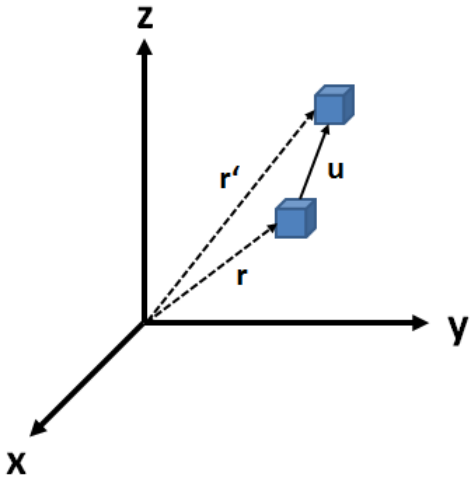

Figure 2.7: Displacement of an (infinitesimal) volume element

$$dV' = dV\left(1 + \sum_i S_{ii}\right), \tag{2.4.1}$$

where $S_{ij} = \frac{1}{2}\left(\partial u_i/\partial x_j + \partial u_j/\partial x_i\right)$ are the components of the strain tensor.

When the deformations are small, Hooke's law describes the linear relationship between the strain S and the stress T [34], [35]:

$$T_{ij} = \sum_{k,l} c_{ijkl} S_{kl}. \tag{2.4.2}$$

c_{ijkl} are the elastic stiffness constants of the material.

The elastic stiffness tensor is of the 4th rank. Thus, there are $3^4 = 81$ components in the stiffness tensor. However, considering the symmetry of T_{ij} and S_{ij}, it can be shown that $c_{ijkl} = c_{jikl}$ and $c_{ijkl} = c_{jilk}$. Furthermore, following thermodynamic considerations [36], one obtains: $c_{ijkl} = c_{klij}$. These symmetry constrains reduce the maximum number of independent elements in the stress and strain tensor to 6. An additional simplification follows by using the Voigt notation, i.e.

$$\begin{array}{ccc} (xx) \leftrightarrow 1 & (yy) \leftrightarrow 2 & (zz) \leftrightarrow 3 \\ (yz),\,(zy) \leftrightarrow 4 & (xz),\,(zx) \leftrightarrow 5 & (xy),\,(yx) \leftrightarrow 6 \end{array} \tag{2.4.3}$$

Finally, c_{ijkl} can be written as c_{mn} representing a 6×6 tensor with maximal 21 independent components. Thus, Eq. 2.4.2 can be expressed as

$$T_m = \sum_n c_{mn} S_n. \tag{2.4.4}$$

The crystal symmetry of the material may limit the number of independent stiffness tensor components. In case of GaAs and its alloys with AlAs, i.e. $Al_xGa_{x-1}As$, where x is the Al concentration, the crystal symmetry is cubic. For materials with

cubic symmetry, there are only three independent components c_{mn}. Namely, c_{11}, c_{12} and c_{44}. The corresponding stiffness tensor is of the form:

$$[c_{mn}]_{GaAs/AlAs} = \begin{bmatrix} c_{11} & c_{12} & c_{12} & 0 & 0 & 0 \\ c_{12} & c_{11} & c_{12} & 0 & 0 & 0 \\ c_{12} & c_{12} & c_{11} & 0 & 0 & 0 \\ 0 & 0 & 0 & c_{44} & 0 & 0 \\ 0 & 0 & 0 & 0 & c_{44} & 0 \\ 0 & 0 & 0 & 0 & 0 & c_{44} \end{bmatrix}. \tag{2.4.5}$$

The elastic stiffness constants for GaAs are according to Ref. [37]: $c_{11} = 11.83 \times 10^{10}\,\frac{N}{m^2}$, $c_{12} = 5.32 \times 10^{10}\,\frac{N}{m^2}$ and $c_{44} = 5.93 \times 10^{10}\,\frac{N}{m^2}$. For AlAs these constants are: $c_{11} = 12.02 \times 10^{10}\,\frac{N}{m^2}$, $c_{12} = 5.70 \times 10^{10}\,\frac{N}{m^2}$ and $c_{44} = 5.89 \times 10^{10}\,\frac{N}{m^2}$, [38]. Since the elastic stiffness constants are similar for GaAs and AlAs, it is reasonable to interpolate between them for $Al_xGa_{x-1}As$ alloys.

In this work, SAWs are generated using IDTs placed on ZnO islands. This is necessary since the SAWs must be generated along the non-piezoelectric directions of GaAs. For completeness, the stiffness tensor for ZnO is given by

$$[c_{mn}]_{ZnO} = \begin{bmatrix} c_{11} & c_{12} & c_{13} & 0 & 0 & 0 \\ c_{12} & c_{11} & c_{13} & 0 & 0 & 0 \\ c_{13} & c_{13} & c_{33} & 0 & 0 & 0 \\ 0 & 0 & 0 & c_{44} & 0 & 0 \\ 0 & 0 & 0 & 0 & c_{44} & 0 \\ 0 & 0 & 0 & 0 & 0 & \frac{c_{11}-c_{12}}{2} \end{bmatrix} \tag{2.4.6}$$

with $c_{11} = 20.90 \times 10^{10}\,\frac{N}{m^2}$, $c_{12} = 12.03 \times 10^{10}\,\frac{N}{m^2}$, $c_{13} = 10.46 \times 10^{10}\,\frac{N}{m^2}$, $c_{33} = 21.06 \times 10^{10}\,\frac{N}{m^2}$ and $c_{44} = 4.23 \times 10^{10}\,\frac{N}{m^2}$ [39], [40]. Since ZnO has a hexagonal symmetry, there are five independent components c_{nm}. For the experiments, ZnO was depositioned on the MC surface using a radio frequency (rf) magnetron sputtering technique. Thus, polycrystalline ZnO films were grown. The parameters used for the deposition process were chosen in such a way that polycrystalline ZnO films exhibited c-axis preferential growth characteristics and possessed piezoelectric properties [41].

SAWs along the non-piezoelectric directions

The SAW equation can be mathematically describes using the Newton's force equation:

$$\rho\frac{\partial^2 u_i}{\partial t^2} = \sum_j \frac{\partial T_{ij}}{\partial x_j}, \qquad i,\, j = x,\, y,\, z, \tag{2.4.7}$$

where ρ is the medium density.

The solutions of SAW modes, which propagate along a non-piezoelectric direction of a material, i.e. [100] or [010] direction on the (001) plane of $Al_xGa_{x-1}As$, are found

by solving Eq. 2.4.7 using the constitutive relation expressed by Eq. 2.4.2. A plane wave is used as the Ansatz function:

$$u_i = A_i \exp\left[i\left(\mathbf{k}\cdot\mathbf{r} - \omega t\right)\right], \tag{2.4.8}$$

where A_i is the amplitude of the particle displacement along the i-direction, $\mathbf{k} = (k_x,\, k_y,\, k_z)^T$ is the wavevector and ω is the angular frequency of the wave. Furthermore, it is useful to describe the wavevector $\mathbf{k}$ by $\mathbf{k} = \mathbf{k}_{||} + k_z\hat{z}$, where $\mathbf{k}_{||} = k_x\hat{x} + k_y\hat{y}$, and to redefine the wave numbers as $\frac{k_x}{k_{||}} = \cos(\theta)$, $\frac{k_y}{k_{||}} = \sin(\theta)$ and $\frac{k_z}{k_{||}} = \kappa$. θ is the angle between the x-axis and $\mathbf{k}_{||}$.

The Ansatz wavefunction (Eq. 2.4.8) then reads

$$u_i = A_i \exp\left[i\, k_{||}\kappa z\right] \exp\left[i\, k_{||}\left(\cos(\theta)\, x + \sin(\theta)\, y - \frac{\omega}{k_{||}} t\right)\right], \tag{2.4.9}$$

where the term $\frac{\omega}{k_{||}}$ represents the phase velocity.

Substituting Eq. 2.4.9 into Eq. 2.4.7 and following [44], [46] one has to solve the following equation in order to obtain SAW solutions:

$$M \cdot \begin{pmatrix} A_x \\ A_y \\ A_z \end{pmatrix} = \begin{pmatrix} 0 \\ 0 \\ 0 \end{pmatrix}. \tag{2.4.10}$$

For a SAW propagating along the x || [100] direction, the angle θ is zero and the matrix M reads:

$$M = \begin{pmatrix} c_{44}\kappa^2 - \left(\frac{\omega}{k_{||}}\right)^2 \rho + c_{11} & 0 & \kappa\left(c_{12} + c_{44}\right) \\ 0 & c_{44}\kappa^2 - \left(\frac{\omega}{k_{||}}\right)^2 \rho + c_{44} & 0 \\ \kappa\left(c_{12} + c_{44}\right) & 0 & c_{11}\kappa^2 - \left(\frac{\omega}{k_{||}}\right)^2 \rho + c_{44} \end{pmatrix}. \tag{2.4.11}$$

Note that there is only one component in the second row of M. Consequently, the amplitude A_y in the y-direction, i.e. [010] direction, is zero. $|M| = 0$ will lead to a quadratic equation in κ. In addition, boundary conditions must be fulfilled for a surface mode. The surface at $z = 0$ must be stress free, i.e. $T_{xz} = T_{yz} = T_{zz} = 0$, and the SAW amplitude must vanish with $z \to -\infty$. Accordingly, κ must have a negative imaginary part. It can be shown that the resulting SAW solution is composed of a transverse u_z and a longitudinal u_x component. A detailed description of the corresponding calculations can be found in Ref. [43], [44], [45] and [46]. Figure 2.8 shows the dependence of u_x and u_z components of this Rayleigh wave solution. The amplitudes of the two displacement components u_x and u_z decrease with depth at different rates and show an oscillatory decay into the bulk.

A similar solution exists for the [010] direction, where $\theta = 90^\circ$ and $\mathbf{k}_{||} = k_y\hat{y}$. In this case, the component $u_x = 0$ and $u_y \neq 0$ and the displacements are confined to the sagittal plane.

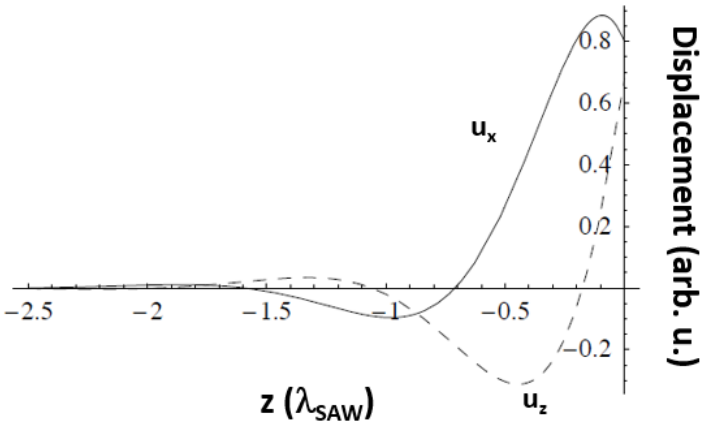

Figure 2.8: Transverse and longitudinal components of a Rayleigh wave propagating along the [100] direction on the (001) $Al_{0.3}Ga_{0.7}As$ surface as a function of depth (adopted from [46])

Waves along piezo-electric directions

The generation of acoustic waves in materials, e.g. SAWs, is usually performed by exploiting the piezo-electric properties of the material. On the (001) GaAs surface, piezo-electric directions are <110> surface directions. Therefore, the wave equation 2.4.7 needs to be modified, i.e. to include the piezo-electricity. In case of an applied external electric field $\mathbf{E}$ on a piezo-electric material, the Hooke's law states that

$$T_{ij} = \sum_{k,l} c_{ijkl} S_{kl} - \sum_{k} e_{kij} E_k, \tag{2.4.12}$$

where e_{kij} is the piezo-electric tensor. The electric field $\mathbf{E}$ is given in the quasi-static approximation by $\mathbf{E} = -\nabla\phi_{piezo}$. ϕ_{piezo} denotes the piezo-electric potential of the acoustic wave. As well, since the deformation of a piezo-electric material causes electric displacement fields, a polarisation term D_i needs to be accounted.

$$D_i = \sum_{j} \epsilon_{ij} E_j + \sum_{j,k} e_{kij} S_{jk}, \tag{2.4.13}$$

where ϵ_{ij} are the components of the dielectric tensor ϵ. For GaAs and AlAs, ϵ has one non-zero component ϵ_{11}, $\epsilon_{11} = 9.73\times10^{-11}F/m$ for GaAs and $\epsilon_{11} = 8.29\times10^{-11}F/m$ for AlAs [38]. ZnO has two non-zero components in the dielectric tensor, i.e. $\epsilon_{11} = \epsilon_{22} = 7.38 \times 10^{-11}F/m$ and $\epsilon_{33} = 7.83 \times 10^{-11}F/m$ [40]. For completeness, the piezo-electric tensor for GaAs and AlAs $[e_{kij}]_{GaAs/AlAs}$ and for ZnO $[e_{kij}]_{ZnO}$ can be found in Ref. [40]. Due to the cubic symmetry of GaAs and AlAs, $[e_{kij}]_{GaAs/AlAs}$ has only one non-zero component, i.e. e_{14}. ZnO has three non-zero piezo-electric constant e_{15}, e_{31} and e_{33}.

Possible wave solutions are obtained by solving the solution of Eq. 2.4.7 under the constitutive relations given by Eq. 2.4.12 and Eq. 2.4.13 and considering the appropriate boundary conditions, i.e. by imposing the conditions that the surface is free as well as continuity of the normal component of the dielectric field across the surface [42].

SAW propagation on multi-layer structures

In this work, SAWs propagate on a surface of a MC structure, i.e. a multi-layer structure. Consequently, the boundary conditions must be extended. The boundary conditions must impose the continuity of the stress at the interfaces between the adjacent layers at the depth z below the surface and, if the SAW propagates along the piezo-electric directions of the material, the electric displacement. This can be expressed by

$$T_{ij}\left(z^{>}\right) = T_{ij}\left(z^{<}\right), \tag{2.4.14}$$

$$D_{i}\left(z^{>}\right) = D_{i}\left(z^{<}\right), \tag{2.4.15}$$

where $z^{>}$ and $z^{<}$ denote two adjacent material layers being above z and the below z, respectively.

In order to obtain SAW solutions, a numerical procedure is required due to the complexity of the multi-layer structure. This procedure is well-described in [47], [48]. For completeness, the numerical procedure is briefly summarised. First, it includes the determination of solutions of Eq. 2.4.7 under the constitutive relations and the imposed boundary conditions for each layer for a given angular wave frequency ω and wavevector $\mathbf{k}$. The solution within each layer can be stated as an eigenvalue problem, where the z-component of the wavevector $\mathbf{k}$ is associated with the eigenvalues and the corresponding eigenvectors are written as a four-dimensional vector $\vec{v} = (u_x,\, u_y,\, u_z,\, \phi_{piezo})^T$. Note, ϕ_{piezo} will be zero, if the SAW is propagating along a non-piezoelectric direction. In the second step, the coefficients of the eigenvectors $\vec{v}$ in neighbouring layers are related to each other by imposing the continuity of $\vec{v}$ as well as the boundary conditions (Eqs. 2.4.14 and 2.4.15). By iterating across the multi-layer structure, the eigenvector coefficients of the first layer will be related to the ones of the substrate. In the last step, one seeks for angular wave frequencies ω yielding SAW solutions, where the following boundary conditions are satisfied: (i) the surface at $z = 0$ is stress free and (ii) the SAW amplitude must decay into the substrate.

Surface acoustic wave induced modulation

Strain induced modulation

SAWs create in the sample regions of tension and compression (cf. Fig. 2.9(a)) and thus, SAWs modulate the valence band (VB) energy E_{VB} and the conduction band (CB) energy E_{CB}. Correspondingly, the bandgap energy E_G, which is $E_G =$

$E_{CB} - E_{VB}$, is modulated by SAWs. The shifts of the CB and/or VB energy induced by Rayleigh waves are given by [48], [50]:

$$\Delta E_{CB} = a_{CB} S_0, \tag{2.4.16}$$

$$\Delta E_{VB} = a_{VB} S_0 \pm b_{VB} \left(S_{zz} - S_{xx}/2 \right), \tag{2.4.17}$$

where a_{CB} and a_{VB} are the hydrostatic CB and VB deformation potentials, respectively, and b_{VB} is the VB uniaxial deformation potential [49], [50]. S_0 is the hydrostatic strain related to the SAW-induced volume change, i.e. $S_0 = S_{xx} + S_{yy} + S_{zz}$, and S_{xx} and S_{zz} are the strain fields along the propagation direction x and the penetration depth z of the SAW. The sign $\pm$ refers to hh and lh states of the QW exciton. According to the above Eqs. 2.4.16 and 2.4.17, the total modulation of the bandgap becomes

$$\Delta E_G = \left(a_{CB} + a_{VB} \right) S_0 \pm b_{VB} \left(S_{zz} - S_{xx}/2 \right). \tag{2.4.18}$$

Figure 2.9(b) displays numerical calculations for the modulation of VB and CB of a pure GaAs system by a SAW with a wavelength λ_{SAW} propagating on the (001) GaAs surface plane along the [001] direction . The maximal acoustic modulation of the bandgap energy is given at the depth of approx. $\frac{1}{4}\lambda_{SAW}$, where ΔE_{VB} and ΔE_{CB} have opposite signs.

Additionally to the modulation of the bandgap energy E_G, SAWs modulate the thickness of the material and thus, its density and its refractive index. Regarding the modulation of exciton-polaritons, SAWs modulate the QW bandgap energy as well as the resonance wavelength of the MC. In the investigated MC structure, SAWs cause a modulation of the MC mode energy E_C by ΔE_C, where $\Delta E_C \approx \frac{1}{4}\Delta E_G$ [51], [83]. As well, the modulation of E_C is in phase with the modulation of E_G, i.e. when E_G reduces, E_C reduces. The total acoustic modulation of the exciton-polariton states is then the sum of ΔE_G and ΔE_C. Figure 2.10(a) displays the experimental results of the acoustic modulation of the lower exciton-polariton branch by an acoustic square lattice potential, which was mapped according to the technique presented in Fig. 2.6. The acoustic square lattice was generated as shown in Fig. 2.13(a) and will be discussed in detail later in the correspoding Subchapter. The exciton-polariton dispersion is folded due to the periodicity of the SAW potential, what is analog to the formation of the electronic band structure in crystals. Furthermore, square-like mini-Brillouin zones (MBZs) in momentum space are formed (cf. Fig. 2.10(b)). The length k_{MBZ} of the MBZ is determined by SAW wavelength λ_{SAW}, which is

$$k_{MBZ} = k_{SAW} = \frac{2\pi}{\lambda_{SAW}}. \tag{2.4.19}$$

Note that due to the curvature of the modulated exciton-polariton dispersion, the effective mass m^* of exciton-polaritons is negative at the M-points of the MBZ (cf. Fig. 2.10(b)) , whereas at the Γ-point m^* is positive and at the X-point m^* is anisotropic, i.e. negative along the $\Gamma \rightarrow$ X-direction and positive along the $\Gamma \rightarrow$ M-direction.

SAWs induce energy gaps ΔE_G^{XP} in the exciton-polariton dispersion (cf. Fig. 2.10(a)). The energy gap is dependent on the SAW power $\sqrt{P_{RF}}$:

$$\Delta E_G^{XP} \propto \sqrt{P_{RF}}. \tag{2.4.20}$$

As will be discussed in the following, the modulation by piezo-electric fields of SAWs is not favourable for the formation of exciton-polaritons and should be excluded.

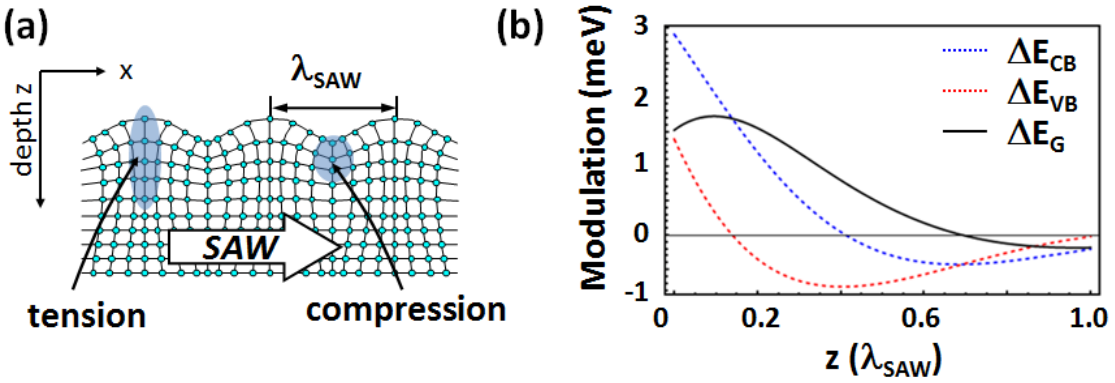

Figure 2.9: SAWs propagate on the material, e.g. GaAs, surface (a) creating regions of tension and compression (adopted from [48]), leading to (b) a depth-dependent modulation of the conduction ΔE_{CB} and valence band ΔE_{VB} energies. For the calculations, the SAW wavelength λ_{SAW} was set to $2\,\mu m$ and the SAW power density $\rho_{SAW} = 100\,\frac{W}{m}$ (ρ_{SAW} is the SAW power per unit length perpendicular to the propagation direction).

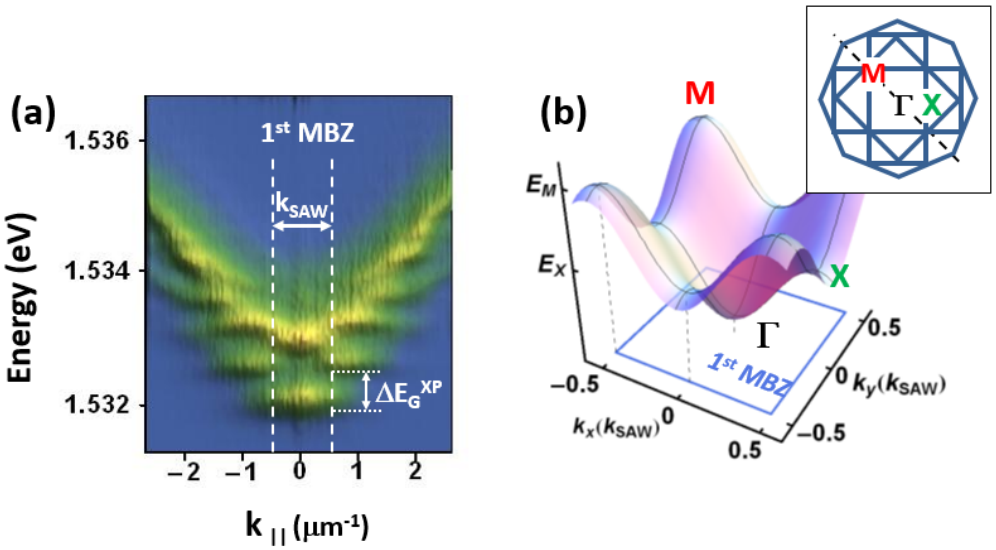

Figure 2.10: (a) Recorded exciton-polariton dispersion under acoustically induced square lattice potential along the dashed line in the inset of (b). (b) 3D scheme of the exciton-polariton dispersion in a square lattice. The insets shows a scheme of the first 4 Brillouin zones of a square lattice.

Piezo-electric field induced modulation

In piezo-electric materials, SAWs propagating along particular directions - which will be called piezo-electric directions - carry a piezo-electric potential ϕ_{piezo} induced by the strain. The longitudinal component of ϕ_{piezo} induces a type-II potential modulation of the energy bands [48], which spatially separates the optically generated electrons and holes (cf. Fig. 2.11). As well, the normal component of ϕ_{piezo} with respect to the surface induces a Stark effect, thus, separating the electrons and holes along the z-direction. Both effects reduce the overlap of the electron and hole wave functions. This results in a longer exciton lifetime and a smaller oscillation strength f_X. Regarding the formation of MC exciton-polaritons, the piezo-electric field weakens the strong coupling. This was confirmed by experimental results reported in Ref. [51]. Figure 2.12 shows the PL intensity emitted by MC exciton-polaritons under SAW modulation in dependence on the power of SAWs propagating along piezo-electric and non-piezoelectric directions. For both cases, the excitation conditions of MC exciton-polaritons were the same. The PL intensity was normalised with respect to the one without SAWs. For all SAW powers, the PL intensity is weaker when MC exciton-polaritons are modulated by SAWs along the piezo-electric directions. Thus, a smaller number of MC exciton-polaritons are created when SAWs along the piezo-electric directions are used. For these reasons, for the experimental part of this work, SAWs are generated along the non-piezoelectric directions.

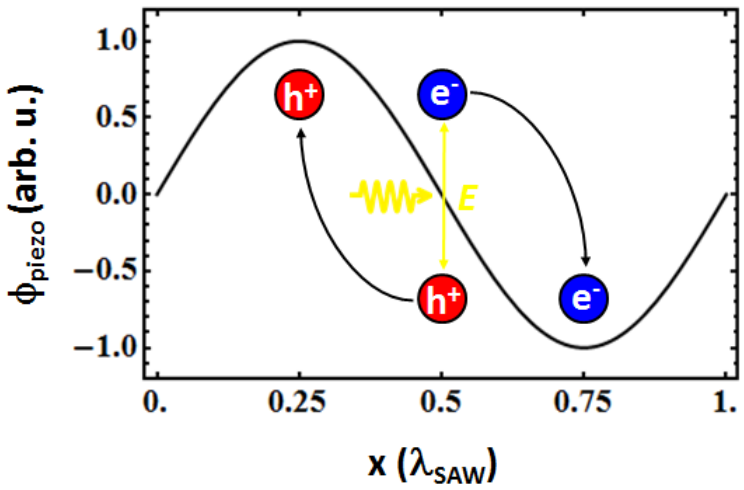

Figure 2.11: Type-II modulation induced by the piezo-electric field of a SAW

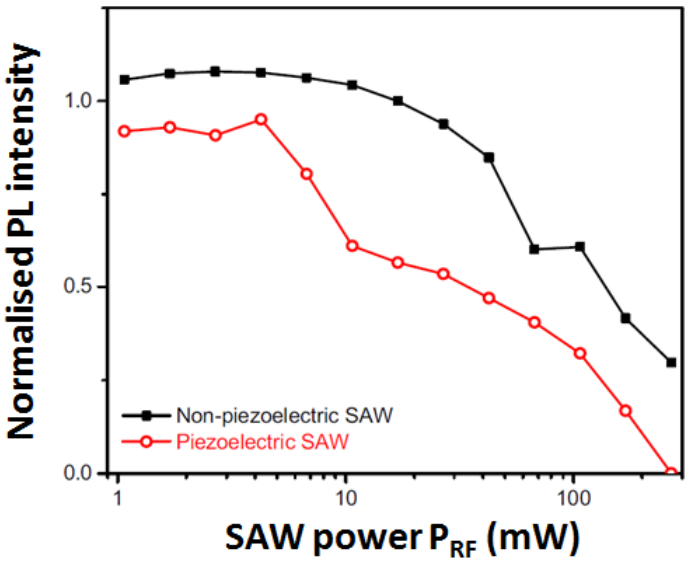

Figure 2.12: PL intensity of MC exciton-polaritons in dependence on the power of SAWs propagating along a piezo-electric and a non-piezoelectric direction (adopted from [51])

SAW generation

For this work, a (Al, Ga)As-based MC is used for the investigation of MC exciton-polaritons. Two SAWs are generated along the non-piezoelectric directions on (001) GaAs surface, i.e. [100] and [010]. Since the SAWs propagate perpendicularly to each other, they interfere and correspondingly create a dynamic acoustic square lattice. The square lattice results when the generated SAWs, i.e. SAW_x and SAW_y, possess the same wavelength. The phase velocity v_{lat} of the acoustic square lattice is then $v_{lat} = \sqrt{2}\, v_{SAW}$, where v_{SAW} is the SAW velocity of each SAW. The lattice periodicity is given by the SAW wavelength λ_{SAW}.
Fig. 2.13(a)-(b) below schematically displays a MC structure with an acoustically induced square lattice. The SAWs are generated by metallic interdigital transducers (IDTs) deposited on 600 nm thick ZnO-islands as shown in Fig. 2.13(c). ZnO-islands are necessary since the generation of SAWs using IDTs relies on the inverse piezoelectric effect. Thus, an electric field applied to the IDTs induces deformations of the ZnO, which is mechanically transmitted to the MC. The SAW wavelength λ_{SAW} is determined by the width and the separation of the IDT fingers (cf. Fig. 2.13(c)). The SAW frequency f_{SAW} is $f_{SAW} = v_{SAW}/\lambda_{SAW}$. In GaAs, v_{SAW} is approximately $3\,\mu m/ns$. For a detailed review on the IDT function and design, the reader is referred to [52], [53].

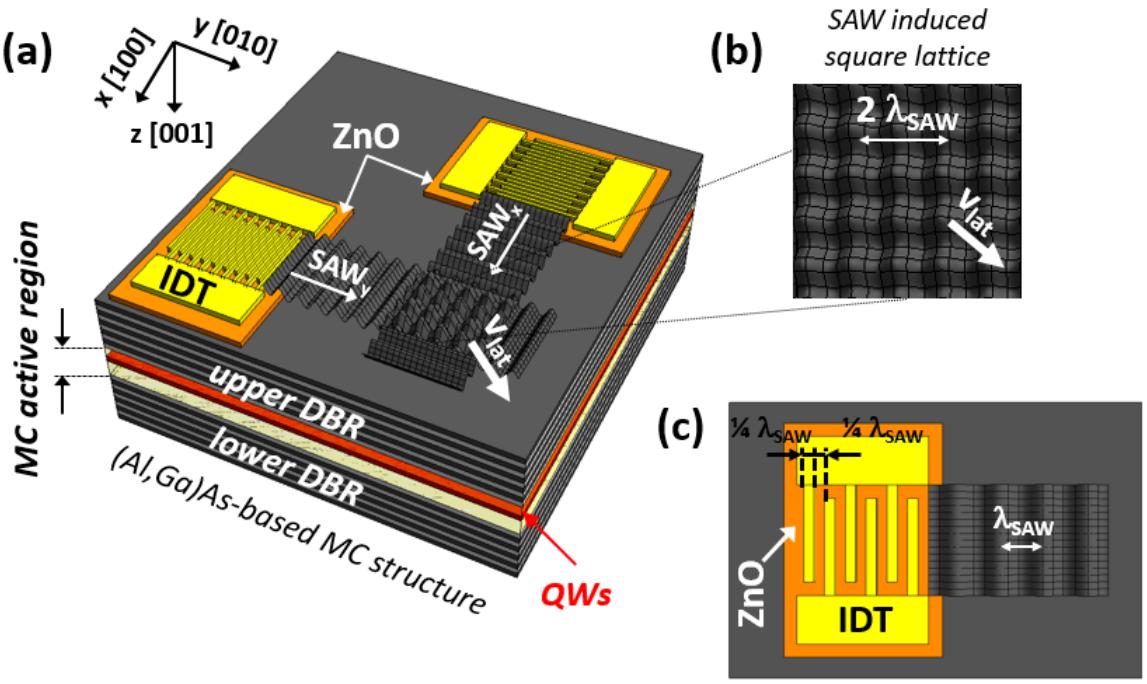

Figure 2.13: (a) Generation an acoustic lattice using SAWs generated by IDTs deposited on ZnO-islands. (b) The acoustic square lattice results due to interference of two to each other perpendicularly propagating SAWs of the same wavelength. (c) The SAW wavelength is determined by the IDT finger widths and their separation to each other.

2.4.2 Sample design and numerical results

In the following, the design of the investigated MC structure for modulation by SAWs is discussed and numerical results are presented. The scheme of the sample structure is shown in the Fig. 2.13(a). The $\frac{3}{2}\lambda$-thick MC active region contains 3 stacks of pairs of 15 nm-thick GaAs QWs placed at the antinodes of the confined electric field of the MC mode. There are following requirements on the MC structure for the investigation of MC exciton-polaritons and their modulation by SAWs (cf. Sec. 2.3):

- Energy E_C of the MC mode must be in resonance with the exciton energy E_X.
- MC must have a high Q-factor in order to insure the strong coupling between excitons and the MC mode.
- MC active region must be small in order to have a small MC mode volume V_C.
- The active medium GaAs must be placed as QWs into the MC in order to enhance the exciton oscillator strength.

- GaAs QWs must be placed at the antinodes of the electric field of the MC mode.
- Several GaAs QWs, i.e. N_{QW}, must be placed into the MC to increase the Rabi-splitting.
- The linewidth $\delta\lambda_{XP}$ of exciton-polariton states must be smaller than the modulation potential Φ_{SAW} induced by SAWs.

As pointed out previously, for observation of the strong coupling between excitons and light, a high Q-factor of the MC is required. This implies highly reflective DBRs. In other words, the DBRs must be composed of many layers, which results in a large distance d between the embedded GaAs QWs and the surface of the MC structure. Since the maximal acoustic modulation in $Al_xGa_{x-1}As$ structures occurs at the depth of approx. $\frac{1}{4}\lambda_{SAW}$ (cf. Fig. 2.9(b)), the depth d of the GaAs QWs within the MC determines λ_{SAW}, i.e. $\lambda_{SAW} \approx 4d$. Additionally, the energy density of SAWs decreases with increasing λ_{SAW}. Thus, the strain induced bandgap modulation of QWs reduces with increasing λ_{SAW}. For the investigated MC structure, a compromise was found by using 16 upper DBR pairs with a total thickness of $2\,\mu m$ and thus, $\lambda_{SAW} = 8\,\mu m$ corresponding to $f_{SAW} = 370\,MHz$. In detail, the upper DBR consists of 16 $\lambda_C/4$-thick $Al_xGa_{x-1}As$ layer pairs with x alternating between 0.15 and 0.8. The lower DBR consists of 13 pairs of a $\frac{\lambda_C}{4}$-thick $Al_{0.8}Ga_{0.2}As$ layer and $\frac{3}{4}\lambda_C$-thick $Al_{0.15}Ga_{0.85}As$ layer after the MC active region followed by 10 $\frac{\lambda_C}{4}$-thick $Al_xGa_{x-1}As$ layer pairs. The lower effective Al content in the lower DBR additionally improves the confinement of the SAW strain field maximum at the depth of the embedded GaAs QWs.

Figure 2.14(a) shows the calculated reflectivity spectrum of the investigated MC structure at $T = 10\,K$. There are two reflectivity dips within the stopband, which correspond to the lower and upper exciton-polariton branches at the energy $E_{LP} = 1.5365\,eV$ and $E_{UP} = 1.5430\,eV$, respectively. The Rabi-splitting $\hbar\Omega$ is $6.5\,meV$. The exciton-polariton linewidth is around $0.5\,meV$. Figure 2.14(b) displays numerical results for the modulus squared of the confined electric field $|E_z|^2$ of the MC mode within the investigated MC structure in dependence on the depth z. The position of the QWs and the maxima of $|E|_z^2$ spatially overlap. Furthermore, Fig. 2.14(b) reveals an enhancement of $|E_z|^2$ by a factor of over 1000 in comparison to $|E_z|^2$ in air.
Figure 2.14(c) displays the maximal acoustic modulation of the bandgap energy $\Delta E_{G,\,max}$ of the GaAs QWs. Obviously, $\Delta E_{G,\,max}$ is not homogenous for all QW pairs. $\Delta E_{G,\,max}$ varies between $0.8\,meV$ and $1\,meV$ for the third QW pair ($2.3\,\mu m$ below the surface) and the first QW pair ($2.1\,\mu m$ below the surface), respectively. This variation is due to the non-constant depth profile of the SAW energy density (cf. 2.14(d)). The position of the GaAs QWs with respect to the SAW energy density profile is displaced by the blue square in the Fig. 2.14(d). Additionally, numerical calculations showed that the modulation of the energy E_C of the MC mode is approximately one quarter of the modulation of E_G. The latter results in

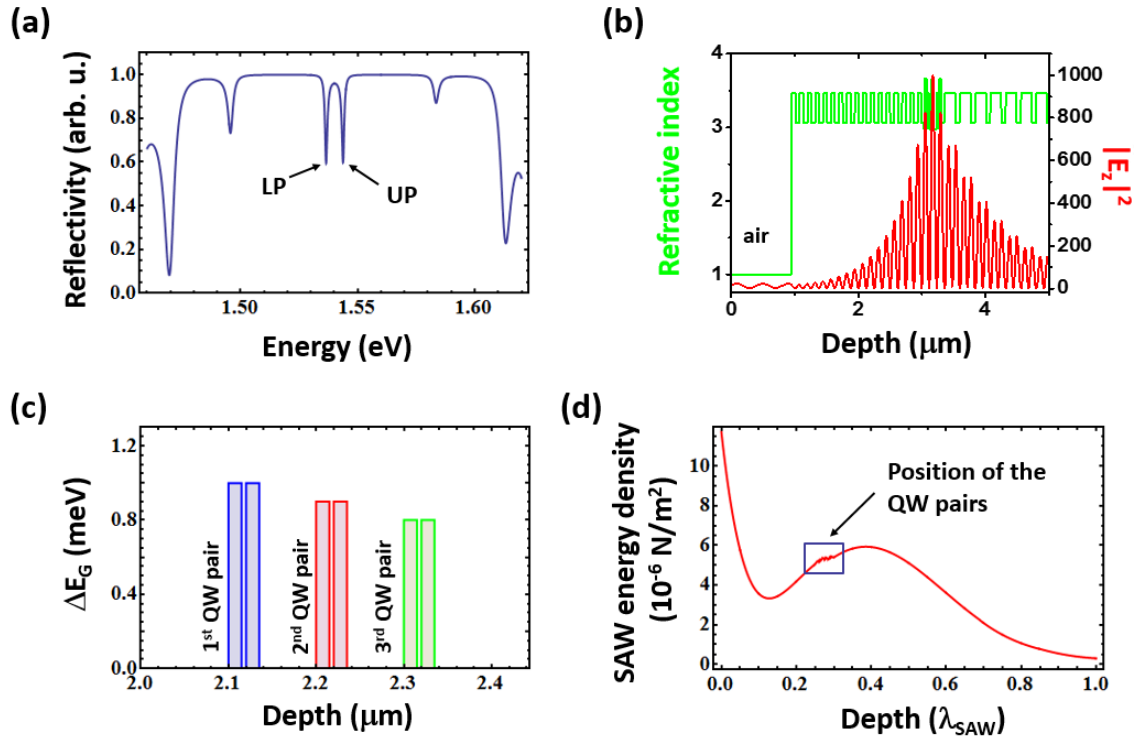

Figure 2.14: (a) Calculated reflectivity spectrum of the investigated MC structure as well as (b) the dependence of $|E_z|^2$ of the MC mode on the depth z. (c) Calculated SAW-induced modulation ΔE_G of the GaAs QWs for the SAW power density $\rho_{SAW} = 100\,\frac{W}{m}$ (ρ_{SAW} is the SAW power per unit length perpendicular to the propagation direction). (d) Depth profile of the SAW energy density

the reduction of the coupling between the QW excitons and the MC mode since the detuning δ between them increases. However, using the coupled oscillator model it can be shown that for small deviations of ΔE_G and ΔE_C compared to the Rabi-splitting Ω, the strong coupling regime is maintained.

Remarks

Note, the upper DBR can be completely or partly replaced by a thin metal layer. Since the dielectric constant of the metal, e.g. gold, is negative, the metal is highly reflective. Already a $30\,nm$-thick gold layer reflects incident light as well as several DBR pairs. However, a gold layer of this thickness is semi-transparent and absorbs light, which results in the broadening of the linewidth of the MC mode. These effects yield MC structures with lower Q-factor. The strong coupling regime can be still maintained but due to the linewidth broadening of the MC exciton-polariton states, their condensation is more difficult to experimentally achieve. In chapter 6 such a MC structure is discussed in detail. It will be shown that the metal layer can lead to the formation of Tamm plasmon polaritons [54], i.e. optical

modes at the interface between metal and a DBR, which can either (i) couple to the MC exciton-polariton states and create new quasi-particles, i.e. Tamm-Plasmon-Exciton-Polaritons (TPEP) [55], [56], or (ii) to mediate the strong coupling between the MC mode and QW excitons resulting in the formation of parametric TPEP states [83]. Such structures open the way to create potential barriers of several meV for exciton-polaritons and at the same time to modulate them with SAWs at higher frequencies, i.e. in the GHz range.

Regarding the homogeneity of the SAW-induced modulation of the GaAs QWs, this can be improved by placing the QWs deeper, i.e. at the depth of approx. $0.4\,\lambda_{SAW}$. At this depth, the slope of the SAW energy density profile is almost zero. Thus, the SAW induced modulation of the bandgap energy of the QWs would be more homogeneous as well stronger since here the SAW energy density is higher than at the depth of $0.25\,\lambda_{SAW}$.

2.5 Condensation of exciton-polaritons

Exciton-polaritons are composite bosons. This property shall enable one to create exciton-polariton condensates. First indications suggesting exciton-polariton condensation in microcavities have been published in Ref. [58], [59], [60]. However, in 2006 Kasprzak *et al.* was the first one to detail a comprehensive set of experiments giving compelling evidence for BEC of exciton-polaritons [57].
It was observed that above a certain (optical) excitation power P_{th}, the critical particle density n_{CR} for condensation of exciton-polaritons was overcome, where all exciton-polaritons have occupied the energetic ground state at the planar momentum $k_{||} = 0$. The spontaneous formation of a coherent state was manifested by an increase of the temporal and spatial coherence as well as by the reduction of the thermal noise. The marked degree of linear polarisation of the condensate emission was measured. These findings varified the spontaneous formation of a macroscopic quantum state (MQS).
In comparison to atomic systems there are several differences (cf. Table 2.1), one can argue whether the exciton-polariton condensation is truly a Bose-Einstein condensation (BEC) since the exciton-polariton system is dissipative and thus, continuous (optical) pumping is necessary to maintain exciton-polariton condensation for a longer period than the exciton-polariton lifetime in the MC. However, the modern understanding of BEC requires the equilibration of the condensing particles and the appearance of the spontaneous temporal and spatial coherence of their phase in the long range regime, i.e. macroscopic dimensions. Note, the concept of the spontaneous appearance of the phase coherence unifies phenomena like BEC, lasing, superfluidity and superconductivity.

Parameter	Atomic system	Exciton-Polariton system
(Effective) mass $[m_e]$	$10^3 - 10^4$	$10^{-5} - 10^{-4}$
Critical temperature T_{CR} $[K]$	$10^{-9} - 10^{-6}$	$1 - 300$
Critical density $[cm^{-2}]$ at T_{CR}	$\sim 10^8$	$\sim 10^8$
de Broglie wavelength at T_{CR}	μm-range	μm-range
Lifetime $[s]$	several	$10^{-12} - 10^{-10}$

Table 2.1: Comparison of the parameters of BEC in atomic and exciton-polariton systems

2.5.1 Requirements for condensation of exciton-polaritons

The necessary requirements for the condensation of bosonic particles, e.g. atoms, excitons or exciton-polaritons, can be obtained by considering their thermal de Broglie wavelength λ_{dB} and their spatial particle separation d. The thermal de Broglie wavelength λ_{dB} states the wavelength of a particle of the mass m at the temperature T:

$$\lambda_{dB} = \sqrt{\frac{h^2}{2\pi\, m\, k_B\, T}}. \tag{2.5.1}$$

When the particle distance d becomes smaller than λ_{dB}, i.e. $d \geq \lambda_{dB}$, the wave functions of the particles overlap (cf. Fig. 2.15). From this point of view, it is obvious that the lighter the particles and lower the temperature, the smaller is the critical particle density n_{CR} for the condensation.
In terms of the experiments, to realise exciton-polariton condensation in planar MCs, the (optical) condensation threshold power P_{th} is a function of the exciton-polariton mass and temperature and the size of exciton-polariton traps. The exciton-polariton traps can be realised by SAWs. Their dimensions are determined the SAW wavelength λ_{SAW}, i.e. $d \sim \frac{1}{2}\lambda_{SAW}$. P_{th} decreases at lower temperatures and/or smaller exciton-polariton masses as well as with smaller the exciton-polariton traps. Note, the condensation may also occur without traps.

Beside the above mentioned facts, the condensation of exciton-polaritons can only occur at certain range of the exciton-polariton particle density. This is due to the bosonic nature of the exciton. The exciton as a part of the exciton-polariton consists of two fermions, i.e. electron and hole. The bosonic character of the exciton is valid in the diluted regime, i.e. when the spatial separation between the electron and hole is much smaller than the distance d between the adjacent excitons. With an increasing density n_X of excitons and thus, of electrons and holes, the Pauli exclusion principle needs be taken into account. As well there are effects of the *phase space filling* and *exchange interactions*. The effect of the phase space filling describes that the electrons and holes occupy all states, which inhibits the creation of the excitons [61], [62]. The exchange interaction results from the interaction of the carriers with the same spin [63], [64].

Excitons can be considered as composite bosons, when

$$n_X \ (a_B)^2 \ll 1. \tag{2.5.2}$$

The saturation density n_X^{sat} above which the excitons cannot be considered as bosons is given by [61], [65]:

$$n_X^{sat} \approx \frac{0.117}{\pi \ (a_B)^2}. \tag{2.5.3}$$

In case of GaAs, $n_X^{sat} \approx 5 \times 10^{10} cm^{-2}$, where the Bohr radius of bulk excitons was applied. For exciton-polaritons in MC, this saturation density can be diluted by using multiple QWs to $n_{QW}^{sat} = n_X^{sat}/N_{QW}$.

To conclude, exciton-polaritons condensate at the particle densities between n_{CR} (lower limit) and n_{QW}^{sat} (upper limit).

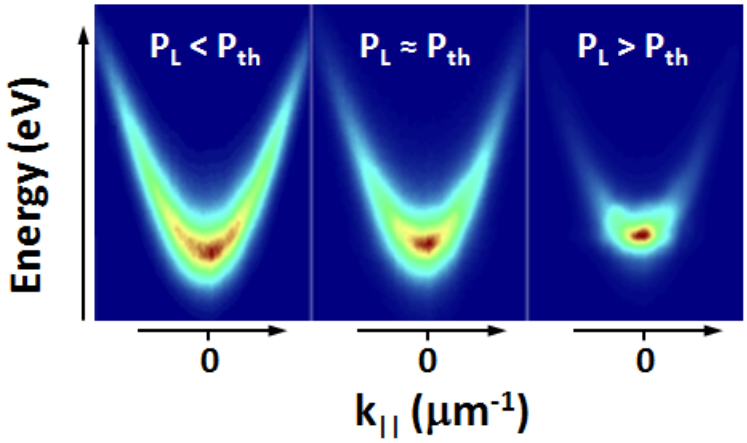

Figure 2.15: Dispersion of exciton-polaritons in a planar MC: lower exciton-polariton branch for small $k_{||}$ shows the energy and momentum distribution of exciton-polaritons at low excitation powers, i.e. below the condensation threshold ($P_L < P_{th}$), around the condensation threshold ($P_L \approx P_{th}$) and above the condensation threshold ($P_L > P_{th}$), where exciton-polaritons occupy one energy state at $k_{||} = 0$ (adopted from [57])

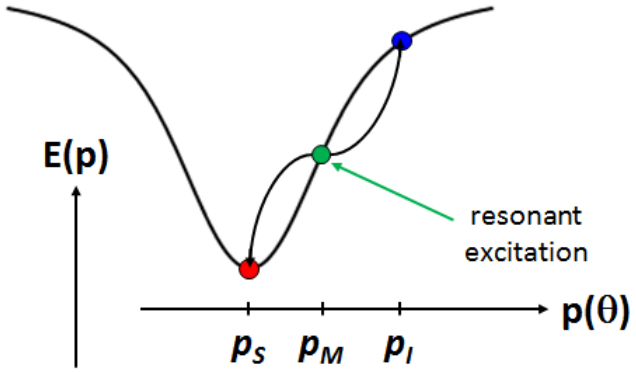

Figure 2.16: Scheme of the stimulated scattering of the pumped state (p_M) into the idler (p_I) and signal state (p_S).

2.5.2 Stimulated scattering

Once the critical particle density n_{CR} is overcome and the exciton-polaritons start to condensate, i.e. populate a common energy state, resonant scattering of the injected exciton-polaritons into such a state becomes strongly enhanced and extremely fast. This process is described as stimulated scattering. Stimulated scattering states that the probability of the scattering of the (injected) exciton-polaritons into a state is proportional to its occupation number [68].

In order to establish resonant polariton-polariton scattering from the pumped state, i.e. point p_M in the Fig. 2.16, into the signal (ground state) and idler state, point p_S and p_I in the Fig. 2.16, respectively, energy and wavevector must be conserved. This process is well known as optical parametric oscillator (OPO). In principle, there is only one such angle that fulfills the latter conditions, the so-called *magic angle* θ_M [66], [67] and [68], which should depend on the curvature of the lower exciton-polariton branch and thus, on the detuning δ. However, in Ref. [69] it is shown that contrary to much previous belief there is no magic angle θ_M for stimulated scattering under continuous-wave conditions. The process is a rather general phenomenon and stimulated scattering may occur over a wide range of pump angles.
Resonantly exciting exciton-polaritons at p_M enables one to directly populate the exciton-polariton condensate. Due to the processes of the stimulated scattering, exciton-polariton condensation has a strong non-linear dependence on the excitation power P_L [65], [67] and [68].

2.5.3 Condensation in a SAW-modulated microcavities

In this work, the used MC structure, i.e. the exciton-polariton system, is weakly modulated by SAWs, where the interference of two to each other perpendicularly

propagating SAWs is used to create a dynamic acoustic square lattice on the MC (cf. Fig. 2.13(a)). In this context, weak SAW modulation creates a weak confinement of exciton-polaritons within the potential minima of the acoustic square lattice, i.e dot-like areas in Fig. 2.13(b). Therefore, the condensation in such a system is discussed here. This sets the basis of this work as well as the motivation of the investigated aspects presented in the following Chapter 4. For completeness, the reader is referred to [70], [71], [72],[73] and [74] to review the exciton-polaritons properties and their condensation under modulation by one SAW.

As previously pointed out, under the SAW modulation the exciton-polariton dispersion is folded due to the periodic nature of SAWs [32], [74], [75]. Energy gaps arise between the exciton-polariton states. When the (optical) excitation power P_L is increased to or above the (optical) condensation threshold P_{th}, i.e. $P_L = P_{th}$, one observes that the exciton-polaritons occupy the energy state at the planar wavevector $k_{||}$ at the edges, i.e. here the M-points, of the first MBZ (cf. Fig. 2.17(a)-(b)). Thus, the critical particle density is overcome first here and not at the Γ-point of the MBZ, triggering the stimulated scattering into the M-points (cf. Fig. 2.17(b)) [75].

Remarkably, exciton-polaritons in a weak acoustic square lattice condensate not at the energetic ground state at $k_{||} = 0$ but at higher energy. Thus, the exciton-polariton condensate is in an excited state. The corresponding physical explanation lies in the effective mass m^* of the exciton-polaritons. Namely, due to the dispersion curvature of exciton-polariton at the M-points, their effective mass is negative, i.e. $m^* < 0$, and thus, their kinetic energy E_{kin} is negative ($E_{kin} < 0$), since $E_{kin} = \frac{\hbar^2 k_{||}^2}{2m^*}$. The repulsive polariton-polariton interaction energy E_{pot} reads

$$E_{pot} = \frac{N_{XP}\, g}{r_{XP}^2}, \tag{2.5.4}$$

where N_{XP} is number of exciton-polaritons within the area of the radius r_{XP} and $g > 0$ is exciton-polariton interaction constant. At the M-points, the kinetic energy E_{kin} is compensated by the potential energy E_{pot} in such a way that exciton-polariton energy is constant across the spatial soliton profile in real-space. This leads to the spatial self-localisation of the condensate. Additionaly, numerical studies showed that the energy of the condensate lies within the single particle bandgap ΔE_G^{XP} of the exciton-polariton dispersion (cf. Fig. 2.10(a)). This type of the exciton-polariton condensate is a two-dimensional (2D) state and was dubbed as *exciton-polariton gap soliton* (2D GS) in analogy to gap solitons in atomic systems [75], [76].

2D GS is an extended state over several lattice periods as shown in Fig. 2.18. Figure 2.18 shows the time- and energy-integrated real-space image of the 2D GS at the optical condensation threshold, i.e. $P_L = P_{th}$. The white arrow indicates the velocity $\mathbf{v}_{lat}$ of the acoustic square lattice. 2D GS is symmetric having a diameter d_{GS} of approximately $3\lambda_{SAW}$. At $P_L = P_{th}$, the coherence length L_{coh} (white dashed circle in Fig. 2.18) corresponds to d_{GS}. The coherence length is deduced from the

full width at half maximum (FWHM) of the PL peaks at the M-points using the Heisenberg's uncertainty principle [77], [78]. According to the latter, $\Delta k\, L_{coh} \geq 2\pi$, where Δk is the FWHM of the PL peaks at the M-points in the k-space (cf. Fig. 2.17(b)).

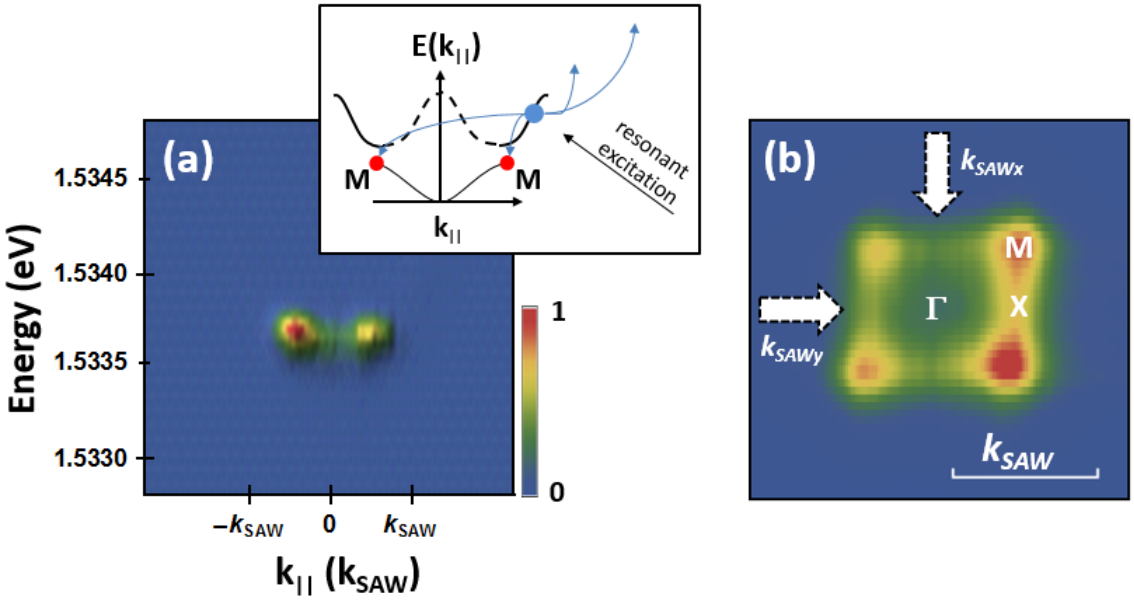

Figure 2.17: (a) Experimentally recorded time-integrated 2D GS dispersion at the condensation threshold P_{th} and (b) the corresponding full momentum image. The inset of (a) schematically illustrates the corresponding stimulated scattering. The intensity scale in (a) applies as well to (b).

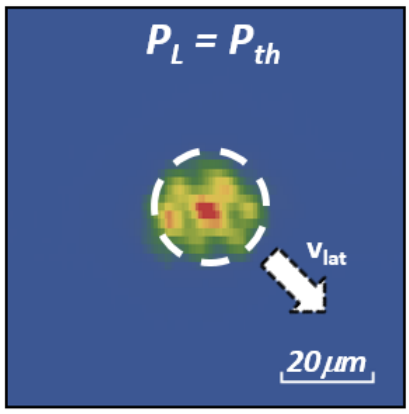

Figure 2.18: Time- and energy-integrated real-space image of the 2D GS at the condensation threshold P_{th}. The white dashed circle represents its coherence length. The intensity scales are the same as in Fig. 2.17(a).

Chapter 3

Motivation for this work

A deeper investigation of the exciton-polariton condensation in SAW-modulated MCs and in particular the 2D GS formation in square lattices described in the Subsec. 2.5.3 reveals novel phenomena. Namely, (i) the dependence of the 2D GS size and its coherence length on the excitation power P_L and the size ϕ_L (quantified by the full width at half intensity maximum (FWHM)) of the laser spot and (ii) the presence of static patterns in the real-space images of the 2D GS. The latter indicates a square lattice periodicity of $\lambda_{SAW}/2$, which is obviously in contrast to the applied SAW wavelength λ_{SAW} as well as to the corresponding k-space images. From the k-space images of the 2D GS it can be clearly deduced a square lattice constant of λ_{SAW} as will be discussed in the following.

Dependence of the 2D GS size and coherence length

The 2D GS is formed at laser excitation powers P_L at and above the optical condensation threshold P_{th}, i.e. $P_L \geq P_{th}$. Interestingly, it is to note that the 2D GS has symmetric dimensions d_{GS} in real-space as well as a coherence lengths L_{coh}, which corresponds well to d_{GS}, i.e. $L_{coh} = d_{GS}$. However, this is only true for the excitation powers at or slightly above P_{th} as displayed in the Fig. 3.1. When the excitation power is increased above the optical condensation threshold, i.e. $P_L > P_{th}$, the 2D GS size increases as shown in the Fig. 3.1(b). In contrast, its coherence length (white dashed circle in Fig. 3.1) estimated from the corresponding momentum-space images remains almost unchanged, i.e. $L_{coh}(P_L = P_{th}) \approx L_{coh}(P_L > P_{th})$. At this point, a question arises whether several 2D GS states are formed spatially next to each other or whether different types of the exciton-polariton condensates are created together with the 2D GS and at which energies? To address this question, tomography-like measurements were performed, where the real- and momentum (k-) space of the 2D GS is spectrally resolved as a function of the excitation power P_L, the size ϕ_L of the laser excitation spot and the SAW power P_{RF}. From the current theoretical framework, the following can be predicted:
From Eq. 2.5.4 one expects that the 2D GS size should increase with increasing excitation power P_L and/or with increasing size ϕ_L of the excitation spot, since in a first approximation one has: $N_{XP} \propto P_L$ and $N_{XP} \propto \phi_L^2$. The latter relation is

valid by assuming that the number N_{XP} of the injected exciton-polaritons is directly proportional to the photon density in the area illuminated by the excitation laser spot. Correspondingly, when P_L and/or ϕ_L increase, the 2D GS radius r_{XP} and its coherence length L_{coh} should also increase in order to keep E_{pot} constant and thus, to maintain the necessary condition $\partial(E_{kin} + E_{pot}) = 0$ for the 2D GS formation. From this assumption, there can be only one 2D GS growing with increasing P_L and/or ϕ_L. However, for $P_L \gg P_{th}$ the experimental results (cf. Fig. 3.1(b)) show a different picture since the linear relation between N_{XP} and P_L seems not hold at high P_L.
With the increase of the spatial confinement, which is set by the increase of the SAW power P_{RF}, the effective exciton-polariton mass m^* increases and thus, reduces E_{kin}. Consequently, to maintain the 2D GS formation E_{pot} must decrease as well, i.e. decrease of N_{XP}, r_{XP} and L_{coh}. The increase of m^* originates in the flattening of the exciton-polariton dispersion.

Investigation of the square lattice constant

The time- and energy-integrated real-space image (cf. Fig. 3.2(a)) reveals that the traces of the propagating potential minima of the SAW induced square lattice are not continuous as it is to expect, i.e. continuous diagonal lines in the inset of the Fig. 3.2(a). On one hand, the traces seem to be interrupted and one may even see an array of dot-like areas in Fig. 3.2(a), which are spatially separated by approximately $\lambda_{SAW}/\sqrt{2}$ from each other and correspondingly, indicating a lattice periodicity of $\lambda_{SAW}/\sqrt{2}$. On the other hand, the corresponding full k-space image (cf. Fig. 3.2(b)) shows that the PL is being emitted from the M-points, which are at $(k_x, k_y) = (\pm 0.39\,\mu m^{-1}, \pm 0.39\,\mu m^{-1})$, confirming a lattice periodicity of $\lambda_{SAW} = 8\,\mu m$ ($k_{SAW} = 0.78\,\mu m^{-1}$ and $\frac{2\pi}{k_{SAW}} = 8\,\mu m = \lambda_{SAW}$). In order to address this contradiction, time-resolved measurements of the 2D GS dynamics in real- and k-space have been performed using a streak-camera set-up [82]. Additionally, time-resolved measurements allow one to directly probe the dynamics of the 2D GS, i.e. the evolution of its wavefunction in time.

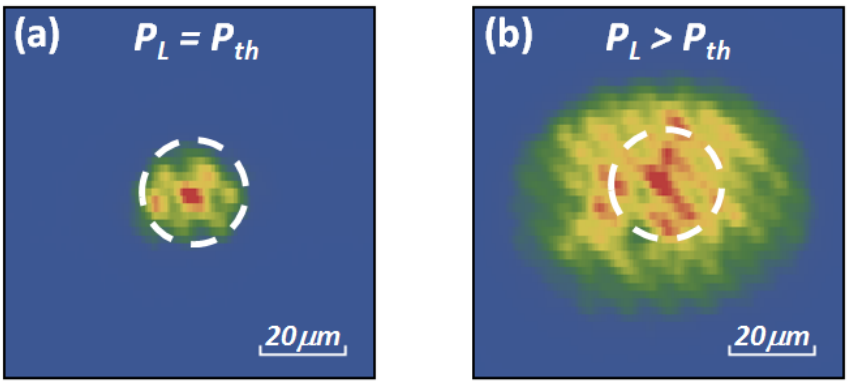

Figure 3.1: Time- and energy-integrated real-space image of the 2D GS (a) at the condensation threshold P_{th} and (b) above P_{th}. The white dashed circles show the coherence lengths of the 2D GS calculated from the corresponding k-space images. The intensity scales are the same as in Fig. 2.17(a).

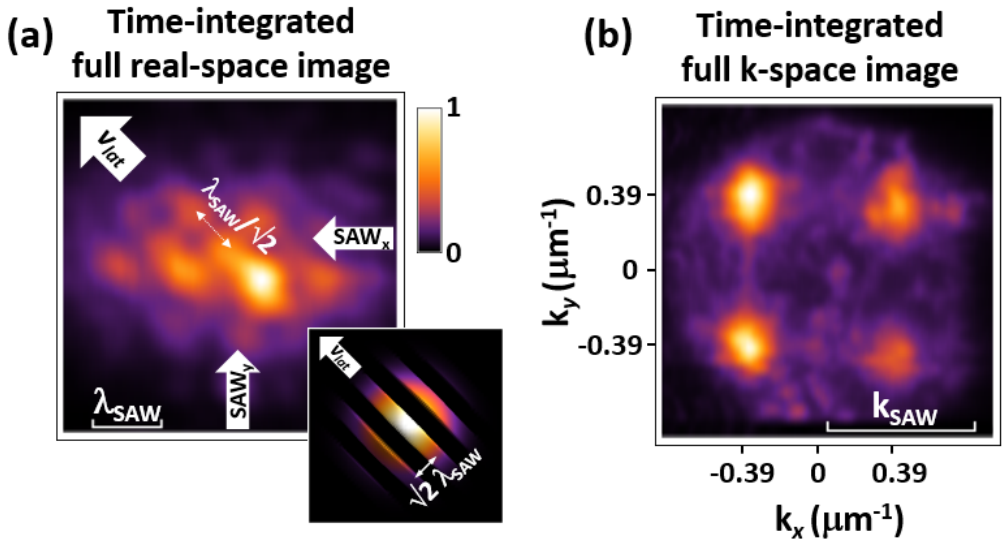

Figure 3.2: Time- and energy-integrated (a) real- and (b) k-space image of the 2D GS at the condensation threshold P_{th}. The inset shows the expected time-integrated real-space image.

Chapter 4

Experimental work

Before the experimental results are presented and discussed in detail, the experimental details are described, first in general form and later for each experiment separately in the corresponding Subsections. This gives the reader the option to see the experimental details at a glance as well as the specific details for each of the experiments.

The experimental findings of this work have been published in [81] and [82].

4.1 General experimental details

The experiments were performed on an (Al,Ga)As-based $3\lambda/2$-MC with 6 embedded $15\,nm$-thick GaAs QWs (cf. Fig. 2.13). All measurements have been carried out at cryogenic temperatures, i.e. $T = 8\,K$. As described in the previous Subsec. 2.4.2, the MC active region is sandwiched between two highly reflective DBRs. The Q-factor of the MC is around 2000. The resonance wavelength of the confined optical mode in the MC is $\lambda_C = 808\,nm$ (in vacuum). Since the exciton energy in the $15\,nm$-thick GaAs QW is around $1.54\,eV$ at $T = 8\,K$ (corresponding to a wavelength in vacuum of $805\,nm$), the experimentally investigated MC structure is negatively detuned. The Rabi-splitting amounts to $6\,meV$. Thus, when exciton-polaritons are created in such a structure, they possess a bigger photonic component in the lower exciton-polariton branch yielding a lower effective mass and a shorter lifetime.
The GaAs QWs are divided into 3 pairs spatially placed at the antinodes of the electric field of the confined MC mode along the z-direction (cf. Fig. 2.14) as well as close to the SAW strain field maximum. On top of the MC structure a $170 \times 170\,\mu m^2$ sinusoidal acoustic square lattice is generated by the interference of two perpendicularly propagating SAWs along the two non-piezoelectric directions, i.e. [100] and [010], on the (001) orientated GaAs substrate. In the experiment, both SAWs are excited by interdigital transducers (IDTs) fabricated on $600\,nm$-thick piezo-electric ZnO islands. The IDTs were excited with the same phase and radio-frequency (RF) $f_{SAW} = 370\,MHz$, corresponding to $\lambda_{SAW} = 8\,\mu m$ and a SAW period $T_{SAW} = 2.7\,ns$. The nominal SAW velocity v_{SAW} in GaAs is aproximately

$3\,\mu m/ns$. The acoustic square lattice moves with the velocity v_{lat} given by $v_{lat} = \sqrt{2}v_{SAW}$. The device used in the experiments is displayed in the Fig. 4.1(a) and (b). There are two working IDTs, which are highlighted by red and green colours and denoted as IDT L and R, respectively. Both working IDTs face either the sample edge or a broken IDT. Due to this, once SAWs are launched, there will be SAW reflections, which will be of importance for the Sec. 4.3. The SAW reflections interfere with the initially generated ones and in this way they modulate the total amplitude Φ_{SAW} of the acoustic square lattice.
The origin of SAW reflections coming from the broken IDT opposite to IDT L is clear, whereas the origin of SAW reflections of IDT R require a greater insight into the nature of the preparation of the sample. One of these preparation steps is the cleavage of the sample, which results in the roughness of the sample edges. Here, on one hand the sample edge causes reflections of the incident SAWs due to the strong change of the material refractive index, i.e. AlGaAs $\leftrightarrows$ air, and on the other hand reflected SAWs will be dispersed in all spatial directions due to the roughness of the sample edge.
For both working IDTs, the distances d_L and d_R between the centre of the RF-driven IDT and the centre of opposing IDT or the sample border, respectively, are approximately $4.7\,mm$. The amplitude of the reflected SAWs was measured using a network analyser with Fourier-Transform capabilities to record time-resolved profiles for the RF-reflection coefficient (s11). Figure 4.2 shows the time-dependent impulse response for the (s11) reflection coefficient of the excited IDT. The reflection for delays $0 < t < 1\,\mu s$ is generated while the SAW excited by the impulse propagates along the $2.8\,mm$ long RF-driven IDT. The echos centred at $\tau \approx 3\,\mu s$ are attributed to the acoustic reflection of the SAW pulse at the opposing IDT and/or sample border. In fact, the echo delays correspond to twice the SAW propagation time of d_L and/or d_R. From the amplitude ratio between the echo and the first peak in Fig. 4.2, the ratio r_{RF}^R between reflected and incident RF-powers is estimated to

$$r_{RF}^R = \frac{10^{-\frac{76}{10}}}{\frac{1}{2}10^{-\frac{41}{10}}} \approx 6.3 \times 10^{-4}. \tag{4.1.1}$$

Due to the read-out inaccuracy of the RF-power values, the error Δr_{RF}^R in r_{RF}^R is 4.1×10^{-4}. The factor of $\frac{1}{2}$ in the denominator accounts for the fact that the RF-driven IDTs generate SAWs in two opposite directions. The SAW amplitude Φ_{SAW} is proportional to the square root of the RF-power P_{RF}, i.e. $\Phi_{SAW} \propto \sqrt{P_{RF}}$. Thus, the peak-to-peak amplitude of the acoustic reflections is $2\sqrt{r_{RF}^R} \approx (5.0 \pm 1.7) \times 10^{-2}$. Furthermore, the interference of the reflected SAWs with the incident ones induces regions of higher acoustic modulation amplitude at the anti-nodes of the incident SAWs, which in a square acoustic lattice are separated from each other by $\lambda_{SAW}/\sqrt{2}$.

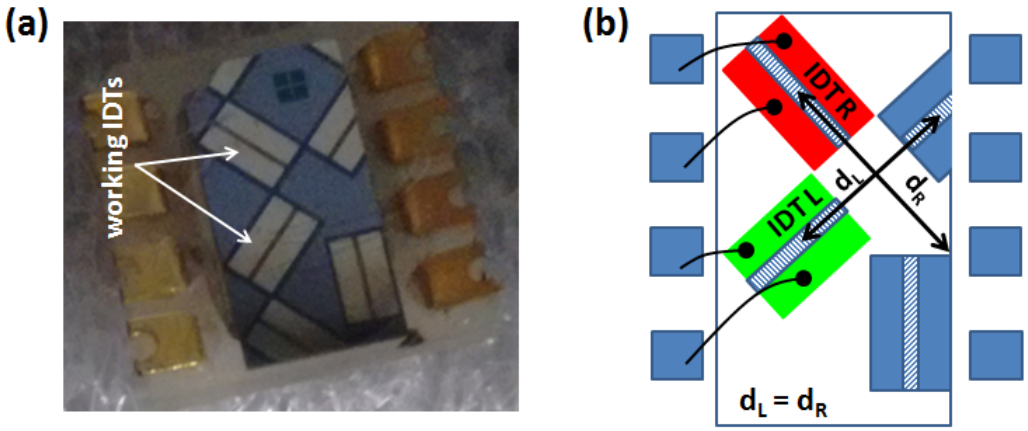

Figure 4.1: Photo of the sample device mounted on a chip holder

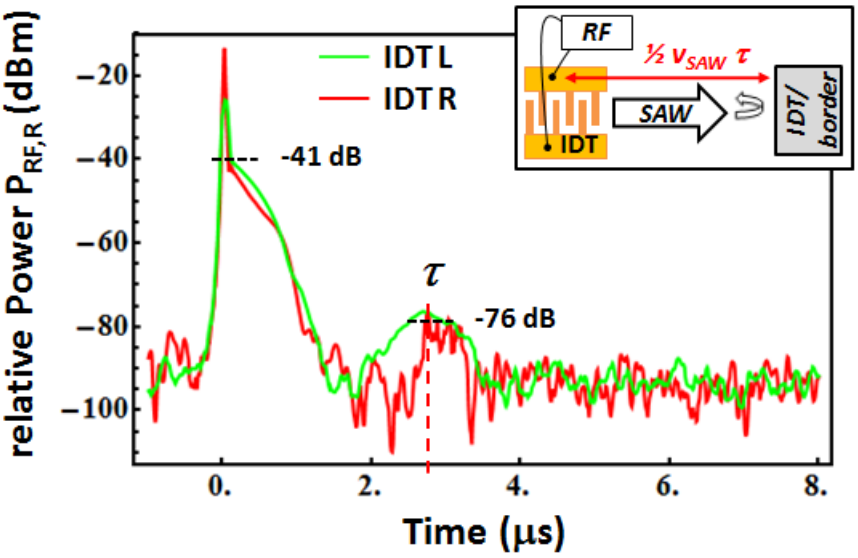

Figure 4.2: Impulse response of the radio-frequency (RF) power reflection coefficient of the working interdigital transducers (IDTs) recorded in the configuration displayed in the inset. The broad peak for delays $0 < t < 1\,\mu s$ is generated while the SAW propagates through the $2.8\,mm$ long excited IDT. The echo centred at $t = \tau$ is caused by SAW reflections at the opposing IDT and/or at the sample border (cf. inset). The distance $v_{SAW}\tau$ corresponds to twice the distance between the centre of the IDT and the reflection point.

Exciton-Polaritons were resonantly excited in an optical parametric oscillator (OPO) geometry (cf. Fig. 2.16) using a tunable, continuous-wave, single-mode Ti:Sa laser with a Gaussian intensity profile. The polarisation of the laser was linear. The laser energy was set to $E_{laser} = 1.5353\,eV$ and its angle of incidence to 13°, i.e. the magic angle, or in terms of the laser planar wavevector $\mathbf{k_P} = (k_x, k_y) = (0, 1.7)\,\mu m^{-1}$, in order to match the lower exciton-polariton dispersion branch. To remind the reader, real- (r-) and momentum (k-) space images were recorded in analogy to the described techniques shown in the Figs. 2.6 and 4.5. The k-space images were obtained by measuring the exciton-polariton photoluminescence (PL) with angle resolution, since the emission angle θ is directly related to their planar wavevector $k_{||}$ by $k_{||} = k\,\sin(\theta)$, where $k = 2\pi/\lambda_{PL}$ is the total momentum of the emitted PL of exciton-polaritons and λ_{PL} its wavelength.
Figures 4.3(a) and (b) displays the lower exciton-polariton dispersion branch probed by k-space maps and the corresponding real-space image, respectively, when both SAWs are launched, for an exciting laser power, which is below the exciton-polariton condensation threshold P_{th}. Figures 4.3 (c) and (d) show the exciton-polariton dispersion when only one SAW is excited. When the SAW propagates parallel to the slit of the spectrometer, one observes the folding of the exciton-polariton dispersion into mini-Brillouin zones (MBZ) created by the periodic SAW. The SAW wavelength λ_{SAW} determines the dimension of MBZ, which is $k_{SAW} = \frac{2\pi}{\lambda_{SAW}}$. The folding is analog to the electron dispersion in a crystal (cf. Fig. 4.3(c)). When the SAW propagates perpendicularly to the spectrometer slit (cf. Fig. 4.3(d)), the dispersion appears to be shifted in energy. These energy shifts result from the folding of the dispersion, too. The formation of energy bandgaps originates in the anti-crossing of the folded energetic levels, which are clearly observable. Accordingly, the exciton-polariton dispersions presented in Fig. 4.3(d) are just dispersions in Fig. 4.3(c) along the non-modulated direction of the 1st MBZ, 2nd MBZ and so on.
When both SAWs are applied, the previously discussed dispersions overlap and create dot-like potentials in the real-space as shown in Fig. 4.3(a) and (b), respectively. By increasing the laser power P_L, exciton-polariton will condensate once the optical condensation threshold power P_{th} is overcome, i.e. $P_L \geq P_{th}$. It is to notice that the excitation of the exciton-polariton condensate can only be performed within a narrow window of the exciting laser energy. Figure 4.4 displays energy- and time-integrated k-space images and the dependence of the formation of the exciton-polariton condensate on the exciting laser energy E_{laser}. The condensate is only resonantly excited at one angle of incidence of the exciting laser beam with a certain E_{laser} corresponding to the magic angle (cf. Fig. 4.4(b)). A variation by $1\,meV$ of E_{laser}, while keeping the laser power and its angle of incidence fixed, is already big enough to leave the resonant excitation conditions. If the laser energy is lowered, no condensate will be formed (cf. Fig. 4.4(a)). Whereas an increase of the laser energy results in an accumulation of exciton-polaritons at the Γ-point of the MBZ (Fig, 4.4(c)). Also the position of the illuminated area on the sample determines the resonance conditions. The MC has not a homogeneous thickness. The MC was cleaved out from a wafer, which was rather thicker at its centre than

on the borders. Thus, there is a gradient of the MC thickness, i.e. wedge, and consequently, there is a spatial dependence of the detuning δ of the exciton-polariton dispersion. Measurements showed that δ roughly varies by $1\,\frac{\mu eV}{\mu m}$.

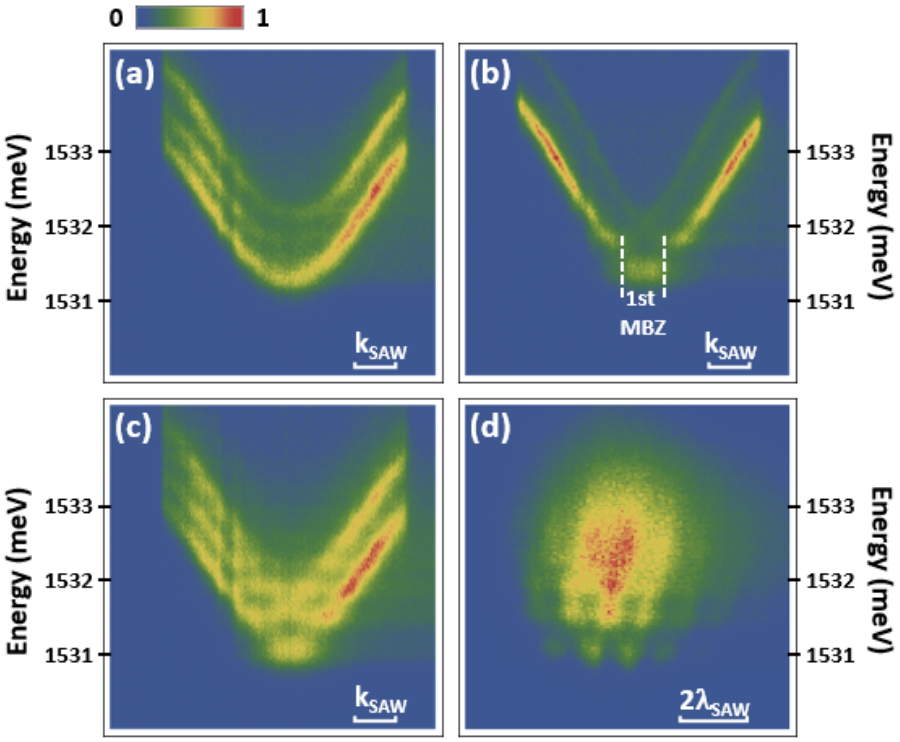

Figure 4.3: Excitation of the exciton-polaritons for laser powers P_L below the exciton-polariton condensation threshold P_{th}. (a) and (b) display the k- and real-space, where both SAWs are generated, respectively. Each SAW power P_{RF} was set to $50\,mW$ and the SAW wavelength λ_{SAW} was $8\,\mu m$. (c) shows the lower exciton-polariton dispersion when only a SAW, which is parallel to the spectrometer slit, is generated, whereas in (d) only a perpendicular SAW is excited.

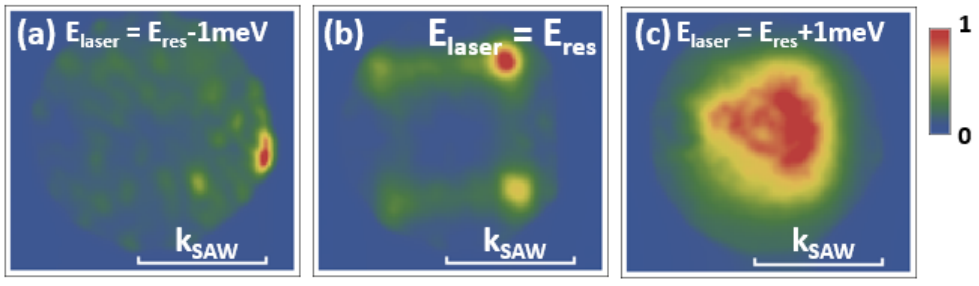

Figure 4.4: Dependence of the excitation of the exciton-polariton gap soliton (2D GS PL) on the laser energy E_{laser}. The intensity scale is the same for all images. The angle of incidence (13°) and the power of the exciting laser beam was kept constant.

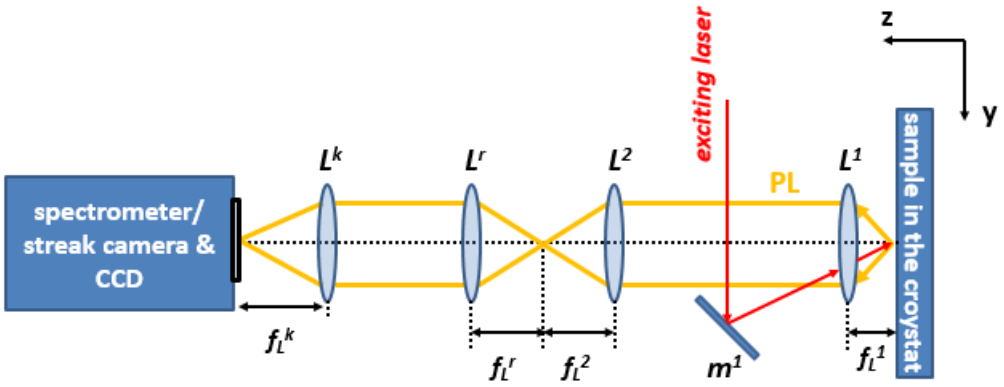

Figure 4.5: One part of the scheme of the experimental set-up showing the path of the emitted light by the sample to the CCD in order to obtain a real-space image

The laser power in the experimental set-up was controlled by the use of the combination of a $\lambda/2$-plate and a polariser. For linearly polarised light, the $\lambda/2$-plate rotates its polarisation vector and thus, the intensity of the light passing through the following polariser changes according to the Malus' law. The angle of incidence of the exciting laser light was set by the mirror m^1 (cf. Fig. 4.5) and focused by an objective L^1 with a focal length f_{L^1} of $5\,cm$. The emitted PL by the sample additionally passed through a lens L^2 with $f_{L^2} = 100\,cm$ and was collected by the lenses L^r and/or L^k for imaging of the real- or k-space, respectively. In this way, the exciton-polariton PL was collected from the sample top surface and was imaged with either spatial or angular (i.e. in-plane momentum) resolution onto a charged coupled device (CCD) [79] at the output port of the spectrometer or the streak-camera. In total, the real- and k-space images were magnified by $\frac{f_{L^2}}{f_{L^1}} \times \frac{f_{L^k}}{f_{L^r}}$ and $\frac{f_{L^k}}{f_{L^2}}$, respectively, before recorded by the CCD. The photo of the experimental set-up is shown in Fig. 4.6.

The illumination of the sample by the laser as well as the generation of SAWs by IDTs heats up the sample. In order to eliminate this heating effect, a chopper was used to trigger the laser and the RF-power supplied to the IDTs with a duty cycle of 10%. The frequency of the chopper was set to $100\,Hz$.

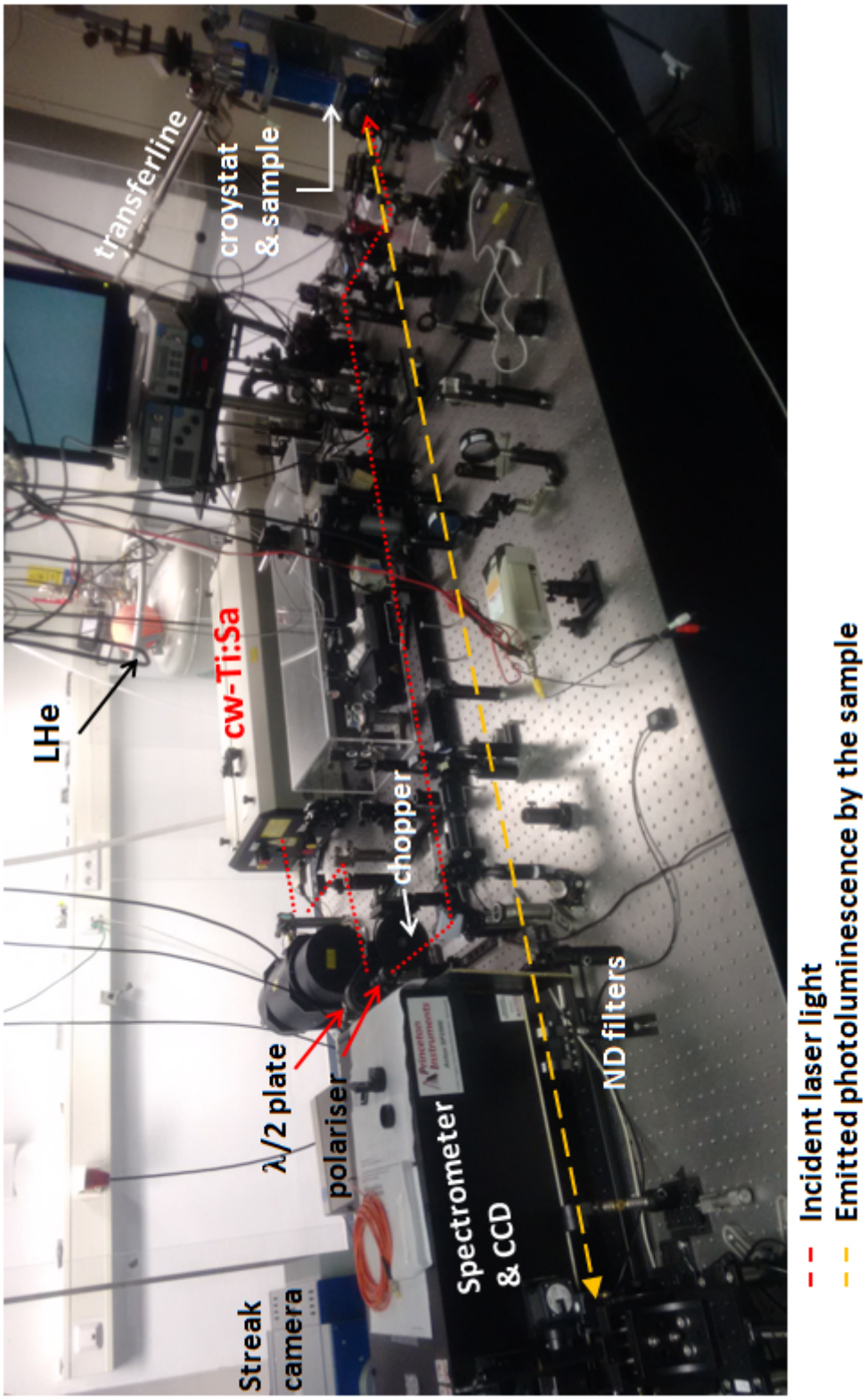

Figure 4.6: Photo of the experimental set-up

4.2 Structure of Exciton-Polariton Condensates in Acoustic Square Lattices

The properties of the exciton-polariton condensates, such as energy, size and coherence length, were measured as a function of the laser excitation power P_L, the SAW power P_{RF} and the size ϕ_L of the exciting laser spot (quantified by the full width at half intensity maximum (FWHM)). The experimental findings show that beside the formation of the 2D GS states, one may form additional solitonic states, which have similarities to 2D GS. These observed solitonic states are one-dimensional (1D), in contrast to the two-dimensional (2D) GS states, and are dubbed in the following discussions as 1D macroscopic quantum states (MQSs). 1D MQSs exist in a wide range of P_L, P_{RF} and the size ϕ_L of the laser spot.
The experimental results are presented and discussed in the following Subsection. First, the experimental details are described. Then, the dependence of the 2D GS and 1D MSQs on the laser power P_L is presented. Additionally, the dependence of the 1D MQSs and 2D GS properties on the SAW power P_{RF} is discussed and finally, the corresponding results are shown for two different sizes ϕ_L of the laser spot. The formation of 2D GS and 1D MQSs is supported by a theoretical model described in Subsec. 4.2.5.

4.2.1 Experimental details of the energy-resolved measurements

The exciton-polariton PL was collected from the sample top surface and imaged with spatial and angular, i.e. planar wavevector $k_{||}$, resolution onto a charged coupled device (CCD) at the output port of a spectrometer. When the input slit of the spectrometer (vertically oriented in Fig. 4.7) was fully open and its dispersion grating set to zero-order diffraction, energy- and time-integrated real- or k-space images of the PL could be obtained (cf. Figs. 2.17(b) and 2.18).
When the slit was closed and the spectrometer grating was set to first-order diffraction, the previous procedure was applied to record spectral information of a cross-section of the real- or k-space image, which was defined by the slit of the spectrometer (cf. Fig. 4.7).
In order to obtain full energy-resolved real- and k-space images, i.e. to obtain 2D maps of the PL in the real- and k-space at all energies, the collected PL was scanned across the slit of the spectrometer by moving a lens L^k, i.e. the first lens in front of the spectrometer (cf. Fig. 4.5). In this way, the image was moved with respect to the slit (black arrows in Fig. 4.7 and 4.8) and divided into several image sections, which were energy-resolved and recorded. Thus, an additional spatial dimension was yielded [80]. Using this procedure, six-dimensional maps of the PL emission were obtained providing information on the spatial dimensions (x, y), planar wavevectors (k_x, k_y), energy E and PL intensity I_{PL} of the exciton-polaritons. The principle of the tomography measurements and the described technique is illustrated in the Fig. 4.8.

Before the experiments the spectrometer was calibrated using a calibration lamp. The spectral resolution was determined to be approx. $60\,\mu eV$. The resolution of the full real- and k-space images was set by the pixel size of $20\,\mu m \times 20\,\mu m$ of the CCD as well as by the optical magnification of the real- and k-space images and the step size of the lens L^k of $50\,\mu m$. In the experiment, the spatial resolution in the x-direction was $0.75\,\mu m$ and $1.85\,\mu m$ in the y-direction. The corresponding k-space resolution was $1.6 \times 10^{-2}\,\mu m^{-1}$ in k_x-direction and $4.6 \times 10^{-2}\,\mu m^{-1}$ in k_y-direction.

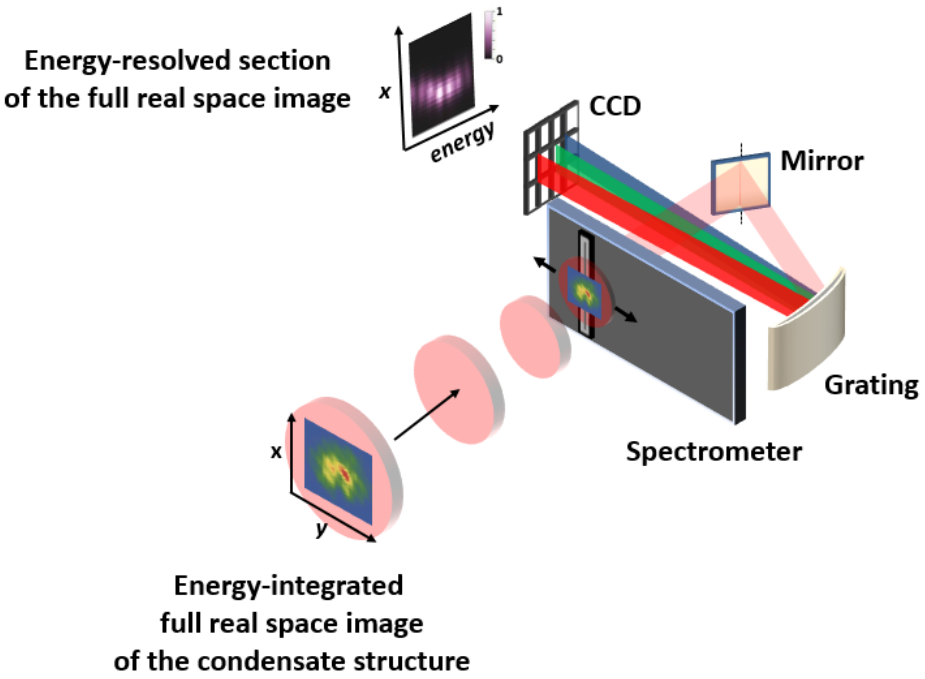

Figure 4.7: Scheme of the experimental set-up for the energy-resolved polariton imaging

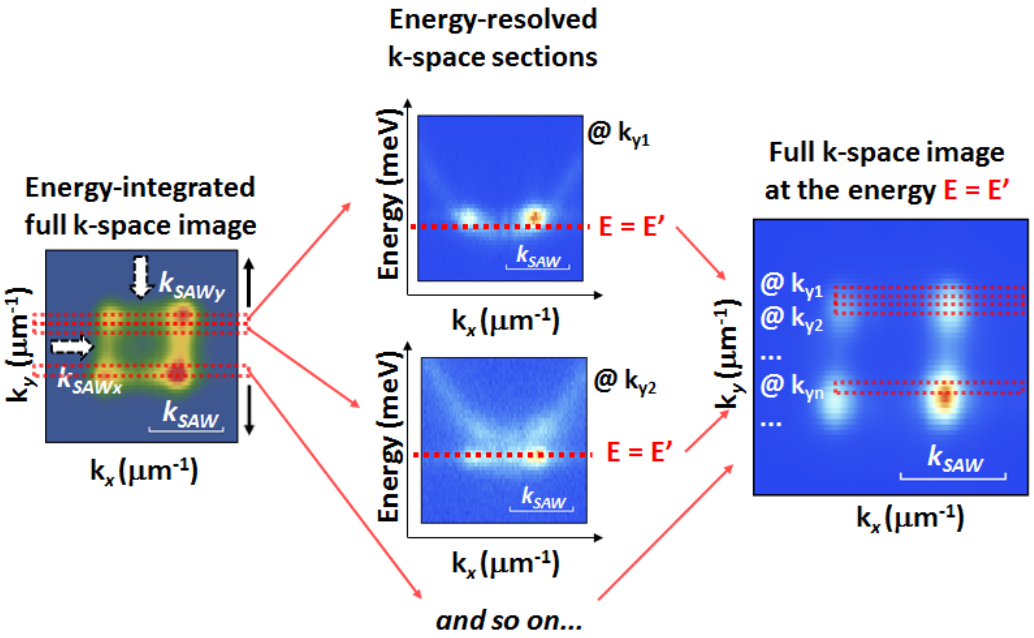

Figure 4.8: Principle of the reconstruction of the energy-resolved images from the recorded energy-resolved image sections

4.2.2 Energy-integrated results

In order to investigate the structure of the exciton-polariton condensate(s) in the acoustic square lattice potential, first the optical condensation threshold power P_{th} was determined. For that purpose, the total emitted energy-integrated PL intensity I_{PL}^{total} from the area of the condensate was measured and integrated. Figure 4.9 shows the emitted PL intensity I_{PL}^{total} in dependence on the laser power P_L. These results were acquired for $P_{RF} = 25\,mW$. Clearly, there is a significant increase of the PL intensity for $P_L \geq 35\,mW$ and thus yielding, $P_{th} = 35\,mW$. Since the size of the used laser spot was $70\,\mu m$, the corresponding power density ρ_L amounts roughly to $28\,\frac{\mu W}{\mu m^2}$. The total power of exciton-polariton condensate(s) emission amounted to $350\,\mu W$. Correspondingly, the total number of exciton-polaritons emitted in one second must be approx. $1,4 \times 10^{15}$, if a central emission energy of exciton-polaritons is assumed to be around $1534\,meV$ as can be extracted from Fig. 4.10.
The insets show energy- and time-integrated real- and k-space images for $P_L = P_{th}$. The white arrows represent the directions of the SAWs and the lattice in the k- and real-space images, respectively. The k-space image clearly displays the luminescence from the M-points of the MBZ, thus, proving that the 2D GS state was excited. In addition, the real-space image reveals that the 2D GS is symmetric in space and consists of diagonal lines tracing the position of the SAW potential minima along the propagation direction of the acoustic square lattice. The PL intensity distribution of the 2D GS, which is the highest at its centre, directly reflects the Gaussian intensity profile of the exciting laser spot. Furthermore, the white dashed circle in the real-space of the inset highlights the calculated coherence length L_{coh}^{GS} of the condensate. L_{coh}^{GS} was estimated to be approximately $24\,\mu m$ and was determined from the FWHM of the k-space peaks using the Heisenberg's Uncertainty Principle as described in Subsec. 2.5.3. This value agrees well with the spatial extension of 2D GS. This is a first evidence that under the used excitation conditions only one 2D GS is formed. In order to concrete this, the emitted exciton-polariton PL was spectrally resolved (cf. Fig. 4.10). Interestingly, the total linewidth of the emitted PL intensity of the exciton-polariton condensate structure is on the order of $100\,\mu eV$ and thus, it is larger than one would expect, since a condensate theoretically occupies only one energy state. The following more detailed study unveils that the exciton-polariton condensate has a rich structure and actually consists of several MQSs accompanied by a low incoherent background originating from the Γ-point in the k-space.

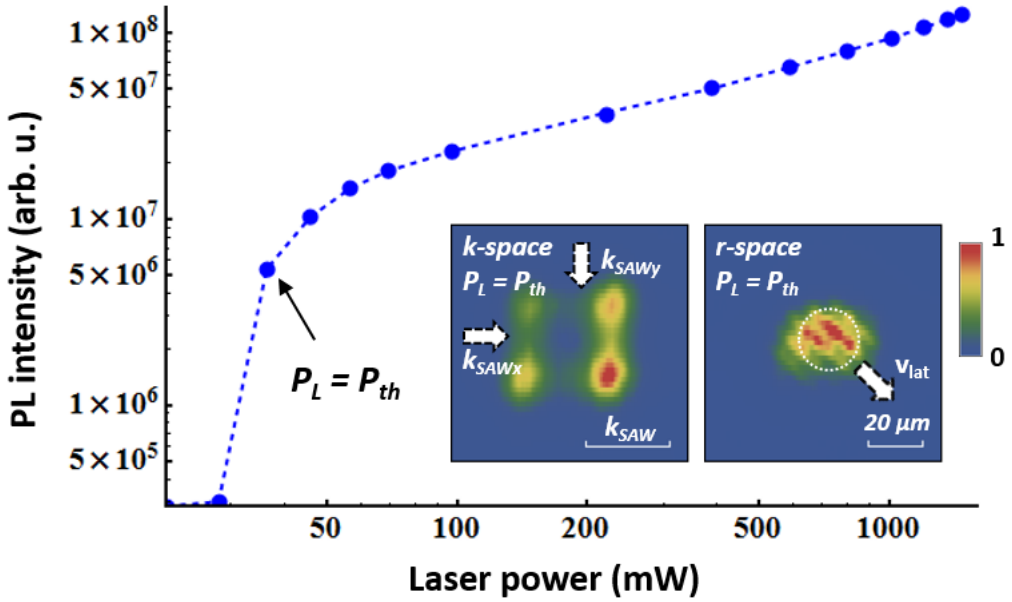

Figure 4.9: Dependence of the energy- and time-integrated PL intensity I_{PL}^{total} of the whole condensate structure on the laser power P_L allows one to identify the optical condensation threshold P_{th}, which is $P_{th} = 35\,mW$. The dashed line is a guide for the eye. The insets show energy-integrated real- and momentum-space images of the condensate at $P_L = P_{th}$. The arrows represent the SAW and the lattice directions in the k- and real-space images, respectively.

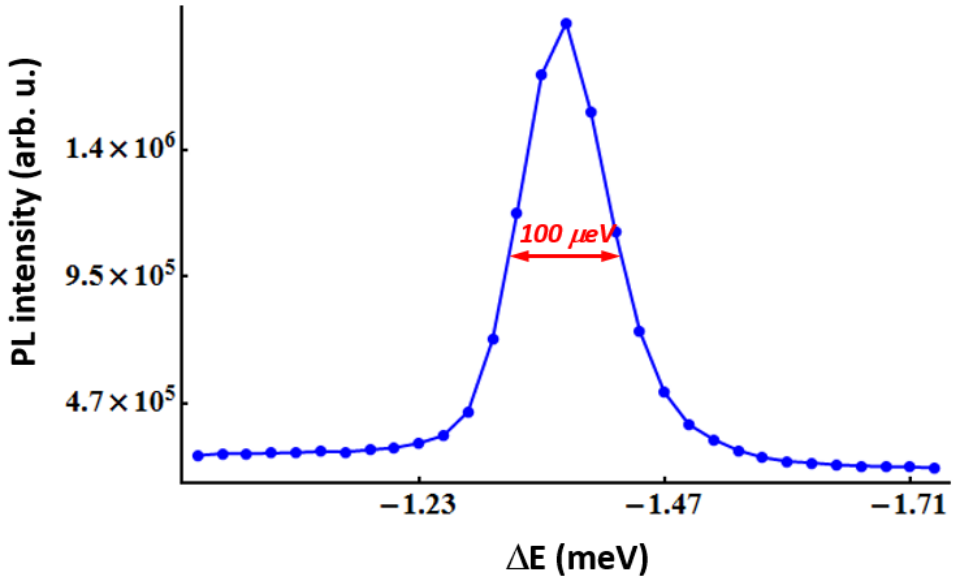

Figure 4.10: Energy-resolved PL intensity of the exciton-polariton condensate for $P_L = P_{th}$. The energy scale is relative to the exciting laser energy $E_{laser} = 1.5353\,eV$.

4.2.3 Energy-resolved PL at threshold ($P_L = P_{th}$)

In this Subsection it will be shown that the excited exciton-polariton condensate structure consists of two different MQSs and of an incoherent background. One of these MQSs is the 2D GS that is spatially surrounded by a second kind of MQS (cf. Fig. 4.11), which will be dubbed as *1D MQS* in the following discussion.
The tomograms in Fig. 4.11 show the spectrally resolved real- and k-space images of the exciton-polariton condensate structure (shown in the inset of Fig. 4.9) at different energies for an excitation power P_L close to the condensation threshold P_{th}, i.e. $P_L = P_{th}$. Figures 4.11(a)-(f) enable one to spectrally separate different condensation states. In the upper row, the 2D GS state is displayed, which is energetically higher than the 1D MQSs (second row). The energy difference amounts to several tens of μeV and is comparable to the spectral resolution of 60 μeV. However, thanks to their different symmetries in the k-space, it is possible to clearly separate the spectral features.
The important feature here is the symmetry of the 1D MQSs in the k-space. Here, the PL is emitted along M $\rightarrow$ X of the MBZ, mostly along the k_y-direction. Furthermore, the PL emission only occurs at the X-point along $\Gamma \rightarrow$ X. The reason for this lies in the curvature of the exciton-polariton dispersion in a square lattice, which was schematically illustrated in Fig. 2.10. At the M-points, the curvature of the dispersion is such that the effective mass of the particles is negative along all k-directions, whereas at the X-point the effective mass of exciton-polaritons is negative along $\Gamma \rightarrow$ X, but positive along M $\rightarrow$ X. Thus, the X-point is a hyperbolic point, where the exciton-polariton effective mass is anisotropic. In analogy to the explanation for the 2D GS formation, 1D MQSs form a spatially extended state in one direction, i.e. along $\Gamma \rightarrow$ X in the k-space, and are confined in the perpendicular direction, i.e. along M $\rightarrow$ X, because of the negative effective mass m^* of exciton-polaritons along the $\Gamma \rightarrow$ X-direction. The latter enables the self-localisation of the particles due to the compensation of the repulsive potential energy E_{pot} by the negative kinetic energy E_{kin} associated with m^*, and because of the confinement, respectively. According to the k-space images in Fig. 4.11(b) and the Heisenberg's Principle, 1D MQSs must be wire-liked shaped and perpendicularly orientated to each other. The majority of them appears to be orientated along the x-direction in real-space because of the higher PL intensity emitted along the k_y-direction in k-space.
Figures 4.11 (d) and (e) also show that the 2D GS and 1D MQSs are spatially separated from each other. The 2D GS only forms at the centre of the spot, where the gradient in intensity is spatially symmetric. The formation of the 1D MQSs may be related to the asymmetric spatial intensity gradient of the Gaussian beam in this spatial region. This provides an energy gradient that gives the polaritons momentum in the radial direction, probably preventing the formation of a stable 2D GS wavepacket at the M-points.

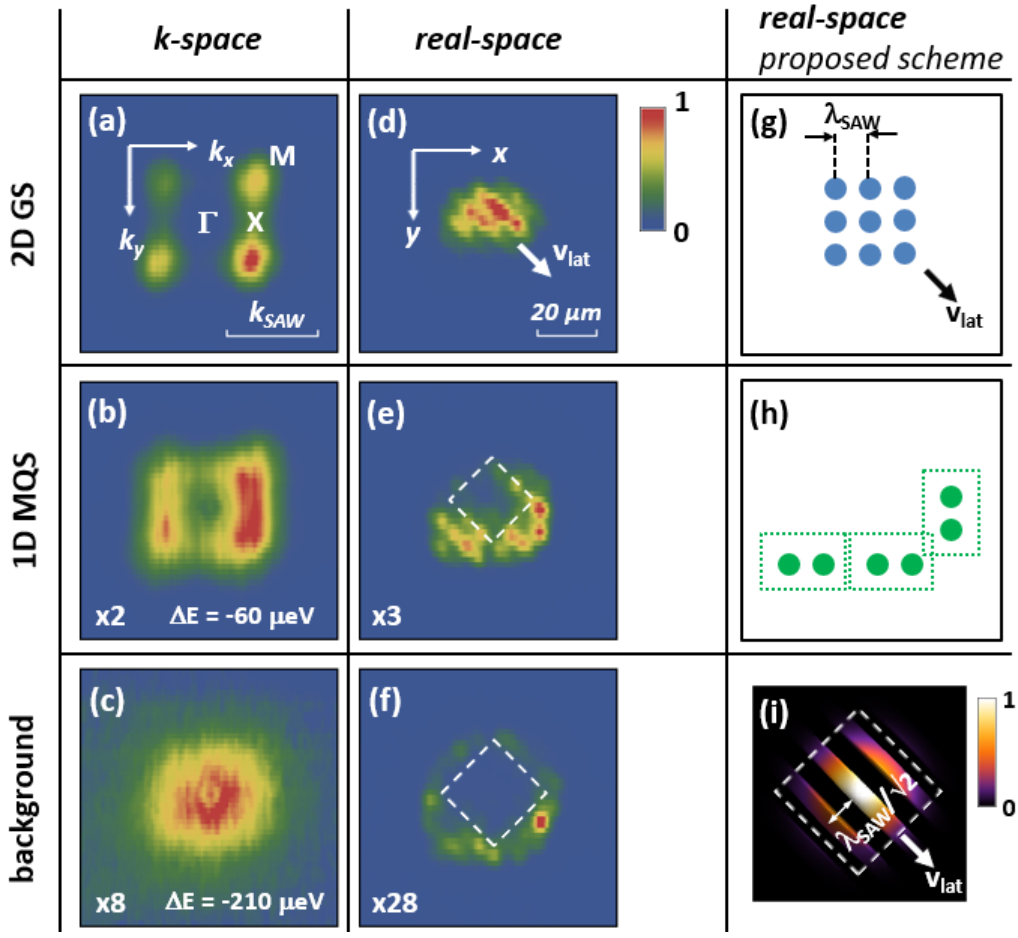

Figure 4.11: (a)-(f) Tomograms of the exciton-polariton condensate structure for $P_L = P_{th}$. The "xN" labels indicate the intensity magnification factor N with respect to the tomogram of the 2D GS in (a). "ΔE" labels show the energy shift of 1D MQSs and the incoherent background with respect to the 2D GS. $\mathbf{v}_{lat}$ indicates the direction of the lattice movement. The white dashed squares symbolise the shape of the wavefunctions of the 2D GS and 1D MQSs (see text). (g) and (h) show the assumed wavefunctions of 2D GS and three 1D MQSs, respectively, at a certain time instant. The dashed green rectangles represent the expected smeared PL areas of 1D MQSs in a time-integrated image. (i) displays the assumed 2D GS wavefunction with Gaussian intensity profile integrated over an acoustic period of the lattice.

Coherence length and spatial configuration of 2D GS and 1D MQSs

An 1D MQS has a coherence length $L^{1D\,MQS}_{coh,\,\mathrm{M}\rightarrow\mathrm{X}}$ of approximately one λ_{SAW}, i.e. $8\,\mu m$, in real-space, if determined from the k-space along M $\rightarrow$ X, and a coherence length $L^{1D\,MQS}_{coh,\,\Gamma\rightarrow\mathrm{X}}$ of approximately $2\,\lambda_{SAW}$, i.e. $16\,\mu m$, if calculated along $\Gamma \rightarrow$ X-direction in the MBZ. Both coherence lengths are smaller than the total spatial extension of the recorded 1D MQS structure, especially along the x-direction, as shown in the time-integrated real-space image (Fig. 4.11(e)). Thus, more than one 1D MQS were excited. A possible spatial configuration of 1D MQSs is proposed in the Fig. 4.11(h). A wavefunction of one 1D MQS should consist of 2 dot-like areas (green filled cicles) indicating the wavefunction maxima, which must be spatially displaced by λ_{SAW} from each other.

1D MQSs are spatially separated from 2D GS in real-space. 2D GS is at the centre of the condensate structure, while the wire-like shaped 1D MQSs surround it. 1D MQSs are spatially formed below and on one side of the 2D GS, which may be due to the wegde of the sample. In addition, the same real-space image in Fig. 4.11(e) unveils that the wavefunction of the 2D GS is square-like. The latter one was spectrally cut out from the total exciton-polariton condensate structure and its area is square-shaped (white dashed square in Fig. 4.11(e)). The 2D GS wavefunction is square-like with dimensions of $3\lambda_{SAW} \times 3\lambda_{SAW}$ as reported in Ref. [75] (cf. blue dot-like structure in Fig. 4.11(g)). Also, the real-space image of the incoherent background PL emission shows a square-shaped cutted out area in the total condensate structure (white dashed square in Fig. 4.11(f)). Thus, also the incoherent sum of the 2D GS and 1D MQSs wavefunctions must be square- or rectangular-like. The spatial dimensions of this superposition of the both wavefunctions are approximately $32\,\mu m \times 32\,\mu m$ corresponding to $4\,\lambda_{SAW} \times 4\,\lambda_{SAW}$. This supports the proposed schemes of the 2D GS and 1D MQS wavefunctions presented in Figs. 4.11(g) and (h), respectively. Note, the latter ones appear to be rotated by 45° in the experimentally recorded real-space images with respect to their schemes in Figs. 4.11(g) and (h). This is not a discrepancy but more an deception of the mind. If the motion of the proposed 2D GS wavefunction is integrated in time over a whole acoustic period of the lattice and one considers that the 2D GS wavefunction must have a Gaussian intensity profile, one will obtain a result, which seems to be the rotated 2D GS wavefunction as displayed in Fig. 4.11(i) - like the experimentally recorded real-space images.

At the spatial periphery of the 1D MQSs (cf. Fig. 4.11(f)) one observes a low incoherent PL emission, which is associated with the Γ-point of the MBZ (Fig.4.11(c)). The central energy of the background emission approximately is $210\,\mu eV$ lower than the 2D GS energy.
The peak intensity of emission from the 2D GS is 3-times and 8-times higher than the ones from the 1D MQS and the Γ-point, respectively.

Composition of the PL of the condensate structure

Another notable fact regards the total PL intensity emitted by the 2D GS and 1D MQSs, which is the highest for the 2D GS. The latter is related to the Gaussian intensity profile of the used laser spot. Figure 4.12 shows the composition of the energy-resolved total emitted PL of the exciton-polariton condensate structure. Note, the energy scale in the Fig. 4.12 relates to the exciting laser energy $E_{laser} = 1.5353\,eV$. The emission attributed to the 2D GS (green curve) clearly dominates over 1D MQSs (black curve) and the incoherent background (orange curve) appears almost negligible. These curves have been obtained by fitting Gaussian intensity profiles at the energies of the corresponding states. The integrated intensity of the 2D GS (green curve) is two-times larger than the one of the 1D MQSs. Note that both PL curves energetically overlap and possess similar values for the linewidth of approximately $70\,\mu eV$, which is comparable to the spectral resolution in the experiment. In contrast to the PL emitted from the Γ-point (orange curve), the narrow linewidth of 2D GS and 1D MQSs, in addition to the long estimated coherence lengths, implies that they are condensates. The linewidth of the PL at the Γ-point is 3 times larger and thus, it was previously associated with the incoherent background (orange curve). The 3-Gaussian fit (red dashed curve) reproduces well the recorded total line shape (blue curve).

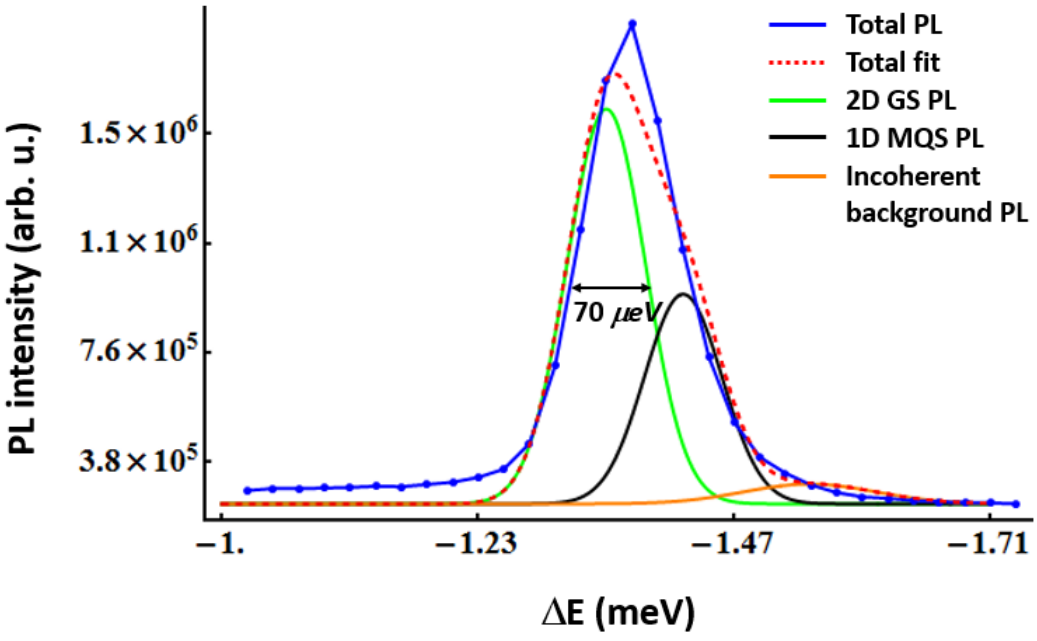

Figure 4.12: Composition of the emitted PL intensity at $P_L = P_{th}$. The energy scale is relative to the exciting laser energy $E_{laser} = 1.5353\,eV$.

4.2.4 Energy-resolved results for $P_L > P_{th}$

All results presented so far were obtained using a laser power P_L close to the condensation threshold P_{th}. In the following, the dependence of the properties of the 2D GS and 1D MQSs on higher P_L is discussed, which is as well summarised in the Figs. 4.13-4.20.

First, the total emitted PL by the condensate structure in dependence on the P_L is spectrally resolved (cf. Fig. 4.13). As expected, one observes an increase of the PL intensity as well as of the blue-shift ΔE^{PL}_{blue}. ΔE^{PL}_{blue} amounts to approximately $400\,\mu eV$ between the energies of the excited condensate structure at $P_L = P_{th}$ and $P_L = 40\,P_{th}$. The origin of the blue-shift ΔE^{PL}_{blue} lies in the repulsive polariton-polariton interactions. When the laser power P_L is increased, more exciton-polaritons are injected and thus, the inter-particle energy is increased due to their repulsive interactions. Furthermore, the total PL linewidth increases with P_L (cf. inset of Fig. 4.13). This is a surprising and an interesting finding at the first glance. Since the total emitted PL by the condensate structure consists of different kinds of MQSs, i.e. 2D GS and 1D MQSs, that are accompanied by an incoherent background, their linewidths or the one of the incoherent background must increase or their central energies must shift relative to each other.

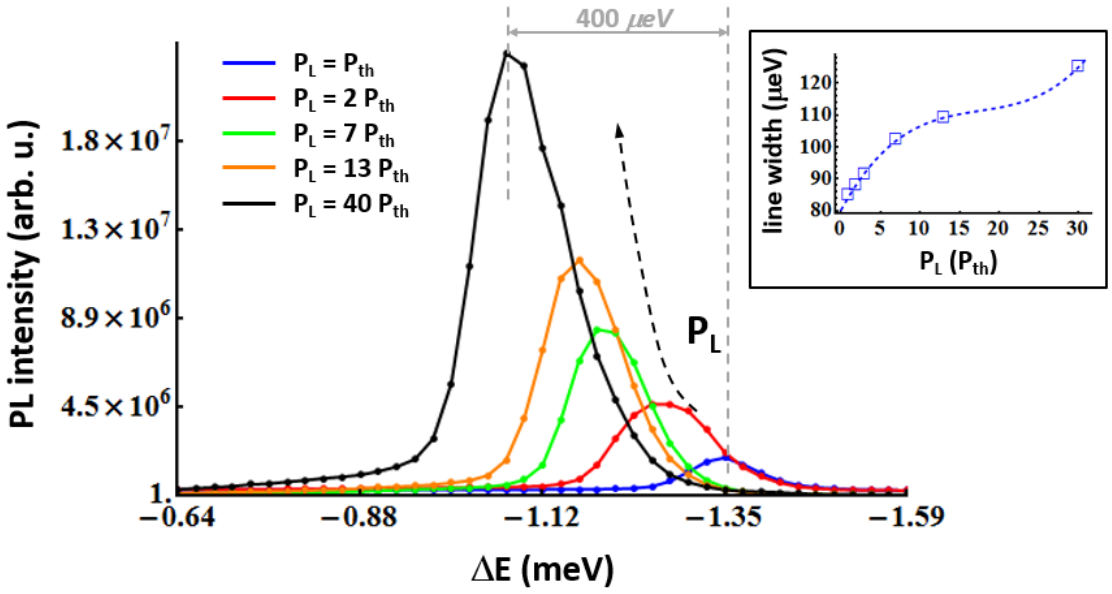

Figure 4.13: Energy-resolved PL intensity of the exciton-polariton condensate structure for different excitation powers P_L. The inset shows the linewidth of the corresponding PL profiles. The blue dashed line is a guide for the eye.

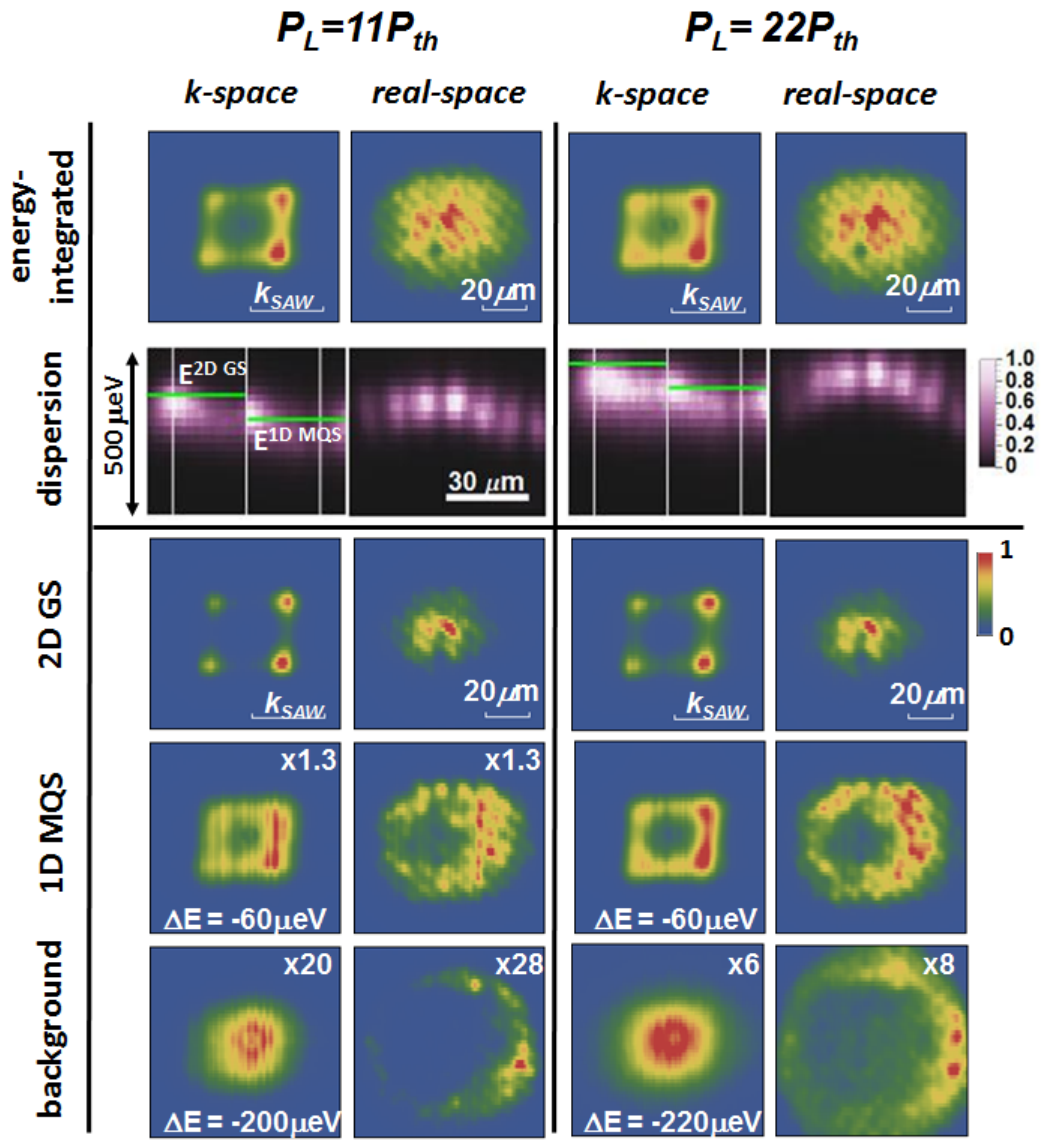

Figure 4.14: Tomograms of the exciton-polariton condensate structure for $P_L > P_{th}$ (adopted from [81]). The SAW potential was set to 200 μeV as been estimated from the energy gap between the exciton-polariton states at Γ- and M-points at lower excitation powers P_L, i. e. $P_L < P_{th}$. The green lines in the k-space dispersion spectra show the values, where the tomograms for 2D GS and 1D MQS were taken. The real space spectra were taken along the centre of the condensate structure. The "xN" labels indicate the intensity magnification factor N with respect to the tomogram of the 2D GS. The "ΔE" labels show the energy separation of 1D MQS and the incoherent background with respect to 2D GS.

Figure 4.14 shows the recorded spectrally resolved PL images of the k- and real-space of the condensate structure for different laser powers P_L. The first row shows energy- and time-integrated real- and k-space images of the exciton-polariton condensate structure. The second row displays cuts of the exciton-polariton dispersion along the $\Gamma \rightarrow$ M-direction. The green lines mark the energies $E^{2D\,GS}$ and $E^{1D\,MQS}$ of the 2D GS and 1D MQS, respectively.
The tomograms (3rd, 4th and 5th row in the Fig. 4.14) show, as in the case of low excitation laser power, that the exciton-polariton condensate structure consists of the 2D GS and 1D MQSs, which are spatially surrounded by an incoherent background. The experimental measurements show that it is possible to distinguish the 2D GS and 1D MQSs for all excitation levels. In contrast to the previous case (cf. Subsec. 4.2.3), the 2D GS at the centre of the excitation spot has now expanded to a diameter of $31\,\mu m$. This spatial extension corresponds closely to $L_{coh}^{2D\,GS}$ if calculated from the corresponding k-space image, thus indicating the presence of a single 2D GS. The 2D GS is still surrounded by a ring-shaped region with lower energy of emission. The related k-space map shows that it consists of 1D MQSs, which must be perpendicularly orientated to each other. The coherence length of a 1D MQS is still on the order of $1\,\lambda_{SAW} \times 2\,\lambda_{SAW}$. Since these dimensions are smaller than the observed dimensions of the ring emission area, several 1D MQSs oriented along the x- and y-direction coexist in this region.
At the higher P_L-value (cf. Fig. 4.14, second column), the size of the 2D GS state at the centre of the laser spot remains essentially unchanged. The k-space map of 1D MQSs shows, however, that the emission from M$\rightarrow$X increases significantly. In addition, from the corresponding real-space image one observes that it now completely surrounds the central 2D GS state.
Finally, the spectrum in the second row shows that the dispersions are blue-shifted. The spectral blue-shift increases with P_L and is again attributed to the polariton-polariton repulsive interactions, which renormalise the lattice dispersion. The blue-shift changes with position in the real-space due to the Gaussian intensity profile of laser spot.

2D GS and 1D MQSs PL dependence on laser power

Several P_L-regimes (marked by I-III in Fig. 4.15) can be identified in the dependence of the 2D GS on excitation power. At low P_L, i.e. $P_L \leq 200\,mW$ (I-regime), the total 2D GS PL intensity $I_{PL}^{2D\,GS}$ (green curve in Fig. 4.15) steeply increases, while at higher P_L the slope of the PL increase significantly reduces. At $P_L < 400\,mW$, $I_{PL}^{2D\,GS}$ is higher than the total PL intensity of 1D MQSs and the incoherent background. In contrast, the total PL intensity $I_{PL}^{1D\,MQS}$ emitted by 1D MQSs (black curve) linearly increases with P_L becoming brighter than $I_{PL}^{2D\,GS}$ at $P_L \geq 400\,mW$ (II-regime). According to the latter, the condensate structure must then contain more exciton-polaritons in 1D MQSs than in the 2D GS, which contrasts to behaviour at low excitation powers. In the range $P_{th} \leq P_L \leq 200\,mW$, the increase of $I_{PL}^{2D\,GS}$ is stronger than at higher P_L, which indicates a reduction of the efficiency of the exciton-polariton injection at high P_L into the 2D GS state. Moreover, at $P_L \geq$

$400\,mW$ the total PL intensity I_{PL}^{back} of the incoherent background (orange curve) obviously increases from an almost constant low value at lower P_L and overcomes $I_{PL}^{2D\,GS}$ at $P_L \geq 800\,mW$ (III-regime).
One reason for the drop of the injection efficiency of the exciton-polaritons into the 2D GS at high P_L is the strong blue-shift of the exciton-polariton dispersion, which affects the OPO resonance conditions.

Figure 4.16 shows a 3-peak fit of the total PL at $P_L = 390\,mW$, i.e. $P_L = 11\,P_{th}$. At this excitation power, the total 2D GS PL intensity $I_{PL}^{2D\,GS}$ (green curve) is of the same order of magnitude as the total PL intensity $I_{PL}^{1D\,MQS}$ emitted by 1D MQSs (black curve). The main differences between them regards their central peak energies. As previously discussed, the energy $E^{2D\,GS}$ of the 2D GS lies above the energy $E^{1D\,MQS}$ of the 1D MQSs. The linewidths of the 2D GS and 1D MQSs, however, remain unchanged within the spectral resolution (cf. Fig. 4.18).

If the laser power P_L is further increased to $800\,mW$, i.e. $P_L = 22\,P_{th}$, the fitted 2D GS and 1D MQS profiles are hard to be separated from each other and $I_{PL}^{2D\,GS}$ becomes comparable with the background PL intensity I_{PL}^{back} (orange curve in Fig. 4.17, III-regime). According to the fits, the overlap between the 2D GS and 1D MQS profiles increases with P_L.

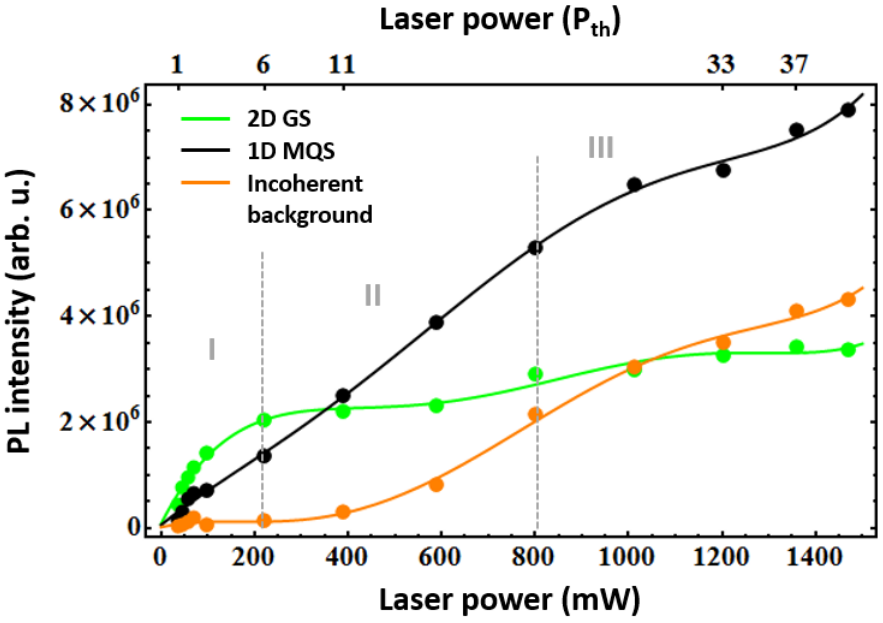

Figure 4.15: Dependence of the PL intensity of the 2D GS, 1D MQSs and the incoherent background on the excitation power P_L

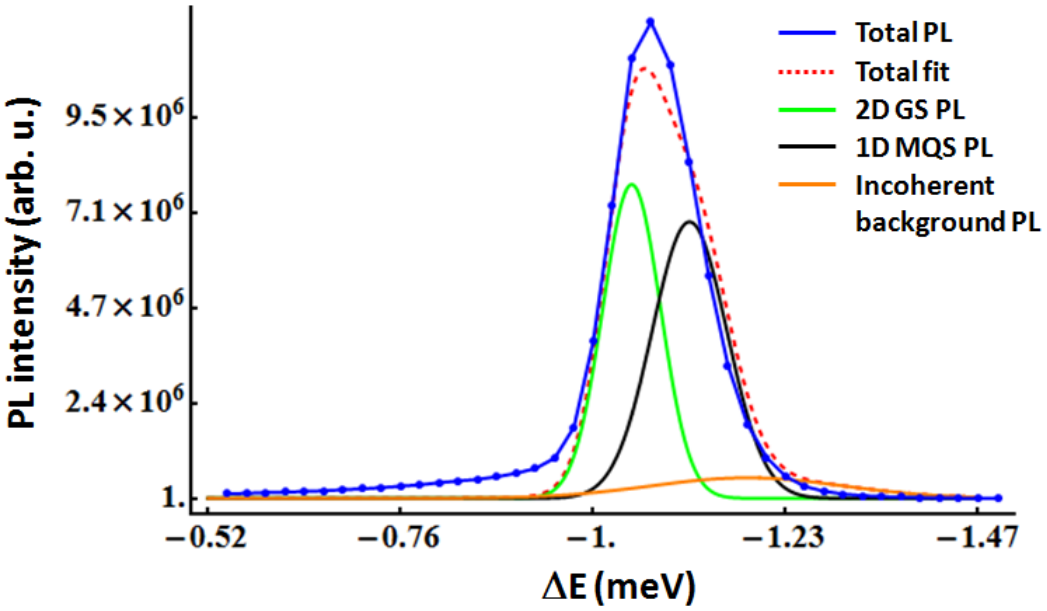

Figure 4.16: Composition of the emitted PL intensity at $P_L = 11\,P_{th}$. The energy scale relates to the exciting laser energy $E_{laser} = 1.5353\,eV$.

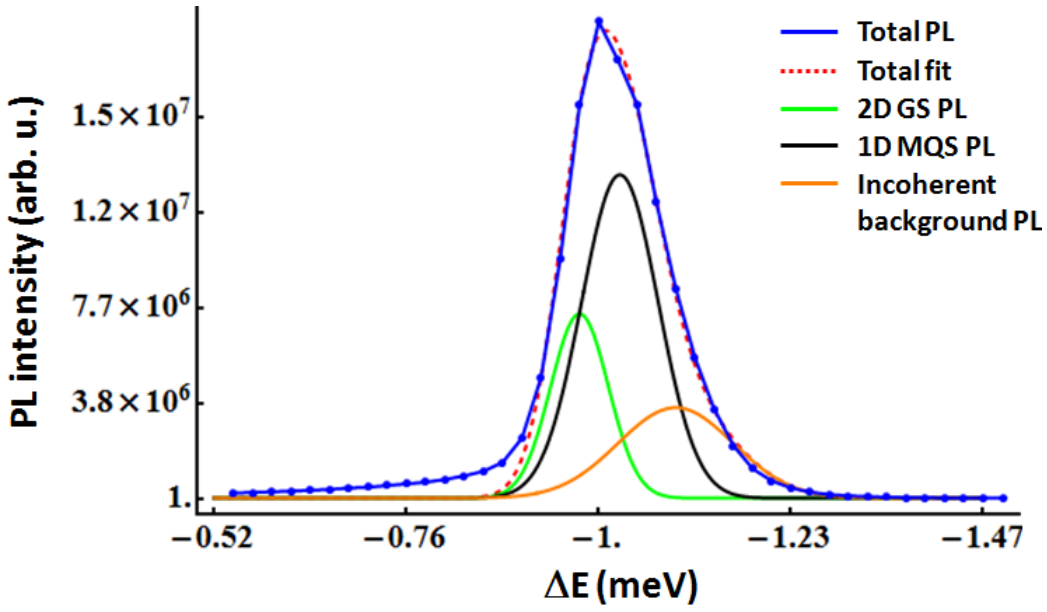

Figure 4.17: Composition of the emitted PL intensity at $P_L = 22\,P_{th}$. The energy scale relates to the exciting laser energy $E_{laser} = 1.5353\,eV$.

2D GS and 1D MQSs linewidth and energy dependence on laser power

Figure 4.18 displays the dependence of the linewidth of the 2D GS (green curve), 1D MQS (black curve) and the incoherent background (orange curve) as a function of the laser power P_L. The error bars indicate the spectral resolution of the experimental set-up. The linewidths of the 2D GS and 1D MQSs are - within the spectral resolution - identical and amount to approximately $60\,\mu eV$. However, there might be a noticeable trend. While the 2D GS linewidth is independent on the laser power P_L, the linewidth of 1D MQSs seems to increase at $P_L > 220\,mW$. At these laser powers, the PL intensity $I_{PL}^{1D\,MQS}$ from 1D MQS states dominates the total condensate PL. As discussed before, at high P_L additional 1D MQSs are formed. Since these 1D MQSs surround the 2D GS, they are spatially located at different positions within the excitation spot, which determine the 1D MQS energy states due to the wedge of the sample, i.e. spatial sample thickness variation, as discussed in Sec. 4.1. Accordingly, 1D MQSs will differ in energy by roughly $25\,\mu eV$, which should lead to a broadening of their linewidth.
Figure 4.18 also reveals that the linewidth of the incoherent background non-linearly increases with P_L from $120\,\mu eV$ at $P_L = P_{th}$ to $170\,\mu eV$ at $P_L = 3\,P_{th}$ and to $250\,\mu eV$ at $P_L = 38\,P_{th}$ (cf. Fig. 4.18). As pointed out previously by the Fig. 4.4, the increase of the linewidth must be due to the strong blue-shift of the exciton-polariton dispersion at higher P_L, which results in the accumulation of a higher number of exciton-polaritons at the Γ-point of the MBZ and, correspondingly, in higher incoherent background intensity I_{PL}^{back}, which is observed in the experiment. This is seen as the origin for the increase of the linewidth of the total PL emitted by the condensate structure presented in the inset of Fig. 4.13.

Figure 4.19 summarises the energy dependence of the condensated states and the incoherent background on the laser power P_L. In order to obtain their energies, the central peak energy of each of the three states, i.e. the 2D GS, 1D MQSs and incoherent background, was first determined for each P_L. The energy curves $E^{2D\,GS}$ and $E^{1D\,MQS}$ of the 2D GS (green points) and 1D MQSs (black points), respectively, follow the same trend characterised by a linear dependence in a semi-log plot. The solid curves are logarithmic fits of the experimental data. In total, their energies increase by approximately $400\,\mu eV$ from the value at $P_L = P_{th}$ and $P_L = 1400\,mW$, i.e. $P_L = 38\,P_{th}$. The energy separation between $E^{2D\,GS}$ and $E^{1D\,MQS}$ is always at the range of $50-70\,\mu eV$. The central energy peak E^{back} of the incoherent background (orange curve), however, is energetically on the order of $200\,\mu eV$ lower than $E^{2D\,GS}$. Its trend follows the trend of the 2D GS, but with a smaller slope.

It is to note that after a strong jump in the blue-shift $\Delta E_{blue}^{2D\,GS}$ of the 2D GS at $P_L \leq 220\,mW$ (cf. Fig. 4.19 with a logarithmic scale), $\Delta E_{blue}^{2D\,GS}$ only moderately increases with higher P_L and an additional look at Fig. 4.15 may unveil that the blue-shift is related to the reduction of the increase of the PL intensity $I_{PL}^{2D\,GS}$ at $P_L > 220\,mW$ and thus, to the injection efficiency of exciton-polaritons into the 2D GS state.

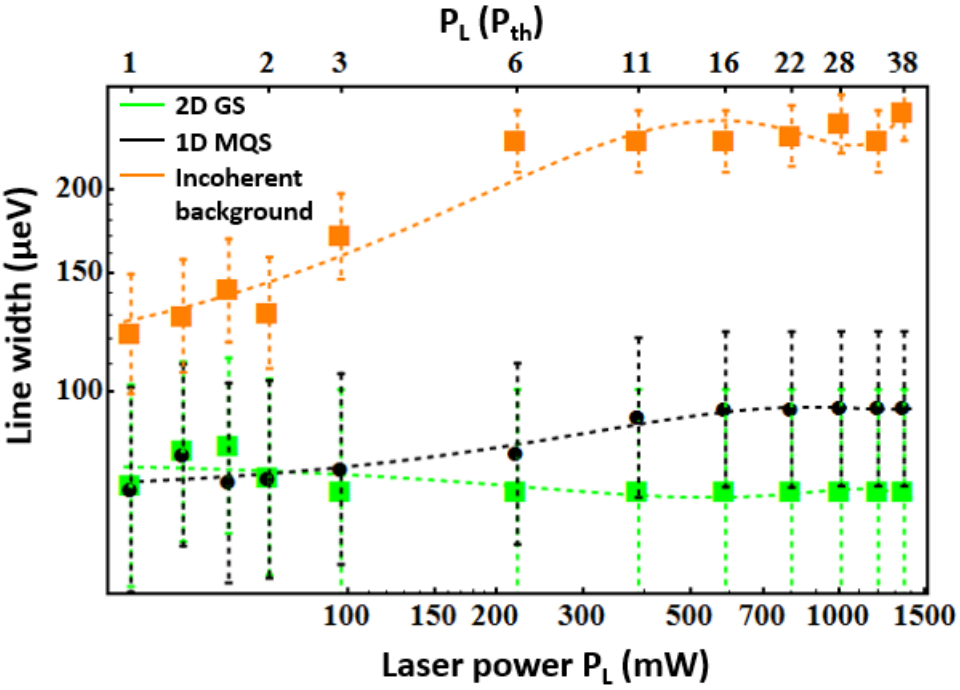

Figure 4.18: Dependence of the linewidth of the 2D GS and 1D MQS states and the incoherent background on the laser power P_L. The lines are a guide for the eye.

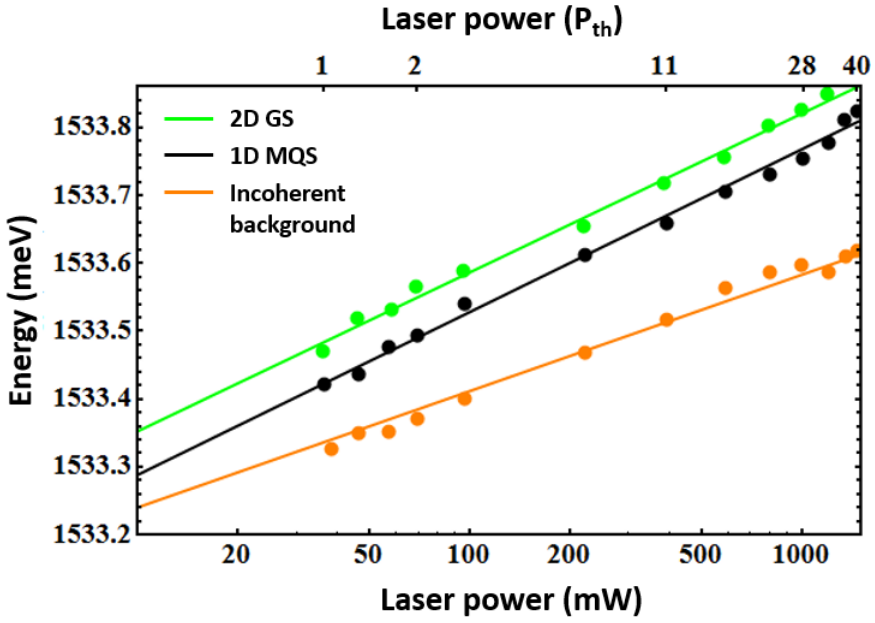

Figure 4.19: Dependence of the blue-shift of the 2D GS, 1D MQS and the incoherent background on the laser power. The lines are a guide for the eye.

2D GS and 1D MQS coherence length dependence on laser power

The final question concerns the coherence length properties of the 2D GS and 1D MQS. The latter two are displayed in Fig. 4.20 and compared to the total size, i.e. diameter determined along the y-direction obtained from the real-space images. In addition, Fig. 4.20 compares the size of the 2D GS wavepacket (orange squares), which was directly measured in the real-space images, and the coherence length of the 2D GS calculated from the k-space (green curve). There is a good agreement between them. Thus, the size and the coherence length of 2D GS can be used as synonyms in this case.
The coherence length $L_{coh}^{2D\,GS}$ of the 2D GS (green curve) amounts to $(20 \pm 3)\,\mu m$ at $P_L = P_{th}$ and slowly increases to its maximum value of $(31 \pm 1)\,\mu m$ at $P_L = 390\,mW$, i.e. $P_L = 11\,P_{th}$. At higher P_L, $L_{coh}^{2D\,GS}$ decreases and keeps its value of $(28 \pm 2)\,\mu m$ constant. The coherence length $L_{coh}^{1D\,MQS}$ of 1D MQS (black curve) shows a similar trend. Also here, three main P_L-regimes can be identified. At $P_{th} \leq P_L \leq 100\,mW$, within the given accuracy, $L_{coh}^{1D\,MQS}$ increases from $(16 \pm 1)\,\mu m$ at $P_L = P_{th}$ to $(22 \pm 2)\,\mu m$ at $P_L = 100\,mW$, i.e. $P_L = 3\,P_{th}$. In the range of $100 < P_L \leq 390\,mW$, it remains constant at the latter value and at $P_L > 390\,mW$ the coherence length of 1D MQS reduces to $(16 \pm 1)\,\mu m$.
Note that the here discussed coherence length $L_{coh}^{1D\,MQS}$ of 1D MQS only takes into account the coherence length, which was calculated from the k-space along the X $\rightarrow$ Γ-direction in the MBZ, i.e. $L_{coh,\,1D\,MQS}^{X\rightarrow\Gamma}$. The coherence length along the perpendicular direction, i.e. $L_{coh,\,1D\,MQS}^{M\rightarrow X}$, was not mentioned, since $L_{coh,\,1D\,MQS}^{M\rightarrow X}$ is constant at the value of λ_{SAW} as previously discussed.

Furthermore, the size of the total condensated area (red curve), which is defined as the composition of the 2D GS and 1D MQSs, grows with increasing laser power P_L. The tomographic images showed that there is only one single 2D GS. Since the total condensated area is significantly larger for all P_L, it is again an indication that several 1D MQSs were additionally excited. Especially, from the difference between the condensated area (red curve) and the 2D GS size (green curve) it is possible to estimate the number of the excited 1D MQS states along the y-direction. For example, at $P_L = 28\,P_{th}$, the difference between the condensated area (diameter is $72\,\mu m$) and the 2D GS size ($28\,\mu m$) amounts to $44\,\mu m$. Thus, in the y-direction there are $\frac{44\,\mu m}{L_{coh,\,1D\,MQS}^{M\rightarrow X}} \approx 5 - 6$ 1D MQS states. Assuming a totally symmetric condensate structure, there must be five to six 1D MQSs in the x-direction, too. Thus, the total condensate structure consists of a single 2D GS and ten to twelve 1D MQSs at $P_L = 28\,P_{th}$.

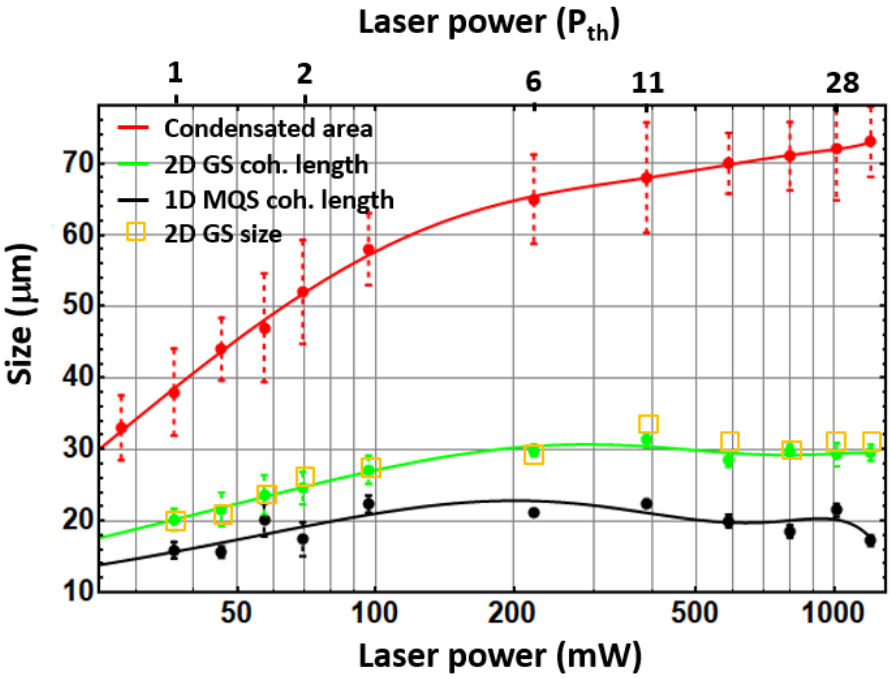

Figure 4.20: Dependence of the coherence length of 2D GS (green curve) and 1D MQS (black curve) on the laser power is compared to the diameter of the total condensated area (red curve). The orange squares represent the 2D GS size directly measured in the real-space images. The lines are a guide for the eye.

It is interesting to notice that the shrinking of the 2D GS at $P_L > 220\,mW$ occurs when the total PL intensity of 1D MQSs overcomes the one from the 2D GS (cf. Fig. 4.15). A possible origin of the decrease of $L_{coh}^{2D\,GS}$, but as well of $L_{coh}^{1D\,MQS}$, is the excitation of additional 1D MQSs at the spatial periphery of the 2D GS. Another ones are the blue-shift $\Delta E_{blue}^{2D\,GS}$ and the limited 2D GS size as it will be discussed later. The first is supported by a model, which quantifies the dependence of $\Delta E_{blue}^{2D\,GS}$ on P_L. Usually, $\Delta E_{blue}^{2D\,GS}$ is defined relative to the energy of the Γ-point at the condensation threshold. The model is based on Eq. 2.5.4, that describes the potential energy of N injected exciton-polaritons within a location area of the radius r_{XP}, i.e.

$$\Delta E_{blue}^{2D\,GS} \propto \frac{N\,g}{(\pi r_{XP})^2}. \tag{4.2.1}$$

$\Delta E_{blue}^{2D\,GS}$ was quantified by fitting N to the experimental data. N represents the total number of excited exciton-polaritons injected into all states, i.e. the 2D GS, 1D MQS and incoherent background. r_{XP} represents the 2D GS radius and was directly taken from the experimental results, i.e. $r_{XP} = L_{coh}^{2D\,GS}/2$. g is exciton-polariton interaction constant, $g = 10\,\mu eV\,\mu m^2$ [75]. The parameters N and r_{XP} are functions of the laser power P_L.

The results of the model are presented in Fig. 4.21. One may think that a larger N increases the potential energy due to the polariton-polariton interactions, screening the SAW potential Φ_{SAW} and thus, reducing the effective lattice bandgap energy ΔE_G^{XP}. This results in a smaller effective mass $|m^*|$ implying a weaker localisation force counteracting the repulsive forces induced by the polariton-polariton repulsive interactions. As a result, the wavepacket expands. Indeed, estimating the blue-shift $\Delta E_{blue}^{2D\,GS}$ one sees that this simple picture reproduces well the behaviour of the system for values up to $P_L = 100\,mW$ (blue line in Fig. 4.21), close to the point, where the 2D GS reaches its maximum size. For higher pump values it strongly overestimates the blue-shift, which indicates that the system enters more and more a different regime of dynamics, where the filling of the donut-shaped area of the 1D MQSs becomes more dominant. In other words, at low P_L the majority of excited exciton-polaritons are injected into the 2D GS state. This situation reverse for higher P_L, which is in agreement with the previous discussions.

Remarks

Furthermore, using the fitted value for N in $\Delta E_{blue}^{2D\,GS}$ enables one to estimate the excited exciton density $n_X^{2D\,GS}$ of the 2D GS within a single GaAs QW of the sample and to compare it to the saturation density $n_X^{sat} \approx 5 \times 10^{10}\,cm^{-2}$, above which the excitons cannot be considered as bosons [61],

$$n_X^{2D\,GS} = \frac{1}{N_{QW}} \frac{N}{(\pi r_{XP})^2}. \tag{4.2.2}$$

Here, N_{QW} is the number of GaAs QWs of the MC structure. The results are displayed in the Fig. 4.22. The excited exciton density remains for all used optical excitation powers significantly below the saturation density n_X^{sat} and correspondingly, the excited excitons kept their bosonic nature.

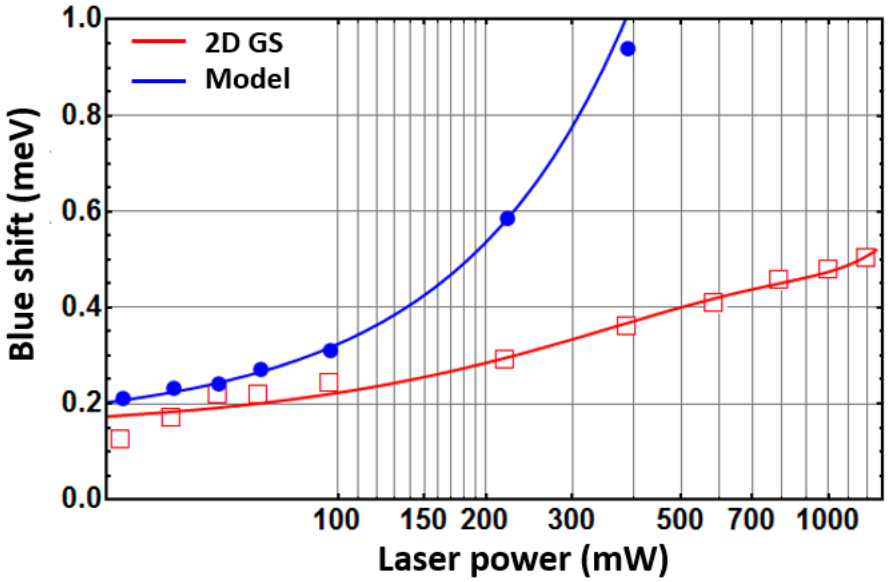

Figure 4.21: Dependence of the blue-shift $\Delta E_{blue}^{2D\,GS}$ as directly measured from the experiment (red curve) and estimated from the expression for the potential energy $E_{pot}^{2D\,GS}$ (blue curve). Both lines are a guide for the eye.

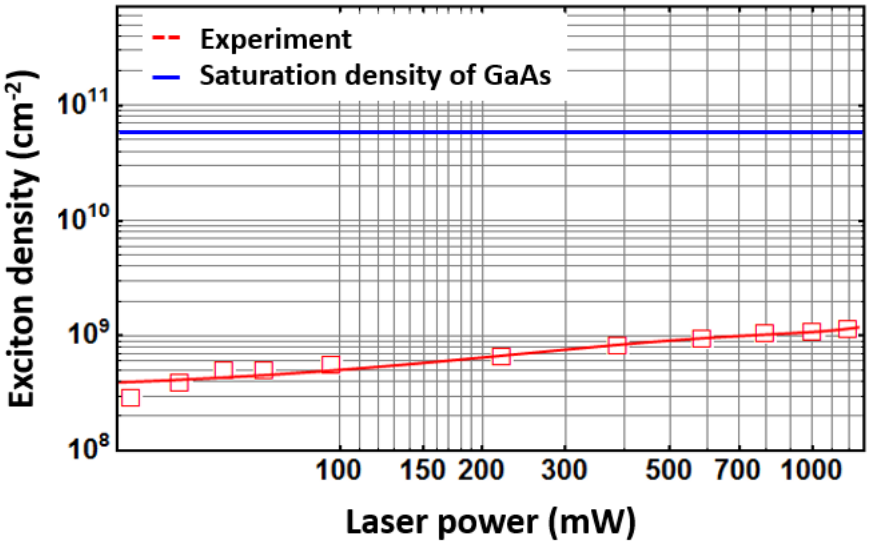

Figure 4.22: Estimated dependence of the exciton density on the laser power (red curve). The saturation density is marked by the blue line.

Dependence on the SAW power P_{RF}

The qualitative dependence of the properties of 2D GS and 1D MQSs on the SAW power P_{RF} can be theoretically deduced by considering the confinement effects introduced by SAWs. When SAWs are applied, the potential landscape for the exciton-polaritons becomes modulated. The spatial dimensions and the potential amplitude are directly proportional to the SAW wavelength λ_{SAW} and the SAW potential Φ_{SAW}, respectively. In the experiment, λ_{SAW} is a fixed parameter of $8\,\mu m$, whereas Φ_{SAW} is set by the SAW power P_{RF}. As discussed in Chapter 2, one has: $\Phi_{SAW} \propto \sqrt{P_{RF}}$. An increase of Φ_{SAW} increases the confinement potential of exciton-polaritons resulting in a reduction of the condensation threshold P_{th} [75]. This is due to the fact that a smaller number of particles has to be injected to overcome the critical particle density n_{CR} required for exciton-polariton condensation. Following this argumentation, the interaction energy of the 2D GS and/or 1D MQSs must reduce with increasing SAW power P_{RF} as well. This behaviour can be understood by looking at the following equation, which describes the necessary condition for the 2D GS formation:

$$\partial(E_{kin}^{2D\,GS} + E_{pot}^{2D\,GS}) = 0 \tag{4.2.3}$$

where $E_{kin}^{2D\,GS}$ and $E_{pot}^{2D\,GS}$ are the kinetic energy and potential energy of the 2D GS, respectively. Note that the above equation can be also applied to describe the 1D MQS formation. Eq. 4.2.3 states that the 2D GS forms, when the 2D GS energy is a (local) energy minimum. Moreover, a decrease of $E_{kin}^{2D\,GS}$ results in a decrease of $E_{pot}^{2D\,GS}$. The first is reciprocally proportional to the effective mass of exciton-polaritons $|m^*|$, i.e. $E_{kin}^{2D\,GS} \propto 1/|m^*|$ [75]. An increase of P_{RF} results in an increase of $|m^*|$ and thus, in the reduction of $E_{kin}^{2D\,GS}$ and, consequently, of $E_{pot}^{2D\,GS}$.

Also, the coherence lengths $L_{coh}^{2D\,GS}$ and $L_{coh,\,\Gamma\rightarrow X}^{1D\,MQS}$ of 2D GS and 1D MQSs, respectively, are dependent on the SAW power P_{RF}. In general, it can be stated that the smaller P_{RF}, i.e. the confinement potential, the bigger is $L_{coh}^{2D\,GS}$ and/or $L_{coh,\,\Gamma\rightarrow X}^{1D\,MQS}$ (cf. Fig. 4.23 and 4.24). Figure 4.23 shows that the coherence length $L_{coh}^{2D\,GS}$ of 2D GS increases first at low laser powers P_L, reaches its maximum and then drops in the high P_L-range. This dependence is not influenced by the SAW power P_{RF}. However, the maximal 2D GS coherence length $L_{coh,\,max}^{2D\,GS}$ is found at lower laser power P_L, when the SAW power P_{RF} is decreased. If P_{RF} is decreased from $25\,mW$ to $12.5\,mW$, $L_{coh,\,max}^{2D\,GS}$ is at $P_L = 220\,mW$, in contrast to $P_L = 390\,mW$. If P_{RF} is doubled, i.e. $P_{RF} = 50\,mW$, $L_{coh,\,max}^{2D\,GS}$ shifts to $P_L = 590\,mW$. In other words, the estimated $L_{coh}^{2D\,GS}$-curves shift due to change of the effective mass $|m^*|$ of exciton-polaritons, which is set by P_{RF}. A change of $|m^*|$ results in a change of the coherence length $L_{coh}^{2D\,GS}$, i.e. r_{XP}, if the supplied laser power, i.e. N_{XP}, is fixed.

A similar trend is observed for the dependence of the coherence length $L_{coh,\,\Gamma\rightarrow X}^{1D\,MQS}$ of 1D MQSs on the laser power P_L and the SAW power P_{RF} (cf. Fig. 4.24). The fluctuations of $L_{coh,\,\Gamma\rightarrow X}^{1D\,MQS}$ at low excitation powers, i.e. $P_L \leq 100\,mW$, are attributed to numerical inaccuracies.

The decrease of $L_{coh}^{1D\,MQS}$ and/or $L_{coh}^{2D\,GS}$ at high P_L is attributed to the excitation of additional MQSs at their peripheries and their blue-shift.

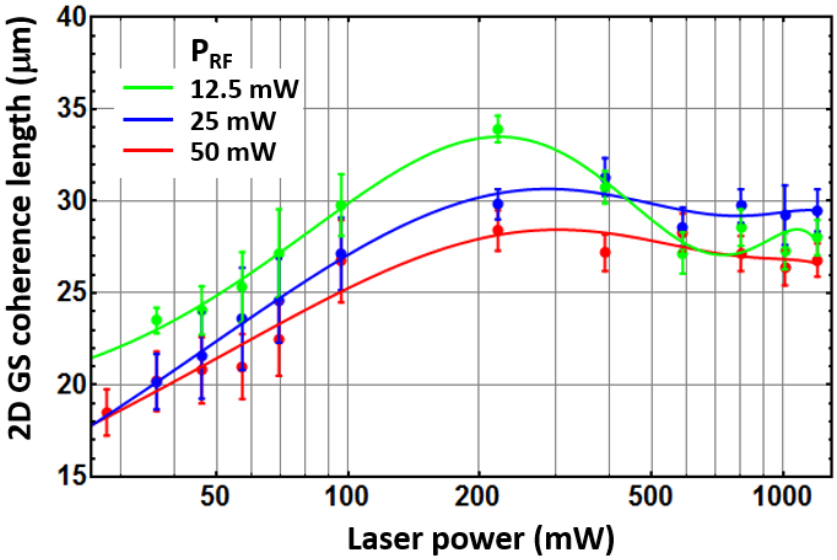

Figure 4.23: Dependence of the coherence length of 2D GS on the laser power P_L and the SAW power P_{RF}. The solid lines are a guide for the eye.

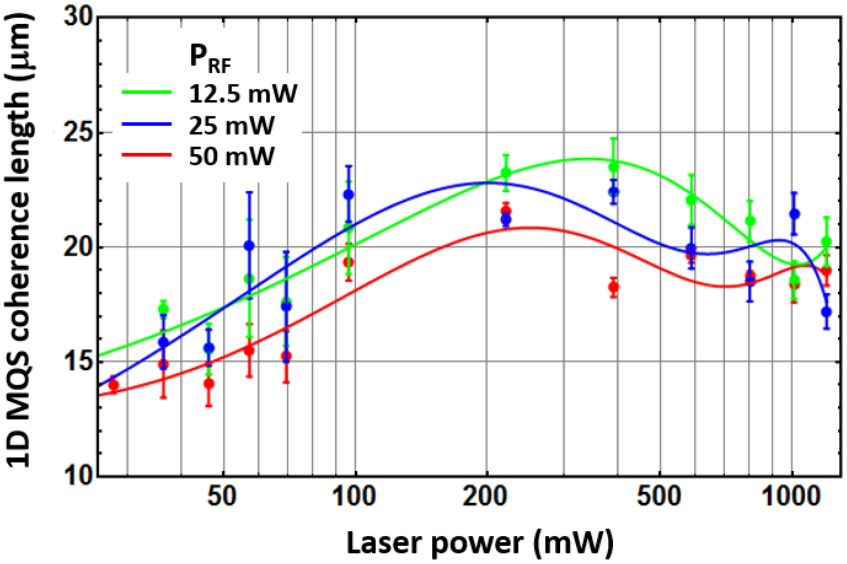

Figure 4.24: Dependence of the coherence length of 1D MQS on the laser power P_L and the SAW power P_{RF}. The solid lines are a guide for the eye.

Dependence on the size of the existing laser spot

As discussed previously, the coherence length $L_{coh}^{2D\,GS}$ of the 2D GS wave packet increases from $23\,\mu m$ at the threshold power P_{th}, or equivalently at the threshold power density ρ_{th} of $28\,\frac{\mu W}{\mu m^2}$, to $31\,\mu m$ at $50\,\frac{\mu W}{\mu m^2}$ (red curve in Fig. 4.25). Interestingly, above this value, the 2D GS stops expanding. The saturation is attributed to the fact that for these excitation levels, the area, where the optical power density is above the threshold, becomes larger than the 2D GS intrinsic size. Under these conditions, the latter becomes mainly determined by the effective mass of the 2D GS and the polariton-polariton interaction energy and is less sensitive to the particle density. In order to support this interpretation, also $L_{coh,\,120\mu m}^{2D\,GS}$ of the 2D GS excited with a larger laser spot with $\phi_L = 120\,\mu m$ was determined (cf. Fig. 4.25).
When the size ϕ_L of the laser spot is increased, its intensity profile becomes flatter. In order to stay in the condensation regime, the laser power P_L needs to be increased in the experiment to maintain the required power density for the formation of the 2D GS. In other words, the total illuminated area, where $P_L \geq P_{th}$, is larger for laser spots with bigger ϕ_L. Whereas, the injected particle density is unaffected by ϕ_L.

$L_{coh,\,120\mu m}^{2D\,GS}$ (blue curve in Fig. 4.25) is close to the one measured with the small laser spot ($\phi_L = 70\,\mu m$, red curve) for large P_L. This indicates that the 2D GS is at its full size for all power densities. Also, within the given accuracy, the coherence length $L_{coh,\,120\mu m}^{2D\,GS}$ remains constant, showing no dependence on the laser power P_L. More importantly, these experimental results discard the less efficient exciton-polariton injection at high optical excitation powers (due, e.g., to a blue-shift of the dispersion) as a mechanism for the limitation of the 2D GS size. Thus, the intrinsic 2D GS size at SAW power $P_{RF} = 25\,mW$ is approximately $31\,\mu m$. The intrinsic size is here the size, when no constraints are applied.

The same analysis was applied to determine whether 1D MQSs have an intrinsic size with a corresponding coherence length $L_{coh,\,\Gamma\to X}^{1D\,MQS}$, too. Figure 4.26 displays these experimental results and clearly states that $L_{coh,\,\Gamma\to X}^{1D\,MQS}$ is independent on the size ϕ_L of the laser spot. $L_{coh,\,\Gamma\to X,\,120\mu m}^{1D\,MQS}$ (blue curve) and $L_{coh,\,\Gamma\to X,\,70\mu m}^{1D\,MQS}$ (red curve) of 1D MQSs excited with a laser spot with $\phi_L = 120\,\mu m$ and $70\,\mu m$, respectively, have a similar dependence on the laser power P_L. Note that there are only 3 recorded $L_{coh,\,\Gamma\to X,\,120\mu m}^{1D\,MQS}$ points for the 1D MQSs, which were excited with a large laser spot, which was due to the limited available laser power.

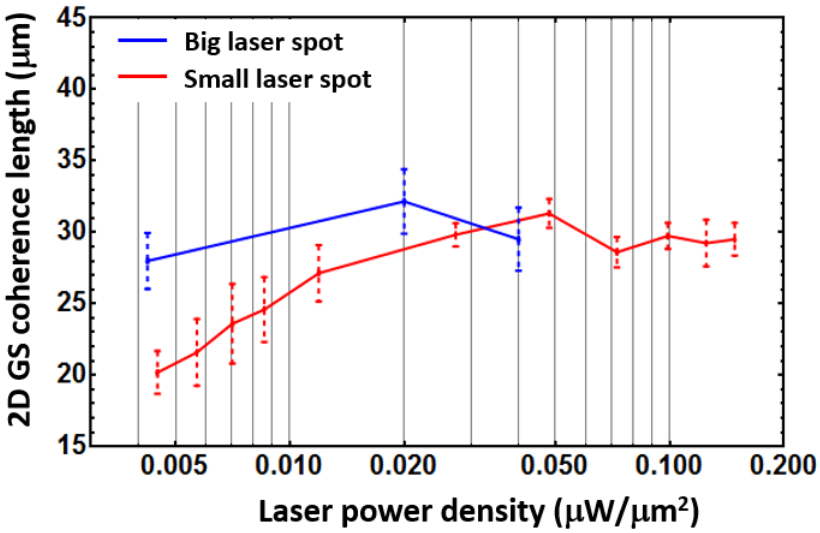

Figure 4.25: Dependence of the coherence length of 2D GS on the laser power for two different sizes of the exciting laser spot. The SAW power was set to 25 mW. The solid lines are a guide for the eye.

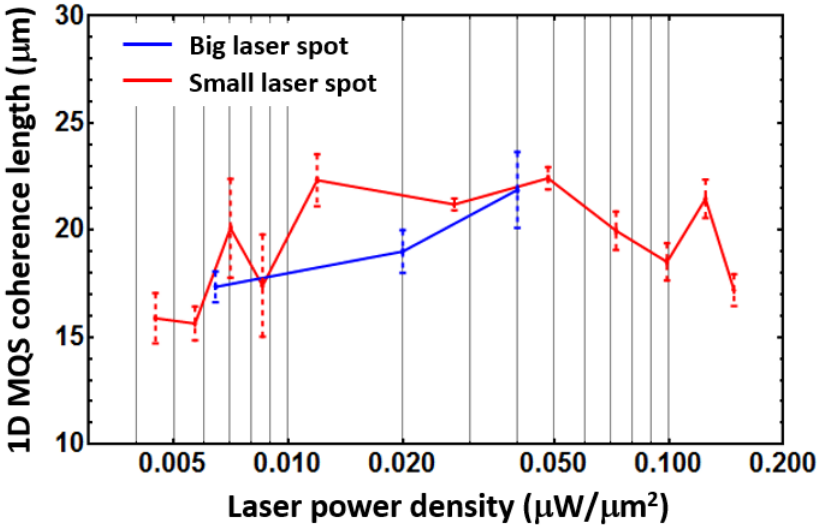

Figure 4.26: Dependence of the coherence length of 1D MQS on the laser power for two different sizes of the exciting laser spot. The SAW power was set to 25 mW. The solid lines are a guide for the eye.

4.2.5 Theoretical model

In order to qualitatively explain the experimental tomography results and to understand the nature of the 2D GS and 1D MQS states, a theoretical model based on the variational solution of the time-independent Gross-Pitaevskii equation (GPE) in the mean-field approximation was applied. The lowest energy eigenstates for an assumed trial wavefunction Ψ_{trial} with free parameters have been numerically probed and enabled one to determine the GPE solutions with respect to the free parameters. Critically, it is to emphasise that this method only considers the energetic configuration of the signal state in the optical parametric oscillator (OPO) process. However, previous investigations [75] have shown that such procedures deliver results compatible with a full numerical solutions of GPE taking into account the complete OPO process, i.e. considering both, the signal and the idler states, as well as the dissipative character of the exciton-polaritons. The interested reader is referred to [84], [85] and [86] for detailed discussions. Full numerical modelling requires many resources for computation but the same physical insights can be obtained using the variational approach to calculate the GPE solutions and to probe the experimental results.

Variational approach

The time-independent GPE-Hamiltonian in the mean-field approximation modified for the present problem reads

$$\hat{H}_{GPE} = -\frac{1}{2}\frac{\hbar^2}{m_p}\hat{\nabla}^2 + \hat{V}_{SAW} + g \parallel \hat{\Psi} \parallel^2 . \tag{4.2.4}$$

The general form of the GPE plays an important role in the quantum mechanical description of bosonic systems such as Bose-Einstein condensates (BEC), superconductivity and superfluidity [87], [88]. Even fundamental questions regarding the explanation of the dark matter and dark energy in the universe can be answered using GPE Ansatz [89]. For this work more important is that solutions describing solitonic states can be found using Eq. 4.2.4 [92]. The GPE is given by

$$\hat{H}_{GPE}\,\Psi = \left(-\frac{1}{2}\frac{\hbar^2}{m_p}\hat{\nabla}^2 + \hat{V}_{SAW} + g \parallel \hat{\Psi} \parallel^2\right) \Psi = E\,\Psi, \tag{4.2.5}$$

where m_p is the mass of the interacting particles and $g = 10\,\mu eV\,\mu m^2$ is their interaction constant [75]. GPE has the mathematical form of the non-linear Schrödinger equation, which accounts the kinetic energy term, the external acoustic potential $\hat{V}_{SAW} = -\Phi_{SAW}\left[\cos\left(k_{SAW}\,\hat{x}\right) + \cos\left(k_{SAW}\,\hat{y}\right)\right]$ as well as the non-linear inter-particle interactions.

The use of the time-independent GPE in the following variational calculation of the present non-equilibrium problem is justified by the long coherence time, i.e. a few hundred of ps, of the exciton-polariton condensates compared to the short lifetime of the photons in the microcavity (tens of ps). Thus, exciton-polariton condensates

can be considered as in quasi-equilibrium [90], [91]. As well, the simplification of the GPE by the mean-field approximation is appropriate, since the experimentally studied exciton-polariton condensates can be seen as a diluted gas, where average particle spacing is greater than their scattering length.

To find the stationary solutions of Eq. 4.2.5 in a square lattice, the stationary trial wavefunction of exciton-polariton condensates in the xy-plane can be sought in the form:

$$\Psi_{trial}\left(x,y\right) = F\,\exp\left(-\left(\frac{x}{r_x}\right)^2\right)\exp\left(-\left(\frac{y}{r_y}\right)^2\right)\,\cos\left(k_0\,x\right)\cos\left(k_0\,y\right), \tag{4.2.6}$$

where

$$F = 2\sqrt{\frac{N}{\pi}}\,\sqrt{r_x r_y\left(\exp\left(-k_0^2\left(r_x^2+r_y^2\right)\right)+\exp\left(-k_0^2 r_x^2\right)+\exp\left(-k_0^2 r_y^2\right)+1\right)}^{-1} \tag{4.2.7}$$

is the normalisation factor of the trial wavefunction, i.e. $\langle\Psi_{trial}|\Psi_{trial}\rangle = N$. N is the number of the (repulsively, non-linearly interacting) exciton-polariton particles.

Ψ_{trial} has a Gaussian envelope function underlining the Gaussian intensity profile of the excitation laser spot used in the experiments. The parameters r_x and r_y are directly related to the coherence length L_{coh} of Ψ_{trial} by $L_{coh}^{x,y} = 2\sqrt{2\,ln2}r_{x,y}$ and k_0 is the wavevector of Ψ_{trial}.

The numerical procedure of the variational calculus involves the minimisation of the functional $\digamma$, i.e. the minimisation of the energy of the eigenstates of the exciton-polariton condensates, with respect to the free parameters r_x, r_y and k_0,

$$\digamma = \langle\Psi_{trial}|\hat{H}_{GPE}|\Psi_{trial}\rangle. \tag{4.2.8}$$

The stationary solutions of Eq. 4.2.5 are only obtained, when

$$\frac{d}{d(r_x,\,r_y,\,k_0)}\digamma = 0. \tag{4.2.9}$$

Therefore, the applied numerical minimisation method searches a (global) minimum of Eq. 4.2.8 in a four dimensional space spanned by $\digamma(r_x,\,r_y,\,k_0)$, r_x, r_y and k_0. Although the energy of exciton-polariton condensate states depends on the parameters N and Φ_{SAW}, they are fixed in the calculus since they are constant in the experiment. N and Φ_{SAW} are determined by the excitation laser power P_L and the SAW power P_{RF}, respectively. In the calculations, in order to fit the experimental data, it was set: $N = 100$ and $\Phi_{SAW} = 200\,\mu eV$. Furthermore, the calculations were carried out using $m_p = 6\times10^{-5}\,m_e$, where m_e is the free electron mass, and $k_{SAW} = \frac{2\pi}{\lambda_{SAW}}$ with $\lambda_{SAW} = 8\,\mu m$.

The numerical results of the above described variational approach are presented in Fig. (4.27). Figure (4.27) shows the calculated local energy minima, which are

marked as M_1, M_{2x} and M_{2y}. The absolute energy minimum that is associated with $k_0 = 0$ and the r_x, $r_y \to \infty$, i.e. the Γ-state, lies outside the plot range and will not be discussed here. The local energy minima M_1, M_{2x} and M_{2y} represent extended modes spreading over several lattice unit cells. They indicate the theoretical possibility for the formation of exciton-polariton condensates with symmetric ($r_x = r_y$) and asymmetric ($r_x \neq r_y$) coherence lengths $L_{coh}^{x,y}$. Their corresponding wavevectors are $k_0^{M_1} \approx 0.45\, k_{SAW}$ and $k_0^{M_{2x,2y}} = 0.41\, k_{SAW}$ and thus, the calculated states of the exciton-polariton condensates form within the first MBZ of the square lattice since $k_0 < k_{SAW}/2$.

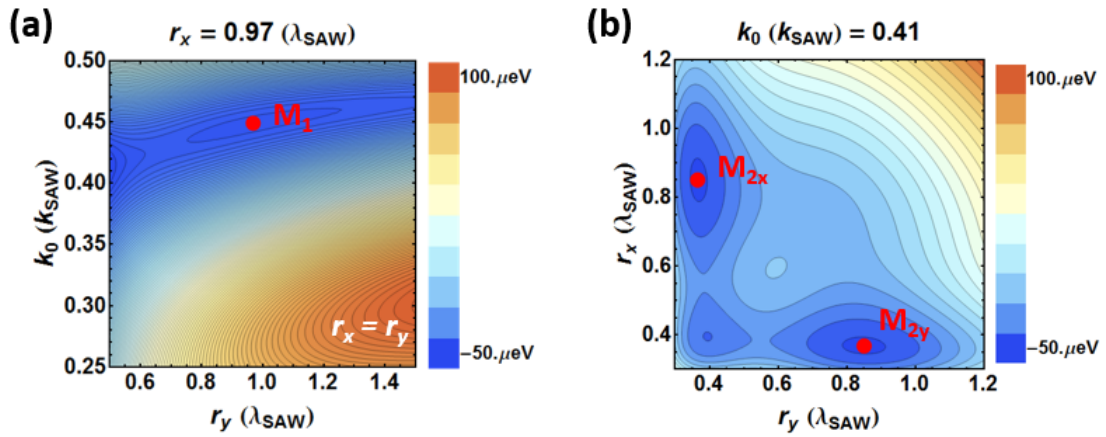

Figure 4.27: Energy maps of the functional F show two stationary solutions, [81]. The lowest energy of Ψ_{trial} is obtained when (a) $r_x = r_y$ and $k_0 \approx 0.45\, k_{SAW}$ and (b) $r_x \neq r_y$ and $k_0 \approx 0.41\, k_{SAW}$. M_1 is a local energy minimum corresponding to the 2D GS state, whereas M_{2x} and M_{2y}^{y} are two degenerate solutions reproducing the M → X-states. The energy of the M_1 state are within the single-particle bandgap. The absolute energy minimum is associated with the Γ-state, i.e. a state with $k_0 = 0$ and the r_x, $r_y \to \infty$, lies outside the plot range.

Variational solution M_1

M_1 represents the solution for the exciton-polariton condensate with symmetric Gaussian coherence lengths, i.e., $L_{coh}^{x} = L_{coh}^{y} = L_{coh}^{GS}$, of approx. $2.3\, \lambda_{SAW}$ in x- and y-direction. The solution M_1 is in agreement with Ref. [75] and is the variational solution for a 2D GS with its energy within the single-particle bandgap at the M-point of the folded exciton-polariton dispersion (cf. Fig. 2.10(a)).
The variational solution provides quantitative values of the parameters r_x, r_y and k_0, which can be used to display the 2D GS wavefunction just by plugging in their values into the assumed trial wavefunction Ψ_{trial}. Fig. 4.28 shows the squared amplitude of the calculated 2D GS wavefunction $\| \Psi_{2D\,GS} \|^2$ in real-space as well as in the momentum-space. In the real-space, $\| \Psi_{2D\,GS} \|^2$ is square-like and consists of an array of dots separated from each other by λ_{SAW}. With the naked eye one sees that

$\| \Psi_{2D\,GS} \|^2$ has an extension of approximately $3\,\lambda_{SAW} \times 3\,\lambda_{SAW}$. In momentum-space, $\| \Psi_{\Psi_{2D\,GS}} \|^2$ is concentrated at and close to the corners of the first MBZ, i.e. the M-points, where $k_0 = k_{SAW}/2$. This implies that the phase of the wavefunction of the 2D GS changes by roughly 180 degrees between consecutive periods (cf. Figure 4.28(b)).

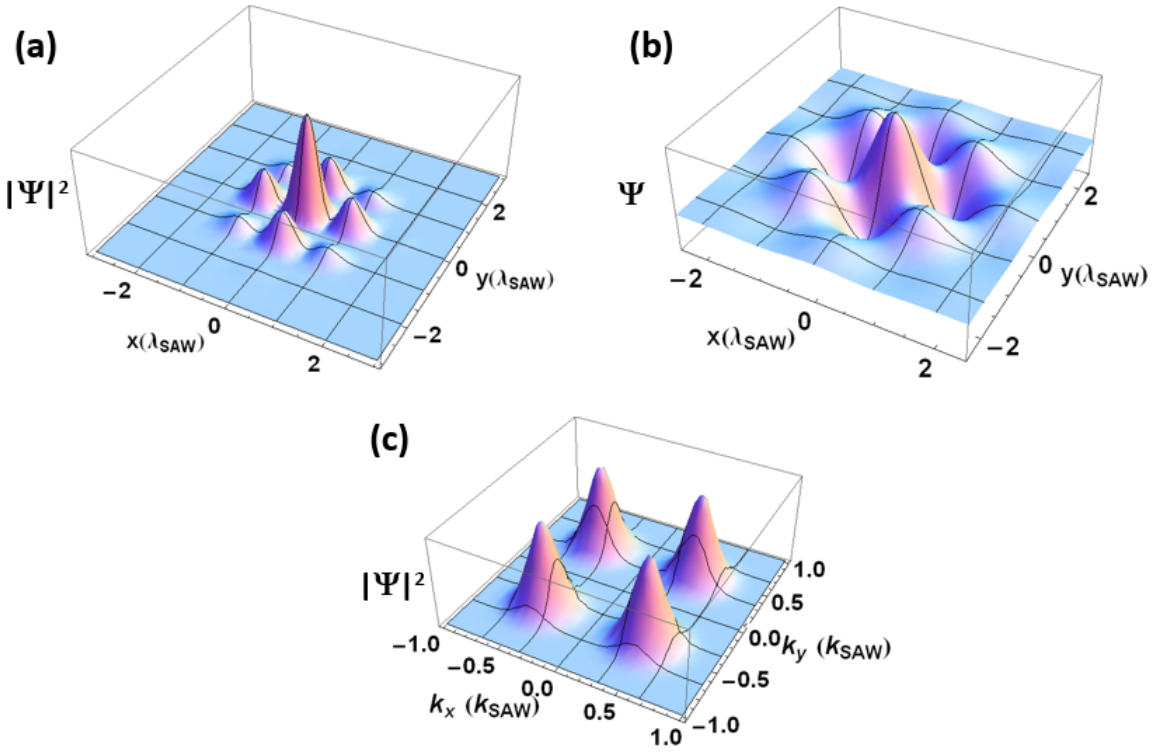

Figure 4.28: Calculated 2D GS wavefunction in (a)-(b) real- and (c) momentum-space representation (adopted from [81]).

Variational solutions M_{2x} and M_{2y}

The variational solutions for the exciton-polariton condensates that form 1D MQSs with the M $\rightarrow$ X-symmetry in momentum-space were calculated by exploring the parameter region, where $r_x \neq r_y$. The functional energy plot (cf. Fig. 4.27(b)) reveals in this case two degenerate modes M_{2x} and M_{2y} with extended coherence along one direction ($\sim 2 - 3\,\lambda_{SAW}$) and reduced coherence ($\sim 1\,\lambda_{SAW}$) along the perpendicular one. The wavefunction representations of mode M_{2x} in real- and momentum-space are displayed in Figs. 4.29(a) and 4.29(b), respectively. The corresponding plots for the solution M_{2y} can be obtained by simply interchanging the x- and y-axis (or k_x- and k_y-axis). Thus, M_{2x} and M_{2y} represent two perpendicularly orientated exciton-polariton condensates, which are both wire-liked shaped. Remarkably, this simple variational approach reproduces the experiment results with an excellent qualitative agreement (cf. Figs. 4.11 and 4.14).

Similar objects (called "in-band" solitons) have been observed in nonlinear crystals [93]. The fact that the band effective mass of exciton-polaritons is negative in the X $\rightarrow$ Γ-direction allows them to self-localise in a similar way as the 2D GS wave packet as discussed in the Subsec. 2.5.3, conferring them a solitonic character. At small particle number or weak interactions, their energy lies within the energy band of the lattice dispersion, but if the interactions are strong enough, they may also rise within the gap, thus becoming one-dimensional gap-solitons. The present model predicts correctly the existence of these states. Additionally, in the tomography experiments one observes a marked blue-shift and flattening of the dispersion along M $\rightarrow$ X (cf. Fig. 4.14), which give some evidence of this kind of behaviour. The transition from the in-band soliton to the gap-soliton is continuous. However, the detailed characterisation of this transition is beyond the scope of this work and is left as a mark for the outlook.

Based on these results, the k-space tomograms in Figs. 4.11 and 4.14 with energy $E^{1D\,MQS}$ are attributed to the incoherent superposition of the wave functions of the solutions M_{2x} and M_{2y}, which form around the central 2D GS state. The incoherent superposition of M_{2x} and M_{2y} is shown in the Fig. 4.30. Its comparison with the experimental results (cf. Figs. 4.11 and 4.14) reveals a good agreement between the results of the theoretical model and the experimental findings.

A final important question addresses the spatial separation between the 2D GS and 1D MQSs with the M $\rightarrow$ X symmetry. In particular, why do the latter only form at the flanks for the excitation laser spot? A possible explanation relies on the fact that the effective mass of the exciton-polaritons at the X-points of the MBZ is positive along X $\rightarrow$ M and negative along X $\rightarrow$ Γ. This makes the excitation of M_{2x} and M_{2y} states at the centre of the illumination spot with a Gaussian intensity profile less probable than the M_1 states. The situation becomes different in the ring around the central 2D GS, which is subject to a radial energy gradient due to the decaying particle densities and to a highly asymmetric illumination intensity profile. Additionally, this gain region has a ring-shape due to the depletion of the central part by the 2D GS states. Thus, the reduction in symmetry in the pump and signal states must induce a preferential formation of M $\rightarrow$ X-states in this region. Note, the variational procedure described above does not account for the shape of the excitation laser spot and/or any energy gradient.

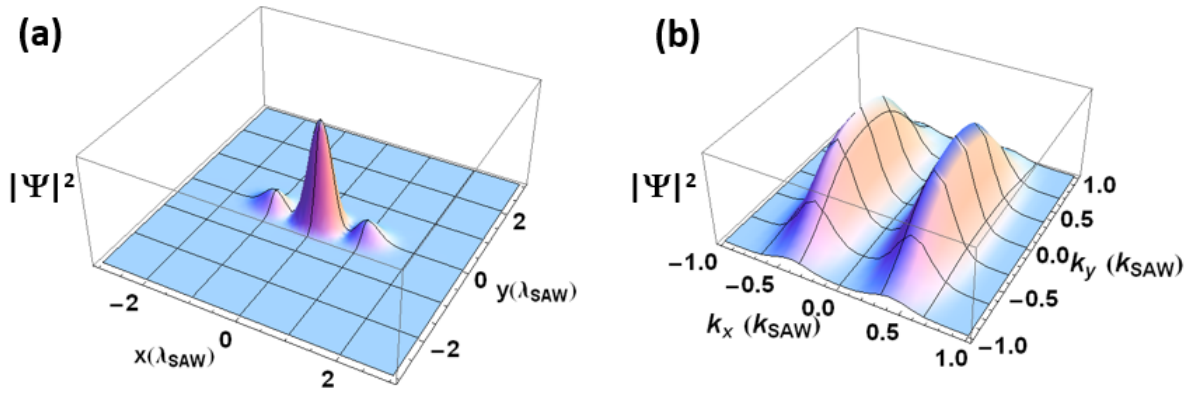

Figure 4.29: (a) Real- and (b) momentum-space representation of the calculated wavefunction for the solution M_{2x} (adopted from [81]).

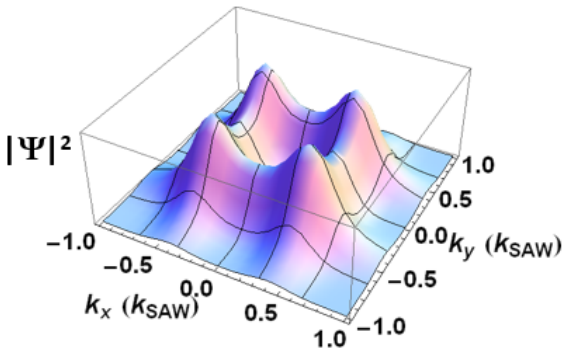

Figure 4.30: Momentum-space representation of the (incoherent) superposition of the calculated wave functions from M_{2x} and M_{2y} (adopted from [81]).

Dependence of the variational solutions on the laser power and SAW power

The dependence of the laser power P_L and SAW power P_{RF} in the variational solutions can be taken into account in the model by varying the parameters N and Φ_{SAW}, respectively. The parameter N describes the number of excited, i.e. injected, exciton-polaritons and thus, it is directly related to P_L since one has: $N \propto P_L$. Whereas Φ_{SAW} is the amplitude of the potential of the acoustic square lattice and it reflects P_{RF} due to their interdependence: $\Phi_{SAW} \propto \sqrt{P_{RF}}$. In the following the dependence of the formation of the 2D GS and 1D MQS as well as their properties, such as their coherence lengths and wavevectors, on the parameters N and Φ_{SAW} is discussed.

Fig. 4.31 displays the dependence of the coherence length $L_{coh}^{2D\,GS}$ and $L_{coh}^{1D\,MQS}$ of the 2D GS and 1D MQS in the momentum-space, respectively, on the number N of injected exciton-polaritons. Here, the acoustic potential Φ_{SAW} was fixed at 200 μeV.

As discussed before, the 2D GS state is symmetric in the xy-plane, whereas 1D MQS is asymmetric. The longer coherence length of 1D MQS, i.e. the coherence length determined from the FWHM of the k-peak at the X-point along the $\Gamma \rightarrow$X-direction in the MBZ, will be denoted by $L^{1D\,MQS}_{coh,\,\Gamma\rightarrow X}$, whereas the short one, i.e. the coherence length determined from the FWHM of the k-peak at the X-point along the M$\rightarrow$X-direction, will be indicated by $L^{1D\,MQS}_{coh,\,M\rightarrow X}$. Fig. 4.31 reveals following points:

- The coherence lengths $L^{2D\,GS}_{coh}$ (red curve) and $L^{1D\,MQS}_{coh,\,\Gamma\rightarrow X}$ (green curve) of the 2D GS and 1D MQS, respectively, increase with N. This is due to the increasing polariton-polariton interaction energy, which is proportional to $g\,N$. One expects that the size of the 2D GS as well as of the 1D MQS continues to grow as N increases.

- The coherence length $L^{1D\,MQS}_{coh,\,M\rightarrow X}$ (blue curve) of 1D MQS is independent on N.

When the coherence length L^{GS}_{coh} and/or $L^{1D\,MQS}_{coh,\,\Gamma\rightarrow X}$ of the 2D GS state and/or of 1D MQS, respectively, increases, their associated wavevector k_0 approaches the value $k_{SAW}/2$, which is the corner of the MBZ (cf. Fig. 4.32). Accordingly, the confinement of the condensates must decrease. This is not surprising, since with increasing N the energy of the condensates, i.e. 2D GS state and 1D MQS, blue-shifts and thus, it screens the SAW induced acoustic potential Φ_{SAW}. The dependence of k_0 on Φ_{SAW} is discussed in detail in Ref. [75].

Finally, Fig. 4.33 summarises one of the most important findings of this thesis, namely, the dependence of the formation of the 2D GS states and 1D MQS on the excitation power, given by N, and the acoustic potential Φ_{SAW}. As already indicated in Fig. 4.31, the 2D GS states as well as 1D MQS can be only excited within a certain range of N and Φ_{SAW}. With increasing Φ_{SAW}, the number N of particles required to form the 2D GS and/or 1D MQS reduces. Interestingly, according to the model the range $[N_{min},\, N_{max}]$ expands for smaller Φ_{SAW}. However, at low or high values of Φ_{SAW} solitonic states cannot be formed. Moreover, Fig. 4.33 illustrates that at constant Φ_{SAW} the formation of 2D GS states occurs at a lower N in comparison to 1D MQS. Accordingly, the variational solutions predict that - under the given parameters - 1D MQS cannot be lonely excited. Despite the simplicity of the model, all these results are in agreement with the experimental observations.

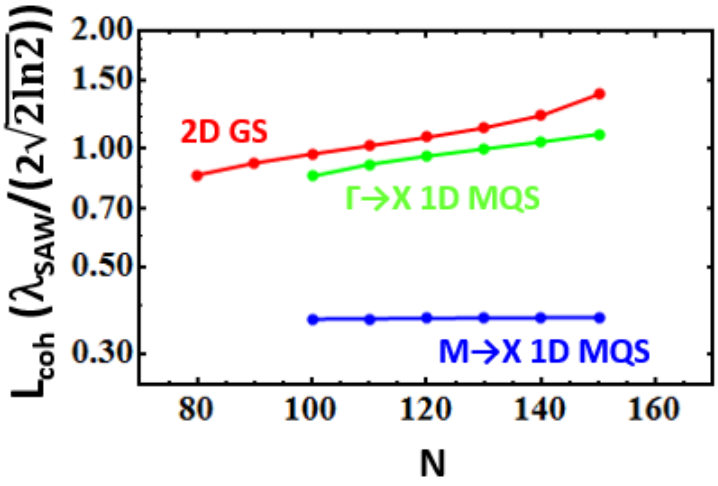

Figure 4.31: Calculated dependence between the coherence lengths and the number N of polaritons for the solutions M_1 and M_{2x}. The parameter Φ_{SAW} is fixed, Φ_{SAW}=200 μeV.

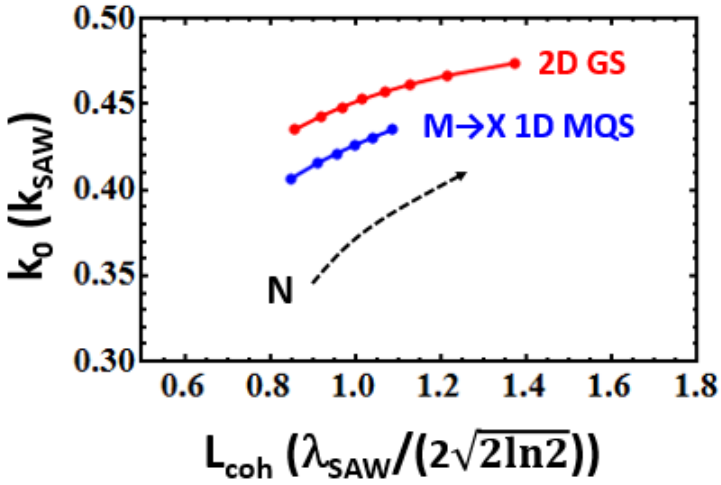

Figure 4.32: Calculated dependence between the wavevector k_0, the coherence lengths and the number N of polaritons for the solution M_1 and M_{2x}. The parameter Φ_{SAW} is fixed, Φ_{SAW}=200 μeV.

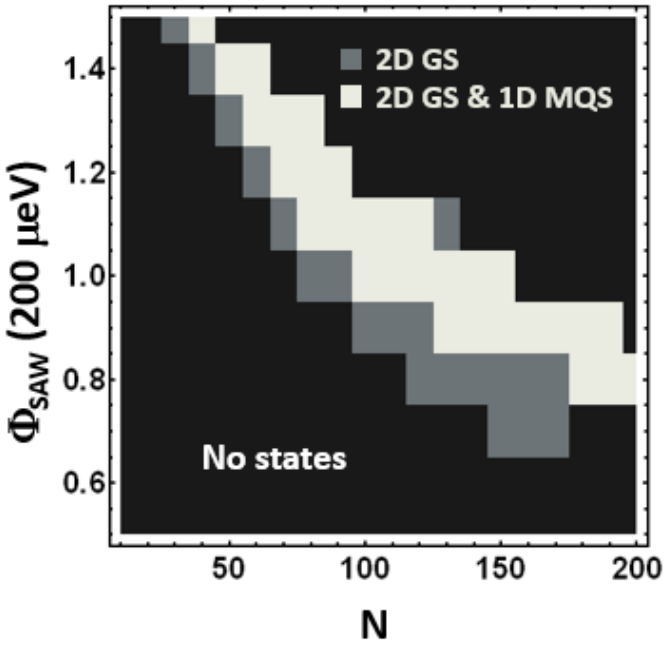

Figure 4.33: Calculated dependence between the formation of macroscopic quantum states on the number N of polaritons and the SAW power Φ_{SAW}

4.3 Dynamics of Exciton-Polariton Gap Soliton in Moving Square Lattices

Previous investigations on exciton-polaritons and 2D GS in acoustic lattices have been carried out using optical spectroscopy in the continuous wave (cw) domain and were, therefore, unable to capture the 2D GS temporal dynamics in the moving acoustic lattice. In the following, this issue is addressed via photoluminescence (PL) studies carried out with temporal and spatial resolutions, which are much shorter than the temporal and spatial SAW periods, respectively.
In the following, first the experimental technique employed to map the time-dependent 2D GS wavefunction in real- and momentum (k-) space is described (Subsec. 4.3.1). Then PL images of the 2D GS wavefunction recorded without and with time resolution are compared. The latter clearly shows the motion of the lattice created by the SAWs with the acoustic velocity. Interestingly, it was found that the PL intensity emitted by the 2D GS oscillates with the position of the lattice relative to the exciting laser beam (to be denoted later as the lattice phase). The PL oscillation amplitude depends both on the PL intensity and the size ϕ_L (quantified by the full width at half intensity maximum (FWHM)) of the laser spot, and increases considerably for excitation intensities close to the condensation threshold for 2D GS formation. These oscillations are explained by a model that takes into account the combined effects of SAW reflections at sample boundaries and defects as well as the spatial phase of the acoustic lattice within the laser spot.

4.3.1 Experimental details of the time-resolved measurements

The time-resolved experiments of the exciton-polariton condensates in real- and k-space were realised using a streak-camera with a temporal resolution of $50\,ps$. The streak-camera was triggered by the RF-signal used to generate the SAWs. In order to obtain full time-resolved real- and k-space images, the energy-integrated PL was projected onto the (horizontal) slit at the input of the streak-camera and scanned vertically to obtain time-resolved image sections (cf. Fig. 4.34) in analogy to the tomographic measurements as discussed in the previous Section. Then complete images for the time $t = t'$ were reconstructed by composing together the signals at t' from each of these sections. In this way, a six-dimensional set of data (x, y, k_x, k_y, time t, PL intensity) was obtained (cf. Fig. 4.35). Note, only the energy-integrated square module $\| \Psi_{2D\,GS} \|^2$ of the 2D GS wavefunction $\Psi_{2D\,GS}$ is recorded.

The spatial resolution of the full real- and k-space images was set by the pixel size ($15\,\mu m \times 15\,\mu m$) of the streak-camera screen as well as by the optical magnification of the real- and k-space images (cf. Fig. 4.5). Thus, the resolution in the real-space was $0.75\,\mu m$ in the x- and y-direction. The k-space resolution was $4 \times 10^{-2}\,\mu m^{-1}$ in k_x and k_y.

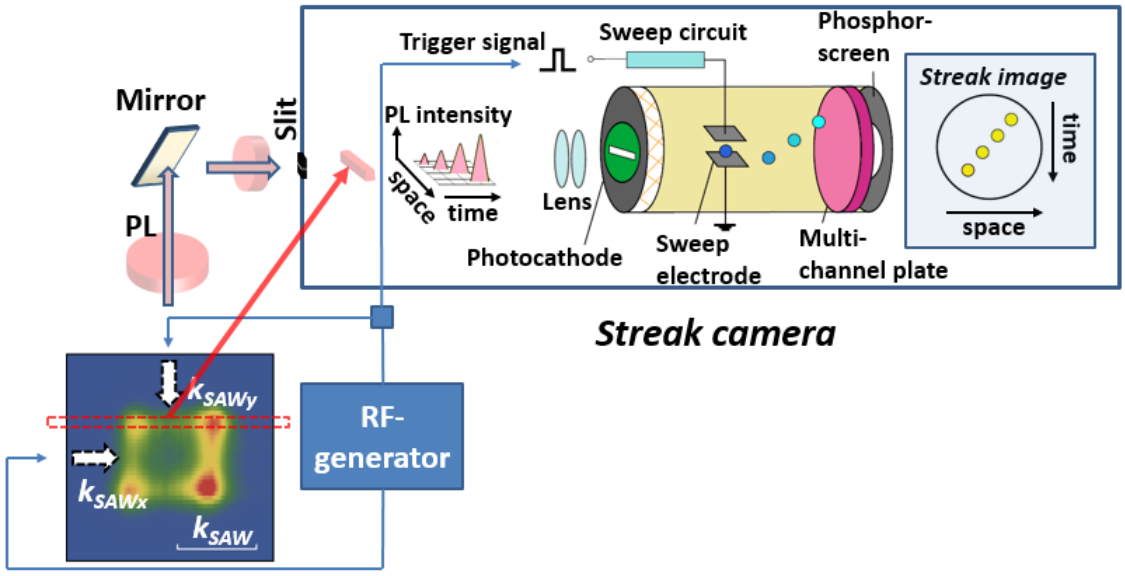

Figure 4.34: Scheme of the experimental set-up to perform time-resolved measurements using a streak-camera

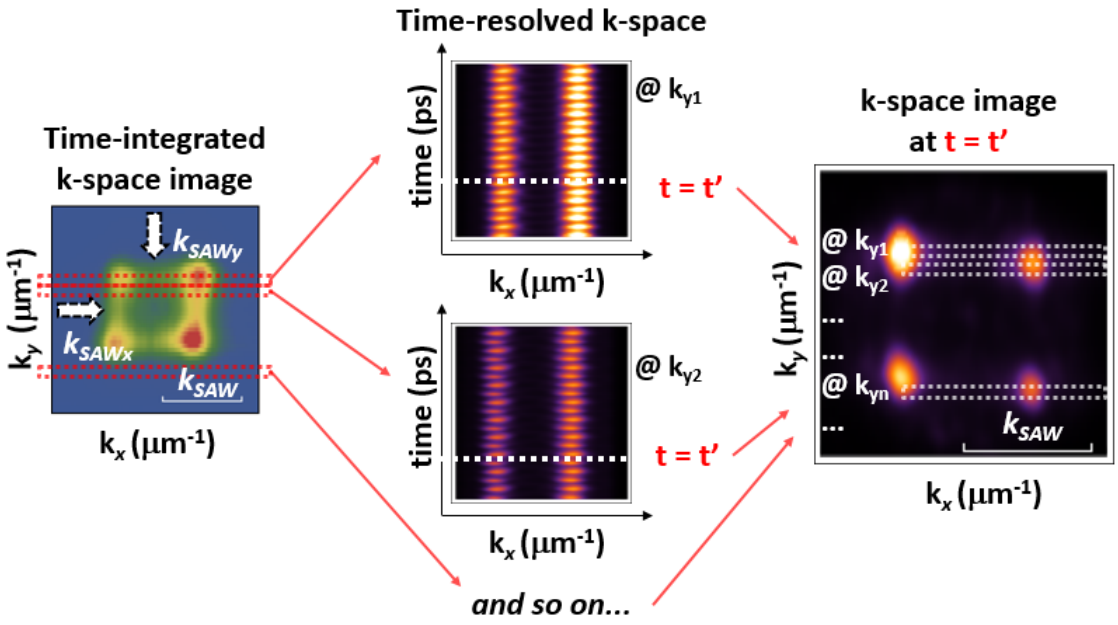

Figure 4.35: Principle of the time-resolved measurement

The laser excitation power P_L and the size ϕ_L of the laser excitation spot were varied in order to investigate the PL dynamics, the dimensions as well as the coherence lengths of the exciton-polariton condensates. The RF-power applied to the IDT for SAW generation was set to $30\,mW$. ϕ_L was either set to $60\,\mu m$ or $100\,\mu m$. The laser power P_L ranged from $P_L = P_{th}$ to $6\,P_{th}$, where P_{th} is the optical threshold power for the formation of the exciton-polariton 2D GS state.

When the above experimental set-up was used, each time-resolved image section was acquired during the forwardtrace of the streak camera and then - after a hold - during the backtrace of the voltage streak as sketched in Fig. 4.36(a). Afterwards, the streak-camera software overlapped these recorded data with their correspondent time-scales (cf. Fig. 4.36(b)). The total time-scale was $26.4\,ns$ and $6.6\,ns$ of the forward- and backtrace, respectively.
The forward- and backtrace had different sweep speeds of the streak v_f and v_b, respectively, with the ratio $\frac{v_f}{v_b} = \frac{1}{4}$. Accordingly, the recorded spatial signals differed in frequency, e.g. four contantly moving dots (blue circles) vs. one dot (red circles) per sweep cycle were recorded by the forwardtrace and the backtrace, respectively, as illustrated in Fig. 4.36(b). These frequencies were related to each other by $\frac{f_f}{v_f} = \frac{f_b}{v_b}$, where f_f and f_b are the spatial frequencies of the forward- and backtrace, respectively. As well, the signal amplitudes A_f and A_b of the forward- and backtrace, respectively, were related by $\frac{A_f}{v_f} = \frac{A_b}{v_b}$.

In order to be able to analyse the data, these time-resolved images of the forward- and backtrace had to be seperated from each other. For that purpose, a Fourier analysis of the recorded data was performed by taking the advantage of the fact that the Fourier components of the modulated PL essentially vanished for high harmonics of the SAW frequency.
In the first step, the Fourier components of the forward- and backtrace were identified. Since there are in total only four Fourier components (cf. Fig. 4.36(c)), half of them at lower values (red circles) must originate from the backtrace, whereas the other half is due to the signals recorded by the forwardtrace (blue circles). In the second step, all data consisting of the Fourier components originating from the backtrace was removed. Thus, the remaining data was the time-resolved image section acquired by the forwardtrace, only. Furthermore, the first Fourier component of the forwardtrace must originate from a sinusoidal function at lower frequency. The second one represents a sinusoidal function with a higher, i.e. twice as high, frequency.
Note, the Fourier component at 0 (thin blue line) represents the time-independent background signal.

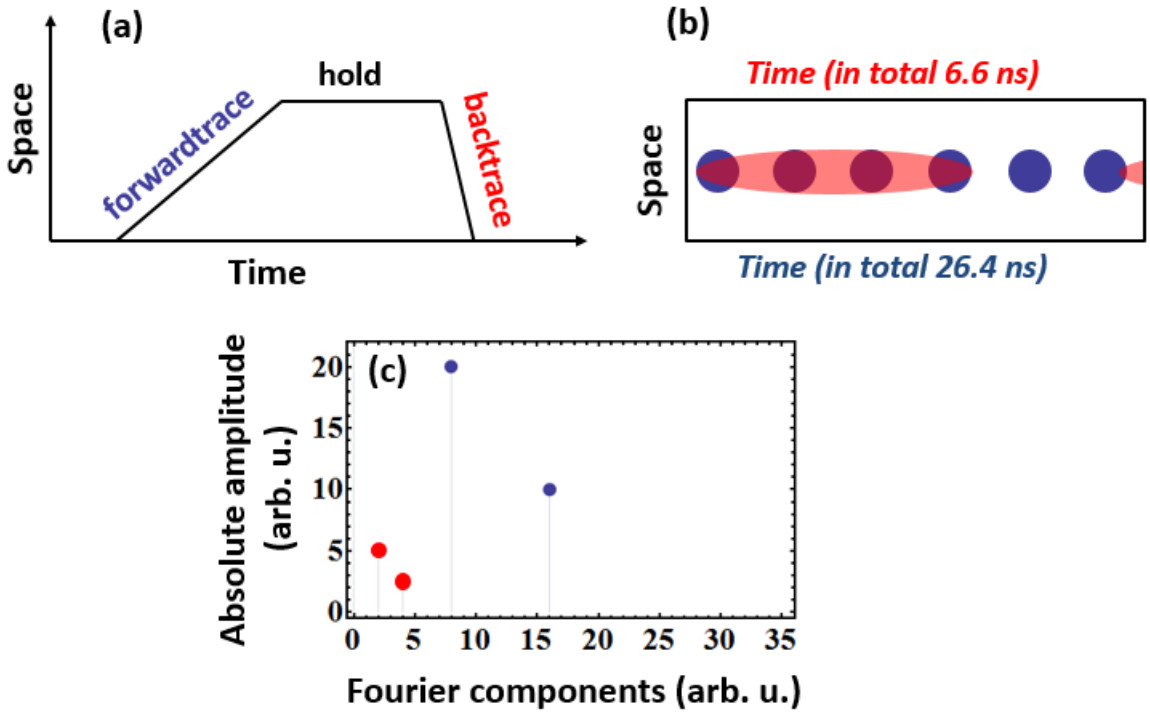

Figure 4.36: (a) Scheme of the streak-camera acquisition of a time-dependent signal with the corresponding (b) time-resolved image section and (c) Fourier components of the experimental recorded data for the laser power at the condensation threshold.

4.3.2 Experimental results

Figure 4.38(a)-(d) display time-resolved real-space images of the squared modulus of the 2D GS wavefunction $\Psi_{2D\,GS}$ recorded for an excitation power P_L close to the optical condensation threshold P_{th} at different time delays t_i ($i = 1...4$) as marked in Fig. 4.38(i). The rectangular shape of the dot array with elongation along the x-direction is attributed to the elliptic shape of the laser spot. In contrast to the time-integrated image Fig. 3.2 as shown in the Chapter 3, the time-resolved real-space images show a well-defined array of dots with periodicity λ_{SAW}, which moves with velocity v_{lat}. In order to visualise the lattice motion, white dashed circles in Figs. 4.38(b) and (d) show the position of the lattice dots at t_2. Between t_2 and t_4 the dots have moved by $0.4\,T_{SAW}\,v_{lat}$, where T_{SAW} is the SAW period.

The periodicity of the real-space images is consistent with the k-space emission pattern displayed in Figs. 4.38(e)-(h) (and also with time-integrated k-space image, cf. Fig. 3.2(b)). These images also prove that the emission from the M-points is present at all time delays and thus, the 2D GS formation is independent on the spatial phase of the acoustic square lattice.

A remarkable feature in the images of Figs. 4.38(a)-(h) is that the total PL emission intensity $I_{PL,T}$ oscillates in time t or, equivalently, with the position $v_{lat}t$ of the acoustic lattice. Figure 4.38(i) displays the time dependence of $I_{PL,T}$ (blue curve) determined by integrating the overall PL intensity emitted by the 2D GS. $I_{PL,T}$ displays two maxima per SAW period T_{SAW}. The relative variation $\Delta I_{PL,T}$ of $I_{PL,T}$ reaches up to 45% with respect to the time-averaged value $< I_{PL,T} >$ of $I_{PL,T}$. The 2D GS, therefore, blinks at twice the SAW frequency for optical excitation power close to the threshold. Since the emission intensity reflects the number of signal polaritons, these oscillations indicate that the optical injection efficiency into the signal polariton states changes with the spatial phase of the acoustic lattice. A detailed discussion of the origin of $\Delta I_{PL,T}$ will be addressed in the following Subsec 4.3.3.

A second interesting finding is the asymmetric shape of the time resolved profile displayed in Fig. 4.38(i), where the time delay between consecutive maxima (or minima) of $I_{PL,T}$ does not correspond to a submultiple of T_{SAW}. In fact, the $I_{PL,T}$-maxima in Fig. 4.38(i) are delayed by $(0.38 \pm 0.03)T_{SAW}$ from each other and also have different intensities. The minima of $I_{PL,T}$ are separated by $(0.62 \pm 0.03)T_{SAW}$. The corresponding Fourier analysis, which is based on the discrete Fourier transform of the experimental data set ($I_{PL,T}$, t), shows that the $I_{PL,T}$-profile consists of two Fourier components. The discrete Fourier transform v_s of a list u_r of length n of periodic data set is defined to be:

$$v_s = \frac{1}{\sqrt{n}} \sum_{r=1}^{n} u_r e^{2\pi i(r-1)(s-1)/n}. \tag{4.3.1}$$

The Fourier transform of a function of time is a complex-valued function. Its absolute value provides the information on the frequencies contained in the original

function, whereas its complex argument represents the phase offset in the sinusoidal functions of that frequencies.

Figure 4.37 displays the absolute values of the discrete Fourier transform of the experimental data set ($I_{PL,T}$, t). As mentioned before, there are two Fourier components, namely at the fundamental SAW frequency f_{SAW} and its 1st harmonics, i.e. at $2\,f_{SAW}$. Correspondingly, the function $I_{PL,T}(t)$ is composed of two sinusoidal functions:

$$I_{PL,T}(t) = A\,\sin\left(2\pi \times f_{SAW}t + \phi_A\right) + B\,\sin\left(2\pi \times 2\,f_{SAW}t + \phi_B\right). \qquad (4.3.2)$$

ϕ_A and ϕ_B are the phases and A and B are the amplitudes of the sinusoidal functions at the frequencies f_{SAW} and $2\,f_{SAW}$, respectively.
According to the results presented in Fig. 4.37, the amplitude A of the sinusoidal function at f_{SAW} is higher than of the one at $2\,f_{SAW}$, i.e. B. The ratio between A and B is 1.4. Thus, $I_{PL,T}(t)$ is dominated by the sinusoidal function at the fundamental SAW frequency f_{SAW}. As will be shown in the next Subsec., this is only true for the excitation power close to the condensation threshold.
The origin of the two maxima in the $I_{PL,T}$-profile, which differ in intensity, and their temporal separation of a non-submultiple of T_{SAW} must be due to the ratio of (i) A to B and/or (ii) ϕ_A to ϕ_B.

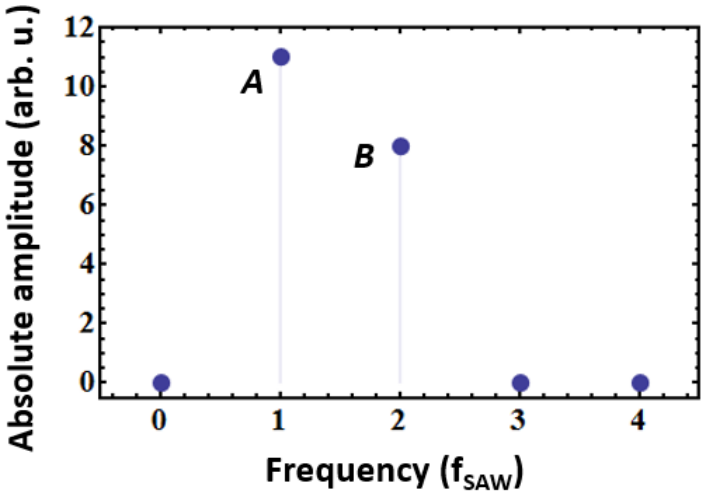

Figure 4.37: Fourier spectrum of the total PL emission intensity $I_{PL,T}$ of the 2D GS

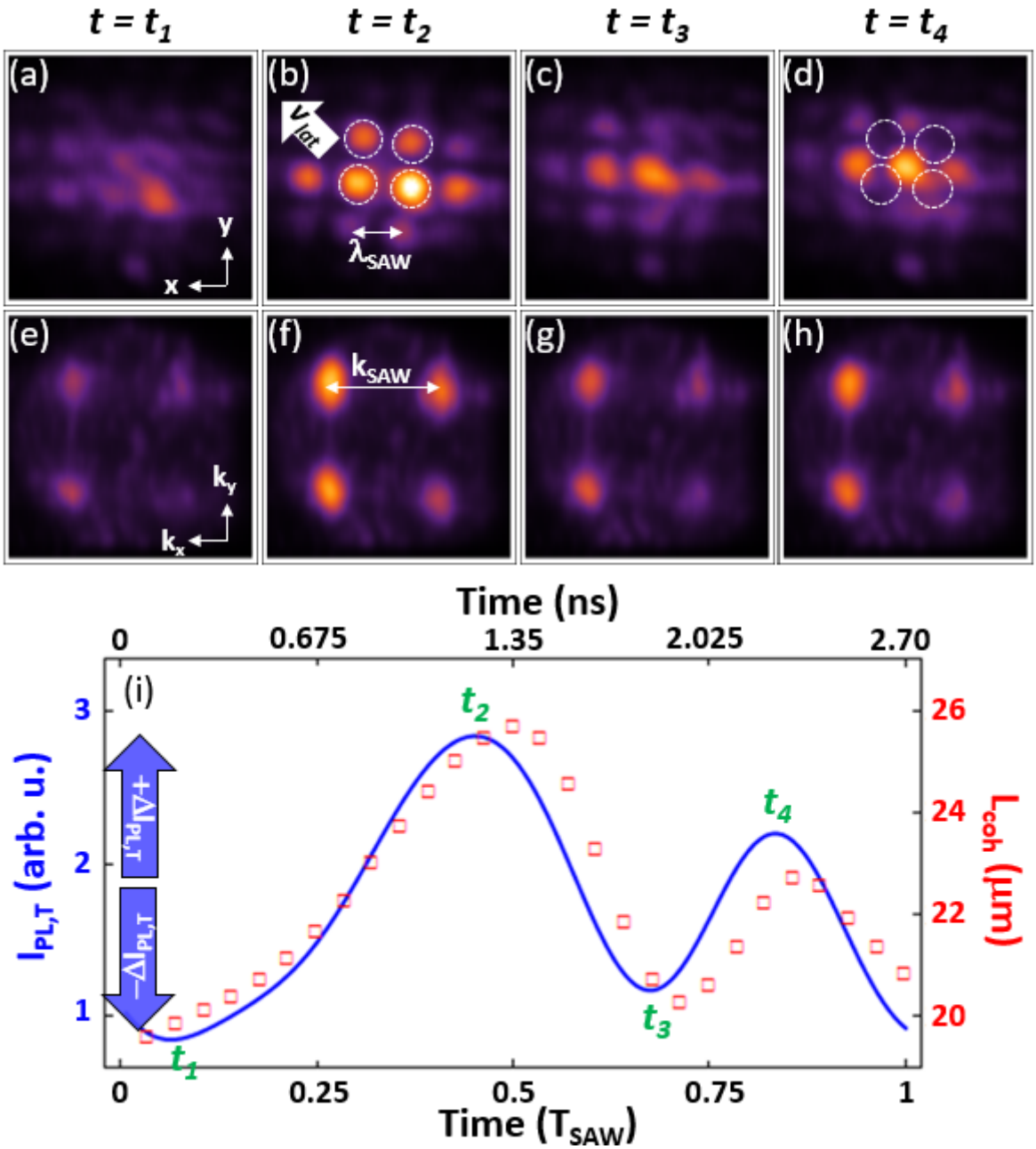

Figure 4.38: Time-resolved (a)-(d) real-space and (e)-(h) corresponding k-space images of $\| \Psi_{2D\,GS} \|^2$ recorded for an excitation power $P_L = P_{th}$ at the delays $t_1 \ldots t_4$ as marked in (i). To help the visualization of lattice motion with velocity v_{lat}, the dashed white circles show the position of the emission maxima at delay t_2. The intensity scale is the same for all images. (i) Integrated intensity $I_{PL,T}$ of PL images (blue curve) as well as the 2D GS coherence length $L_{coh}^{2D\,GS}$ (red squares) as a function of time. One acoustic period T_{SAW} equals $2.7\,ns$, [82].

Time-dependence of the 2D GS coherence length and its dependence on the laser power

The time-resolved experiments also allow one to follow the time evolution of the coherence $L_{coh}^{2D\,GS}$ of the 2D GS or, equivalently, the extension of its wavefunction. $L_{coh}^{2D\,GS}$ was determined using Heisenberg's Uncertainty Principle, i.e. $\Delta k\, L_{coh}^{2D\,GS} \geq 2\pi$, where Δk is the FWHM of the PL peaks at the M-points in the k-space (cf. Fig. 4.38(e)-(h)). Results recorded for $P_L = P_{th}$ are displayed by the red squares in Fig. 4.38(i). Interestingly, $L_{coh}^{2D\,GS}$ oscillates during the lattice motion between $(19.6 \pm 0.6)\,\mu m$ and $(25.7 \pm 0.8)\,\mu m$ following the temporal line shape of the total PL emission intensity $I_{PL,T}$. $L_{coh}^{2D\,GS}$ and $I_{PL,T}$ are apparently correlated (cf. Fig. 4.38(i)) as expected since a larger 2D GS should consist of more exciton-polaritons. Note that the $L_{coh}^{2D\,GS}$ line shape is shifted by approximately $150-200\,ps$ with respect to the $I_{PL,T}$-curve. This shift may originate from the finite coherence time of the 2D GS since the value of $150 - 200\,ps$ corresponds to the independently measured 2D GS coherence time in the sample used here [72]. However, a detailed analysis of the temporal evolution of $L_{coh}^{2D\,GS}$ is beyond the scope of the present work and must be addressed in further investigations. To the best of my knowledge, this is the first experimental observation of the temporal evolution of the 2D GS coherence length in acoustic square lattices. The time-averaged coherence length $< L_{coh}^{2D\,GS} >$ is $(22.4 \pm 2.1)\,\mu m$ and agrees well with the previously presented results in the Sec. 4.3.

$L_{coh}^{2D\,GS}$ $[\mu m]$ / P_L $[P_{th}]$	P_{th}	$2 \times P_{th}$	$6 \times P_{th}$
$< L_{coh}^{2D\,GS} >$	22.4 ± 2.1	29.1 ± 2.2	34.0 ± 2.6
min. $L_{coh}^{2D\,GS}$	19.6 ± 0.6	25.8 ± 0.8	30.4 ± 0.9
max. $L_{coh}^{2D\,GS}$	25.7 ± 0.8	32.2 ± 1.0	37.2 ± 1.1

Table 4.1: Dependence of the coherence length $L_{coh}^{2D\,GS}$ on laser power P_L. The errors result from inaccuracies in reading out Δk-values of the M-points.

$< L_{coh}^{2D\,GS} >$ depends on the excitation power P_L as quantitatively summarised in Table 4.1. As reported in the previous Subsec. 4.2.4, the time-integrated 2D GS coherence length $< L_{coh}^{2D\,GS} >$increases with increasing P_L, reaching a maximal value $< L_{coh}^{2D\,GS} >= (34.0 \pm 2.6)\mu m$. For all P_L, the time-resolved coherence length $L_{coh}^{2D\,GS}$ oscillates between minimal and maximal values, which increase with P_L, too. The difference $\Delta L_{coh}^{2D\,GS}$ between the minimal and maximal $L_{coh}^{2D\,GS}$ amounts to approximately $6 - 7\,\mu m$, i.e. approximately one spatial SAW period λ_{SAW}. $\Delta L_{coh}^{2D\,GS}$ is independent on the laser power. However, the 2D GS dimensions are dependent not only on the laser power P_L, but also on the lattice phase. The lattice phase determines the number of the SAW induced potential minima within the illuminated area, where exciton-polaritons are injected. The SAW potential minima are separated by λ_{SAW} from each other. If their number increases, there are more SAW potential minima, in which are exciton-polaritons are injected, and accordingly the 2D GS

has then a larger diameter. This explains the correlations between the line shape of the $L_{coh}^{2D\,GS}$-oscillations and $I_{PL,T}$-curves as shown in the Fig. 4.39.

Figures 4.39(a) and (b) show the time-resolved total PL emission intensity $I_{PL,T}$ of 2D GS for different excitation powers, i.e. $P_L = 2\,P_{th}$ and $P_L = 6\,P_{th}$, respectively. $I_{PL,T}$ increases with P_L as expected and oscillates, as well as $L_{coh}^{2D\,GS}$, with twice the SAW frequency within one acoustic period T_{SAW}. $I_{PL,T}$-oscillations are always present in the used laser power range.

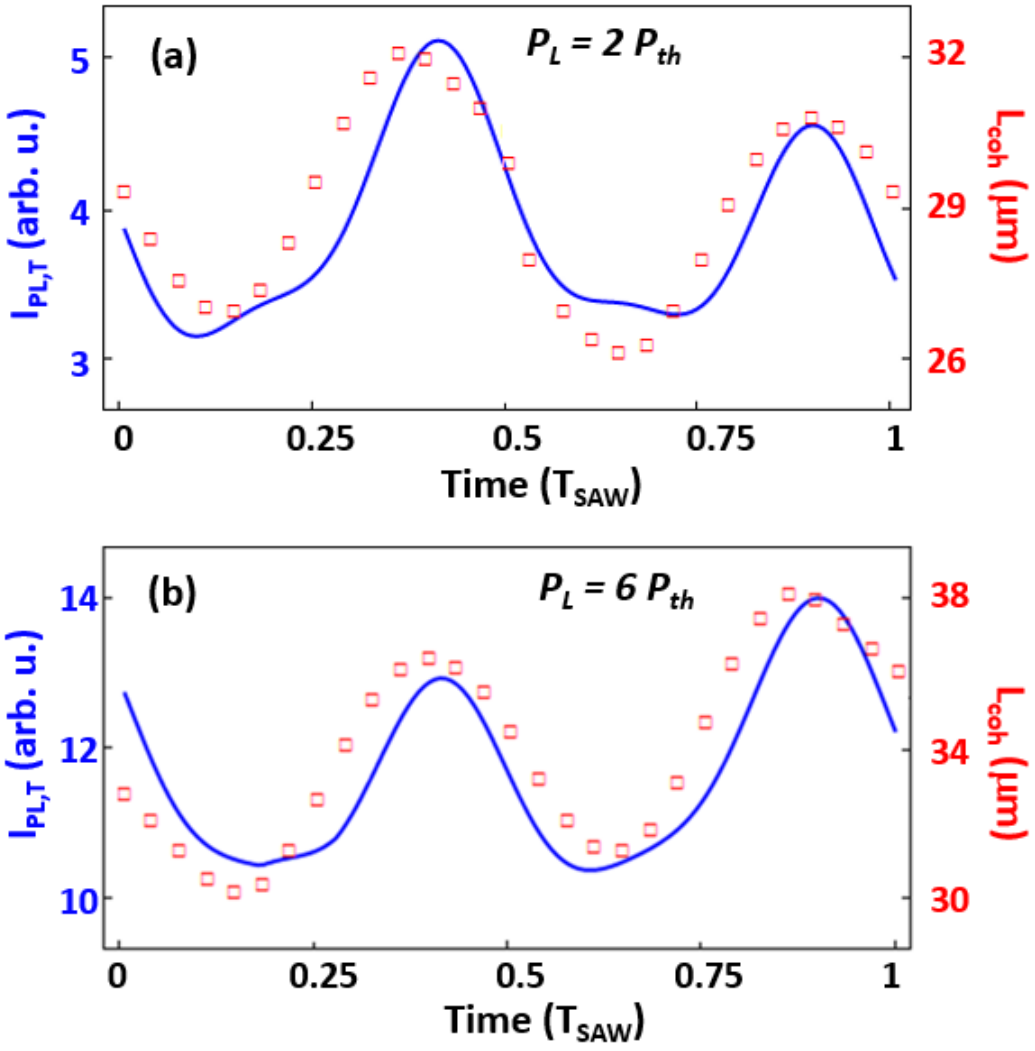

Figure 4.39: Integrated intensity $I_{PL,T}$ of PL images (blue curve) as well as the 2D GS coherence length $L_{coh}^{2D\,GS}$ (red squares) as a function of time for different laser powers: (a) $P_L = 2\,P_{th}$ and (b) $P_L = 6\,P_{th}$.

Dependence of the PL oscillations on the laser power

The time-resolved $I_{PL,T}$-profiles also depend on the laser excitation power P_L, as indicated by solid curves of Fig. 4.40. The relative difference in amplitude between the two maxima of $I_{PL,T}$ within a SAW cycle reduces with increasing P_L while their temporal separation approaches $0.5\,T_{SAW}$ (cf. Fig. 4.40). Note, in addition, that while the first maximum (indicated by the full arrows) has a higher intensity than the second one (dashed arrows) for excitation powers$P_L < 3P_{th}$, this situation can revert for higher powers. In the next Subsection, a model for the temporal variation of $I_{PL,T}$ is introduced, which can account for this behaviour. Furthermore, these findings indicate a strong reduction of the Fourier component at the fundamental SAW frequency f_{SAW} relative to the one at the 1st harmonics, which is indeed the case. The corresponding findings are displayed in Fig. 4.41. It shows that the ratio of the amplitudes B and A of the Fourier components at the $2\,f_{SAW}$ and f_{SAW}, respectively, strongly decreases at high P_L. The ratio $B/A > 1$ states that the oscillation of $I_{PL,T}$-curves is dominated by the 1st harmonics of f_{SAW}, i.e. $2\,f_{SAW}$. Accordingly, the relative difference between the $I_{PL,T}$-maxima or -minima should significantly reduce at high P_L. Indeed, this is experimentally observed as displayed in Figs. 4.39 and 4.40.

The line shape of the oscillations remains essentially constant when the size ϕ_L of the laser spot increases from $60\,\mu m$ to $100\,\mu m$, while retaining the same excitation density, as can be inferred from a comparison between the solid and dashed bottom curves in Fig. 4.40. The amplitude $\Delta I_{PL,T}$ of the oscillations, quantified by the ratio between the peak amplitude of the $I_{PL,T}$ oscillations relative to the time-averaged PL intensity $< I_{PL,T} >$, reduces when P_L is increased above the condensation threshold P_{th} (cf. inset of Fig. 4.40). In particular, the $\Delta I_{PL,T}$ reduces from 45% at $P_L = P_{th}$ to approximately 10% at $P_L = 6 \times P_{th}$. The quantitative relationship between $\Delta I_{PL,T}$ and P_L can be cast into the form:

$$\Delta I_{PL,T}(P_L) = A\,P_L^{-1} + B. \tag{4.3.3}$$

The parameter A describes the non-linear power dependence of $\Delta I_{PL,T}(P_L)$, whereas B is its asymptotic value at large P_L. The lines in the inset of Fig. 4.40 show a fit of the previous expression to the experimental results, which yields $A = (42 \pm 1)\%$ and (32 ± 2) for the measurements with ϕ_L of $60\,\mu m$ (full squares) and $100\,\mu m$ (empty squares), respectively. For both cases, $B = (3 \pm 1)\%$. In the previous Subsec. 4.2.4, it was shown that the spatial extension of the 2D GS increases with the size ϕ_L of the laser spot. In view of this result, the dependence of the parameter A on ϕ_L is expected.

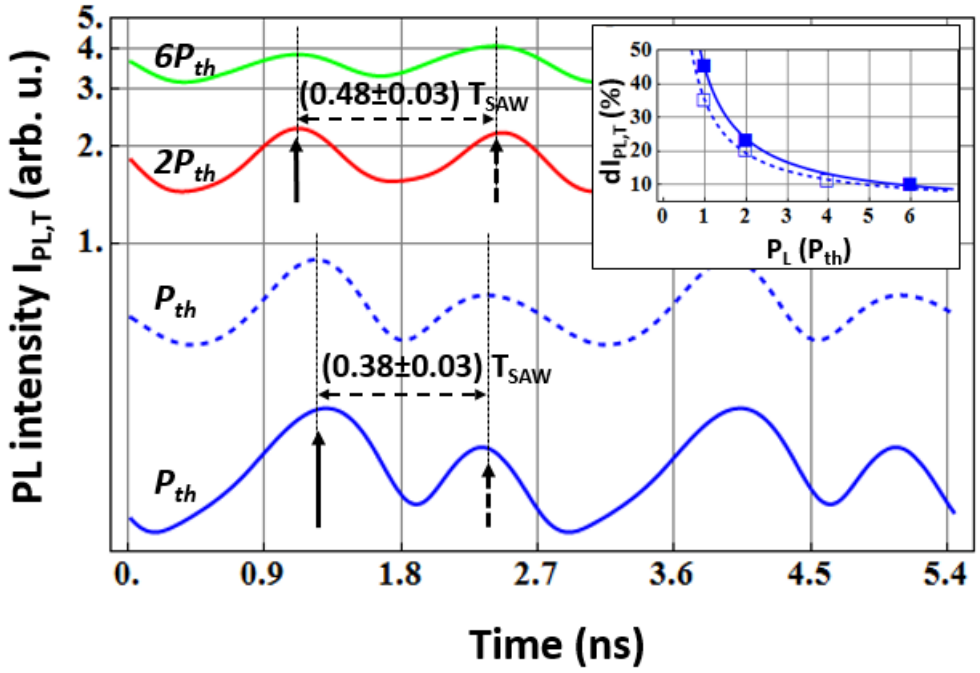

Figure 4.40: Time-resolved total PL intensity $I_{PL,T}$ for different laser powers (P_L stated in terms of P_{th}) recorded for laser spot sizes ϕ_L of 60 μm (solid curves) and 100 μm (dashed curve), [82]. The solid and dashed arrows mark the first and the second maximum of the PL intensity, respectively. The inset shows the dependence of the PL intensity variation $\Delta I_{PL,T}$ on the laser power P_L for $\phi_L = 60\,\mu m$ (solid curve) and $\phi_L = 100\,\mu m$ (dashed curve). The lines are fits to the expression discussed in the text.

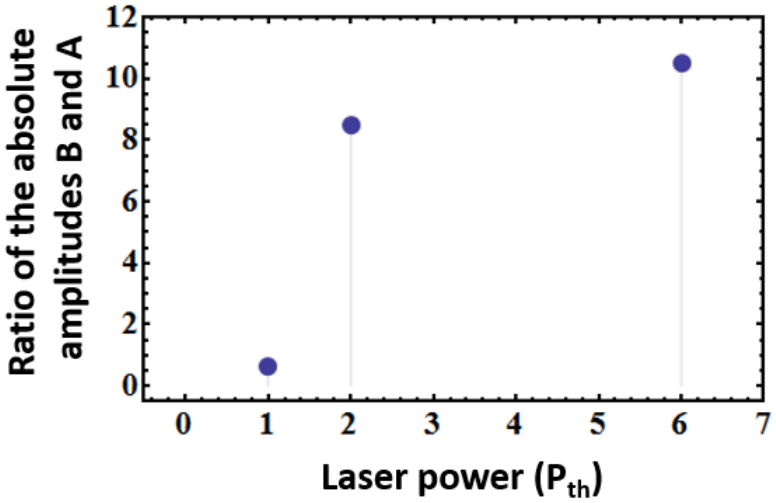

Figure 4.41: Ratio of the Fourier spectrum amplitudes A and B of the total PL emission intensity $I_{PL,T}$ of the 2D GS as a function of the laser power

Dependence of the total PL intensity on SAW amplitude

In order to clarify the origin of the PL oscillations $\Delta I_{PL,T}$, the dependence of the time-integrated PL intensity I_{PL} on the excitation power P_L as well as on the SAW amplitude Φ_{SAW} was measured. Results obtained for a spot diameter $\phi_L = 60\,\mu m$ are summarised in Fig. 4.42. I_{PL} strongly increases for $P_L > P_{th}$ and saturates for $P_L > 6\,P_{th}$. The saturation is attributed to the finite 2D GS size as well as to an increase in the energy blue-shift ΔE_{blue} of the polariton pump states with increasing polariton density, which reduces the injection efficiency above certain P_L [65]. The PL intensity also increases with the SAW amplitude. This behaviour can be understood by taking into account the non-linear dependence of the injection efficiency on ΔE_{blue}. In particular, more polaritons are injected when the energy of the pumping states red-shifts during half of the SAW cycle and thus, the resulting extra polariton density overcompensates the reduced injection during the subsequent SAW half cycle.

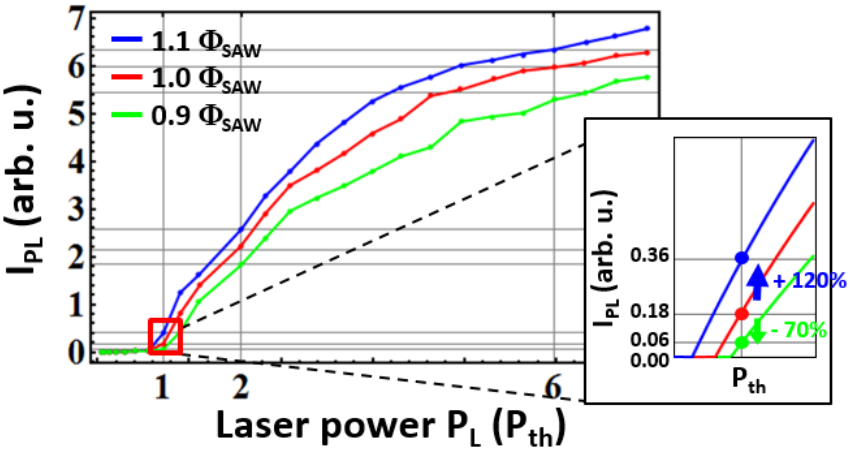

Figure 4.42: Dependence of the time-integrated PL intensity I_{PL} of the 2D GS on the laser power P_L and the SAW amplitude Φ_{SAW} for $\phi_L = 60\,\mu m$. $1.0\,\phi_{SAW}$ corresponds to the used RF-power of $30\,mW$ in the experiments presented in this Sec. The inset shows a zoom-up of the plot for the laser powers close to the 2D GS condensation threshold P_{th}. It shows that an increase of Φ_{SAW} by 10% enhances I_{PL} by 120% at the same PL. Furthermore, a decrease of Φ_{SAW} by 10% leads to a decrease of I_{PL} by 70%, [82].

The formation of a standing wave pattern due to SAW reflections together with the dependence of the emission intensity on SAW amplitude (cf. Fig. 4.42) provides a possible qualitative explanation for the oscillations in emission intensity at twice the SAW frequency f_{SAW} detected in the time-resolved images (cf. Fig. 4.38). The oscillations at $2\,f_{SAW}$ also account for the extra spatial periodicity observed in the time-integrated real-space image (cf. Chapter 3 Fig. 3.2(a)). Quantitative estimations of the magnitude of the PL oscillations can be extracted from the results in Fig. 4.42. At high optical excitation powers (i.e., in the saturation regime for

$P_L \geq 6\,P_{th}$), the data in Fig. 4.42 shows that the variation in PL intensity is roughly proportional to the SAW amplitude Φ_{SAW}. The peak-to-peak variation in acoustic amplitude of 5% due to the SAW reflections reported in Sec. 4.1 is then expected to induce a variation of approximately 5% in the time-resolved PL intensity $I_{PL,T}$. This oscillation amplitude compares well with the value $B = (3 + 1)\%$ previously determined for high excitation powers. These results for optical powers $P_L \gg P_{th}$ are also consistent with the spatial modulation of the time-integrated PL reported in [94]. Our time-resolved investigations also identified two further effects, which become pronounced for optical excitation powers close to the condensation threshold: a strong enhancement of the PL modulation intensity (cf. inset of Fig. 4.40) and the appearance of a strong modulation component at the SAW frequency. The first of these effects can also be understood based on the results of Fig. 4.42. Here, the relative changes in PL intensity increase considerably with decreasing optical excitation: the relative changes in PL intensity caused by a 1% variation of the SAW amplitude Φ_{SAW} vary from 1% at $P_L = 6\,P_{th}$ to 4% at $P_L = 2\,P_{th}$. Much more pronounced changes occur close to the condensation threshold due to its modulation by the SAW amplitude. Here, an increase of Φ_{SAW} by 1% results in an increase of PL intensity I_{PL} by more than 10%.

While SAW reflections alone readily explain the modulation at twice the SAW frequency, they cannot account for the asymmetric shape of the $I_{PL,T}$-profiles, especially for $P_L \simeq P_{th}$, which is caused by the appearance of a Fourier component at the fundamental SAW frequency (cf. Fig. 4.37). In the following, a mechanism to account for this behaviour is presented, which relies on the matching of the spatial phase of the acoustic square lattice and the laser spot.

4.3.3 Theoretical model

Dependence of $I_{PL,T}$-profiles on the lattice phase

Figures 4.43(a) and (b) show a schematic diagram of the position of the moving acoustic square lattice within a Gaussian laser spot exciting a 2D GS at two time instants $t = 0$ and $t = 0.5\,T_{SAW}$. For high laser powers P_L, the size of the 2D GS is large (red dashed circle) and encloses a larger number N_{pot} of SAW potential minima (green/green-white dots in Fig. 4.43(a) and (b)). The 2D GS luminescence properties are then weakly sensitive to the phase of the lattice within the excitation area. For small P_L, in contrast, the 2D GS size reduces (blue dashed circle) and its emission properties should change as the lattice moves across the laser spot. Obviously, N_{pot} depends on the relative spatial phase of the lattice with respect to the excitation spot. In order to estimate the magnitude of this effect in the absence of SAW reflections, the modulation of $I_{PL,T}$ was calculated under the following simplifying assumptions:
(i) the number of injected exciton-polaritons as well as the total PL intensity are linearly dependent on P_L;
(ii) the injection of exciton-polaritons is only possible within a radius of $\lambda_{SAW}/4$ around the N_{pot} lattice potential minima created by SAWs within the Gaussian excitation spot (i.e., radius of dot-like areas in Fig. 4.43(a));
(iii) the injection of exciton-polaritons is restricted to an area of diameter D_L, where the optical power density exceeds the condensation threshold. D_L corresponds to the diameter of the emission area and depends on the laser power P_L and the laser spot size ϕ_L. Physically, D_L is related to P_L and the 2D GS size.

Accordingly, the model equation can be summarised as follows:

$$I_{PL,T}(t) \propto \int_0^{\frac{D_L}{2}} \Phi_{SAW}(r)\, \exp\left(\frac{-r^2}{2\sigma^2}\right) r\, dr, \tag{4.3.4}$$

where the SAW potential is presented by $\Phi_{SAW}(r)$, where r has a time-dependence, i.e. $r = r(t)$. The Gaussian intensity profile of the laser spot is described by $\exp\left(\frac{-r^2}{2\sigma^2}\right)$. σ is related to the laser spot size ϕ_L by $\phi_L = 2\sqrt{2\,ln2}\sigma$.

The time dependence of $I_{PL,T}$ calculated for $D_L = 24\,\mu m$ and $D_L = 48\,\mu m$ with $\phi_L = 60\,\mu m$ is illustrated in Fig. 4.43(c). These calculations mimic experiments carried out with the smaller laser spot ($\phi_L = 60\,\mu m$) under optical excitation powers close to and above the condensation threshold P_{th}, respectively. An increase of D_L corresponds to an increase of P_L in the experiment. The model predicts a PL modulation amplitude $\Delta I_{PL,T}$ at the SAW frequency of $\pm 8\%$ (blue curve) around its average value, which reduces with increasing D_L (red curve). In addition, while the maximum PL intensity is at $t = 0.5\,T_{SAW}$ for $D_L = 24\,\mu m$ (blue curve), it shifts to $t = 0$ for $D_L = 48\,\mu m$ (red curve). This shift in phase reflects the fact that the lattice phase yielding the highest PL intensity varies with D_L. It is interesting

to note that due to the Gaussian excitation profile, the total PL intensity depends not only on the total number N_{pot} of lattice potential minima enclosed within the diameter D_L but also on their spatial arrangement within the illuminated area.

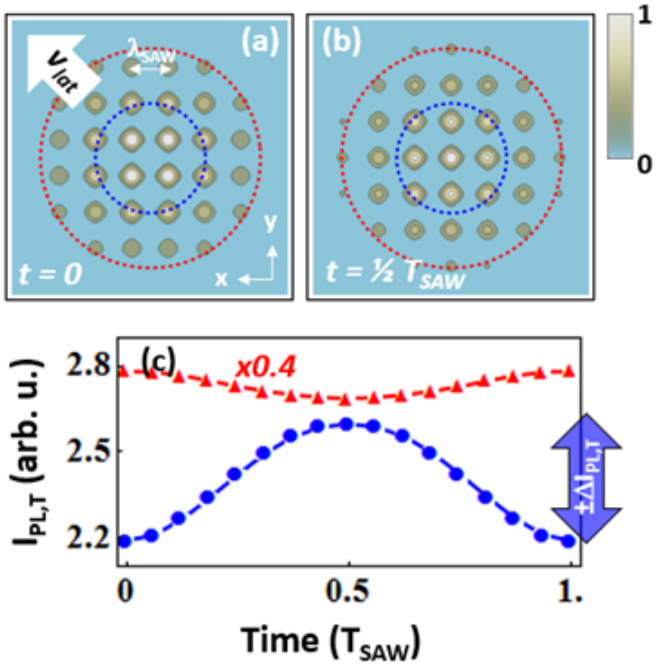

Figure 4.43: Panels (a)-(b) schematically show the SAW potential minima at $t = 0$ and at $t = 0.5\,T_{SAW}$ after the acoustic square lattice has moved by $0.5\,T_{SAW}\,v_{lat}$, [82]. The blue and red dashed circles have a diameter $D_L = 24\,\mu m$ $(= 3\,\lambda_{SAW})$ and $D_L = 48\,\mu m$ $(= 6\,\lambda_{SAW})$, respectively, and represent the effective area of the laser spot, where $P_L \geq P_{th}$. The centre of the laser spots coincides with the centre of the square lattice at $t = 0$ and $t = \frac{1}{2}T_{SAW}$. While the square lattice moves, as indicated by the white arrow, the spatial phase of the square lattice is changing with respect to the laser spot and thus, making the total PL intensity $I_{PL,T}$ to oscillate as (c) calculated for a laser spot with $\phi_L = 60\,\mu m$ and $D_L = 24\,\mu m$ (blue curve) and $D_L = 48\,\mu m$ (red curve). The "xN" label indicates the intensity magnification factor N with respect to the result for $D_L = 24\,\mu m$. For both cases, $I_{PL,T}$ varies with f_{SAW} around its time-averaged value. However, the variation $\Delta I_{PL,T}$ is bigger for the blue curve $(D_L = 24\,\mu m)$. As well, the phase of the blue curve is shifted by a half of the SAW period with respect to the red curve $(D_L = 48\,\mu m)$. The origin of the phase shift is discussed in the text.

Combined Effects of the SAW reflections and the lattice phase on $I_{PL,T}$-profile

The same model can also take into account the combined effects of SAW reflections and lattice phase matching, which is required to reproduce the shape of the time-resolved $I_{PL,T}$-profiles. For that purpose, it is assumed that SAW reflections change the amplitude of the acoustic square lattice by 5% (cf. Sec. 4.1). Results for different values of D_L and ϕ_L are displayed in Fig. 4.44(a). In all cases, the model yields two maxima and two minima per SAW period T_{SAW} in agreement the previous results as displayed in the Fig. 4.38(i). For $\phi_L = 60\,\mu m$ and $D_L = 24\,\mu m$ (blue curve), which corresponds to the experimentally determined 2D GS size at $P_L = P_{th}$ (cf. Fig. 4.38(a)-(d)), the main contribution to $I_{PL,T}$ arises from the phase matching mechanism. As a result, the calculated $I_{PL,T}$ displays a strong component at the SAW frequency. Furthermore, the comparison between the calculated results for $D_L = 24\,\mu m$ and $D_L = 48\,\mu m$ reveals that the strongest $I_{PL,T}$-maximum in Fig. 4.44(a) shifts by $0.5\,T_{SAW}$ reproducing the experimental results (cf. blue and green curve in Fig. 4.40, respectively). As pointed out by the Fig. 4.43, this is due to the fact that N_{pot} is bigger at $t = 0$ than at $t = 0.5\,T_{SAW}$ when $D_L = 24\,\mu m$, but the opposite is true when $D_L = 48\,\mu m$. When ϕ_L is increased to $100\,\mu m$ and $D_L = 32\,\mu m$ (experimentally determined 2D GS size at $P_L = P_{th}$ for $\phi_L = 100\,\mu m$), $\Delta I_{PL,T}$ reduces (red curve in Fig. 4.44(a)) but keeps the same temporal shape as obtained for the experimental conditions: $\phi_L = 60\,\mu m$ and $D_L = 24\,\mu m$.

Figure 4.44(b) shows the calculated relationship between $\Delta I_{PL,T}$ and D_L, which can be expressed as $\Delta I_{PL,T}(D_L) = (230 \pm 20)\%\,(D_L/\mu m)^{-1} + (1 \pm 1)\%$. When D_L is increased, the amplitude of the oscillations reduces and the profiles become dominated by the component at $2\,f_{SAW}$ (cf. Fig. 4.44(a)). These calculated results qualitatively reproduce the experimental behaviour shown in Fig. 4.40.
Note, however, that the calculated amplitudes are smaller than the measured ones. This discrepancy is attributed to the fact that the model does not take into account the non-linear dependence of the emission intensity on optical and acoustical excitation powers.

Finally, Figures 4.45(c) and (d) compare the experimental results obtained using a spot diameter $\phi_L = 60\,\mu m$ and optical powers of $P_L = P_{th}$ and $P_L = 6\,P_{th}$ with calculations performed for $D_L = 24\,\mu m$ and $D_L = 48\,\mu m$, respectively. These particular values for D_L were chosen because they approximately correspond to the dimensions of the emission area in the experiments. The experimental results have been scaled in intensity by constant factors to fit the calculated profiles. In the calculations, the position of the laser spot relative to the acoustic lattice and thus, to the standing SAW pattern, which determines the phase difference between the Fourier components at f_{SAW} and $2\,f_{SAW}$, was adjusted to match experimental results. Except for an overall scaling factor, the calculated profiles reproduce very well the experimental data. Despite its simplicity, the model can account for the temporal shape of the $I_{PL,T}$ as well as the dependence of $\Delta I_{PL,T}$ on P_L and ϕ_L.

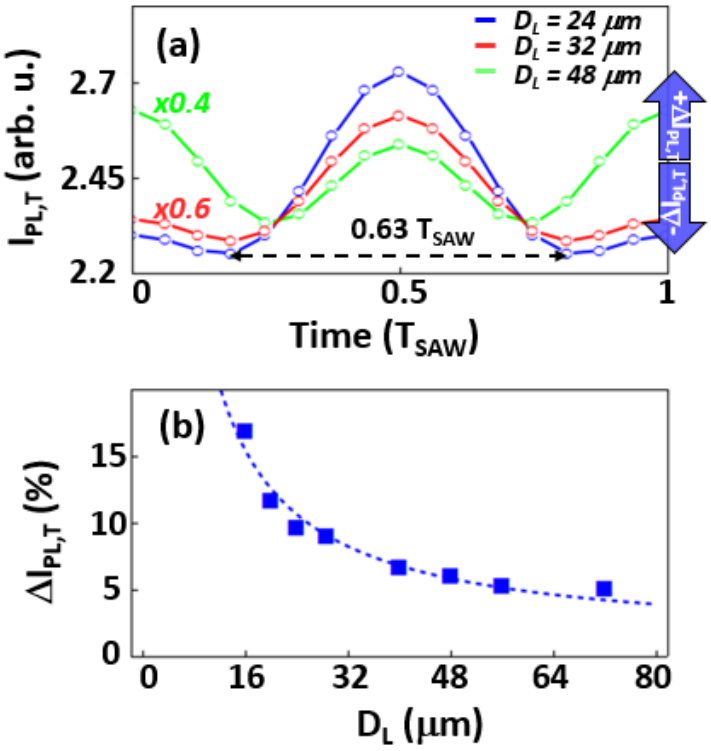

Figure 4.44: Calculated total PL intensity $I_{PL,T}$ considering SAW reflections and the changing spatial phase of the acoustic square lattice with respect to the laser spot. The parameter D_L was set to $24\,\mu m$ (blue curve) and $48\,\mu m$ (green curve) with $\phi_L = 60\,\mu m$ and $D_L = 32\,\mu m$ with $\phi_L = 100\,\mu m$ (red curve). The centre of the laser spots was placed at the centre of the square lattice at $t = 0$. The "xN" labels indicate the intensity magnification factor N with respect to the result for $D_L = 24\,\mu m$. $\Delta I_{PL,T}$ reduces with increasing D_L and/or ϕ_L. (b) Calculated dependence between $\Delta I_{PL,T}$ and D_L according to the model (adopted from [82]).

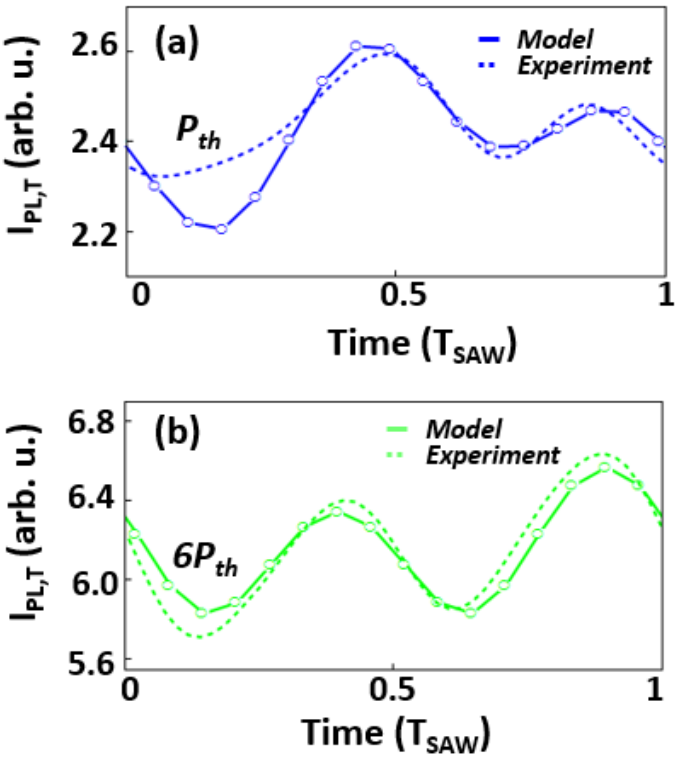

Figure 4.45: (a) and (b) show the comparison of the model with the experimental results for the excitation powers $P_L = P_{th}$ and $6\,P_{th}$, respectively. The experimental results have been scaled in intensity by constant factors to match the calculated ones (adopted from [82]).

Chapter 5

Summary and Conclusions

In this work, the structure and the dynamics of exciton-polariton condensates in moving acoustic square (2D) lattices have been investigated by spectrally-resolved cw- and time-resolved PL spectroscopy, respectively.

The tomographic study revealed that the exciton-polariton macroscopic quantum states (MQSs) self-organise in a structure, where three concentric modes coexist under excitation by a laser spot with a Gaussian intensity profile. The central mode is a single two-dimensional exciton-polariton gap soliton (2D GS) wavepacket reported in Ref. [75], which robustly forms over a large range of excitation parameters. The energy-filtered images review that the diameter $d_{2D\,GS}$ of the 2D GS emission is very close to the coherence length $L_{coh}^{2D\,GS}$ measured from reciprocal (k-) space images. While the total emission area d_{PL} of the MQSs is also equal to $d_{2D\,GS}$ and $L_{coh}^{2D\,GS}$ close to the threshold, it increases above these values for high excitation intensities. It was shown that the extra emission does not arise from multiple 2D GS states, but rather from multiple 1D MQSs with shorter coherence length excited at hyperbolic regions (X-points) of the dispersion. Additionally, it was shown that 2D GS has an intrinsic size.
The existence of 2D GS and 1D MQSs has been also been confirmed by a variational solution of the Gross-Pitaevskii equation for interacting polaritons in a square lattice.

Time-resolved studies of the 2D GS have revealed the spatial and temporal evolution of its wavefunction in a moving 2D lattice. The 2D GS PL intensity from the lattice oscillates at twice the SAW frequency in time or, equivalently, with the position of the lattice sites. The oscillation amplitude reaches several tens of %. The oscillations are attributed to the combined effects of SAW reflections, which modulate the potential of the acoustic square lattice, and the spatial phase matching between the lattice and the excitation laser spot. The main quantitative contribution to the PL intensity oscillations for excitation powers above the 2D GS condensation threshold is attributed to SAW reflections. SAW reflections are the origin of the PL intensity fluctuations at twice the SAW frequency. A model was developed to reproduce the time dependence of the 2D GS PL intensity oscillations on the intensity and size of the excitation laser spot. In addition to the PL intensity, it was

found that the spatial coherence of the 2D GS varies in time, which is due to the change of the spatial lattice phase.

In conclusion, the present studies provide an insight into the structure and dynamics of exciton-polariton MQSs in moving 2D lattices. The first broadens the fundamental understanding of self-localised exciton-polariton MQSs with a solitonic character, which may prove to be relevant for functionalities based on solitonic objects. The latter experimental results showed that it is possible to engineer polariton-based light emitting sources with intensity variations controllable by the SAWs.

Chapter 6

Outlook

This chapter is based on the publication [83] and gives an outlook about a possible development in the field of exciton-polaritons in the near future.

The development of new opto-electronic devices based on microcavity (MC) exciton-polariton operating at low threshold powers and at high switching frequencies is a complex and challenging task, which can only be overcome by exploiting new physical phenomena [95], [96], [97] and applying them to device implementations [98], [99]. As mentioned before, one of such new promising physical phenomenon are exciton-polaritons in semiconductor MC. Various polariton-based device concepts, like polariton-based transistors and logic gates, as well as their implementation in quantum information processing have been proposed [14], [100]. However, the fabrication of polaritonic devices requires reliable and practical potentials for controlling, confining and guiding exciton-polaritons in MC structure. One interesting option is provided by dynamic strain potentials induced by SAWs [101]. Since the SAW penetration depth is comparable to λ_{SAW}, an efficient acoustic modulation requires that λ_{SAW} is larger than the thickness of the upper MC DBRs. This limitation can be overcome by exploiting plasmonic resonances induced by thin metallic structures deposited on the top of the MC structure. In this case, new quasi-particles called Tamm-Plasmon/Exciton-Polaritons (TPEP) form by the superposition of Tamm plasmons (TPs) at the metal-semiconductor interface and the exciton-polaritons in the MC [55]. Furthermore, TP states can be used to mediate the strong coupling between photonic modes and QW excitons resulting in the formation of parametric TPEP states [83]. Such structures open the way to confine exciton-polaritons laterally, to guide them, to create potential barriers of several meV for them and at the same time to modulate them with SAWs at high frequencies, i.e. in the GHz range.

6.1 Tamm-Plasmon/Exciton-Polariton (TPEP)

6.1.1 Sample design and numerical studies

The proposed MC structure supporting TPEP states consists of a gold (Au) layer on top of the upper DBR of a MC structure (cf. Fig. 6.1(a)), which is very similar

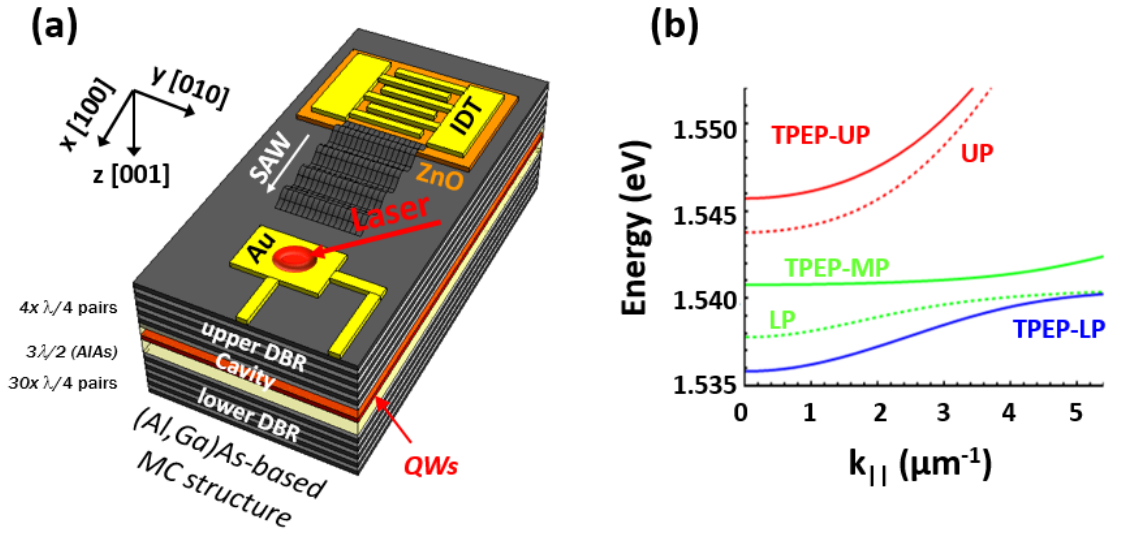

Figure 6.1: (a) Scheme of the proposed MC structure supporting the formation of TPEP states; sample A: 50 nm gold layer, 21 upper $\frac{1}{4}\lambda_C$ DBR pairs, $\frac{3}{2}\lambda_C$ cavity with 6 QWs and 30 lower $\frac{1}{4}\lambda_C$ DBR pairs for formation of TPEP states, where $\lambda_C = 805\,nm$ is the MC resonance wavelength. The QW exciton energy is in resonance with the TP and the MC mode. Structure of sample B is similar to sample A differing by: 30nm gold layer, 4 upper $\frac{1}{4}\lambda_C$ DBR pairs and $\lambda_C = 780\,nm$. (b) Calculated TPEP states (solid lines) due to the strong coupling of the TP mode, MC mode and QW excitons according to Eq. 6.1.1 as well as calculated exciton-polariton lower (LP) and upper (UP) states (dashed lines). The lower (TPEP-LP), the middle (TPEP-MP) and upper (TPEP-UP) states are shown. The calculations have been performed for the sample structure A.

to the one investigated in the experimental part of this work (cf. Fig. 2.13(a)). To remind the reader, the upper DBR consists of $Al_xGa_{1-x}As$ layers with a thickness of $\lambda_C/(4n_i)$, where x alternates between 0.15 and 0.8, n_i is the refractive index of the DBR layers and λ_C is the wavelength of the MC mode. Importantly, the MC structure supports TP modes at the metal-semiconductor interface only when the DBR layer adjacent to the metal has a higher refractive index than its following one [54]. Note, in contrast to Surface Plasmons (SPs) TP modes can be excited either with s- or p-polarised light at any wavevector k [103], [97]. However, they exist only within the cone of the excitation light. Furthermore, TP modes have a parabolic dispersion with an effective mass of $\sim 10^{-5}m_e$, where m_e is the electron rest mass, and their energy E_T can be tuned by changing the thickness of the metal and/or of the adjacent DBR layer [54].
When E_T is in resonance with the MC mode and the QW exciton energy, the resulting coupled system can be described using the three level coupled oscillator model given by:

$$\hat{H} = \begin{pmatrix} E_T & \frac{\hbar\Omega_{T-C}}{2} & 0 \\ \frac{\hbar\Omega_{T-C}}{2} & E_C & \frac{\hbar\Omega_{C-X}}{2} \\ 0 & \frac{\hbar\Omega_{C-X}}{2} & E_X \end{pmatrix}, \tag{6.1.1}$$

where E_T, E_C and E_X are the uncoupled eigenenergies of the TP mode, the MC mode and the QW excitons, respectively. The solution of the Schrödinger equation $\hat{H}|\Psi\rangle = E|\Psi\rangle$ yields the eigenstates and -energies of the TPEP modes, which are the linear combinations of the TP mode $|T\rangle$, MC mode $|C\rangle$ and QW exciton $|X\rangle$:

$$|\Psi\rangle = \alpha\,|T\rangle + \beta\,|C\rangle + \gamma\,|X\rangle. \tag{6.1.2}$$

α, β and γ are the corresponding Hopfield coefficients. There are three TPEP-states: the lower TPEP-state (TPEP-LP), the middle TPEP-state (TPEP-MP) and the upper TPEP-state (TPEP-UP) (cf. Fig. 6.1(b)). Each of them separated by $6\,meV$ since in the calculations using Eq. 6.1.1 it was assumed: $\hbar\Omega_{T-C} = \hbar\Omega_{C-X} = 6\,meV$.

The coupling strengths between the TP state and the MC mode (Ω_{T-C}) and between the MC mode and the QW excitons (Ω_{C-X}) determine, besides the Rabi-splitting, the mixing of these states in the TPEP modes. Ω_{T-C} is given by [55]:

$$\Omega_{T-C} \approx \frac{\sqrt{2}(n_2/n_1)^N(n_1-n_2)}{\pi\sqrt{n_1(2n_1-n_2)}}\omega_{DBR}, \tag{6.1.3}$$

where ω_{DBR} is the Bragg frequency of the upper DBR. Ω_{T-C} decreases exponentially with the number N of the upper DBR layers, whereas Ω_{C-X} is well approximated by Eq. 2.3.13. In Eq. 6.1.1, the direct coupling between excitons and TP states is neglected. However, since the amplitude of the electric field E_z of the TP mode strongly decays into the MC structure [107] and the QWs are positioned several DBR pairs below the metal, the latter approximation is reasonable.

When all states are in resonance and the coupling strengths are equal, i.e. $\Omega_{T-C} = \Omega_{C-X}$, then $\alpha = \beta = \gamma$. For the $Al_xGa_{1-x}As$/GaAs structures (cf. Fig. 6.1(a)), numerical studies based on a transfer matrix calculations show that it can only be achieved by using a relatively thick upper DBR (21 pairs of $\lambda_C/(4n_i)$-thick layers) to ensure that $\Omega_{T-C} \approx \Omega_{C-X}$. $\hbar\Omega_{C-X}$ is assumed to be of a few meV in accordance with the Rabi-splitting of the experimentally investigated MC structure. Figure 6.1(b) shows the TPEP dispersion of a MC structure satisfying this condition (cf. Fig. 6.1(a), structure A described in the caption).

Figure 6.2(a) shows the calculated reflectivity spectrum of the TPEP states for a MC structure with 21 upper DBR pairs and $50\,nm$ Au at $T = 10\,K$ using a transfer matrix method. A thick Au layer is necessary in order to confine the SAW strain field maximum at the depth of the QWs and thus, to increase SAW induced modulation of TPEP states. This is possible because the SAW velocity v_{SAW} in Au is smaller than in $Al_xGa_{1-x}As$ layers. In analogy to the core-cladding effect in optical fibers,

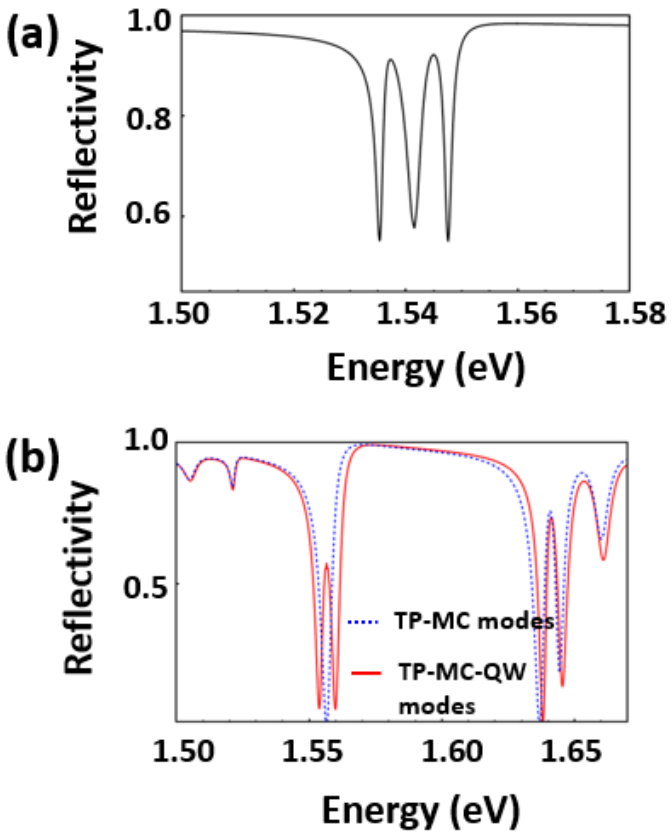

Figure 6.2: Calculated reflectivity spectrum of the TPEP states of (a) a MC structure A with 21 upper DBR pairs and (b) of the MC structure B with 4 upper DBR pairs (red solid line). The dashed blue line shows the reflectivity spectrum of the coupled TP mode and MC mode without any presence of QW excitons in the MC active region.

the SAWs tends to stay in the region and close to the region of low v_{SAW} [48], [105], [106]. The linewidth of the TPEP states is $2.5\,meV$ and is limited by the absorption of the gold layer and its finite reflectivity. The Rabi-splitting between lower and upper TPEP mode is $12\,meV$ and $6\,meV$ between the lower/upper and middle TPEP mode. However, since the upper DBR is "very" thick, the efficient modulation of TPEP states by SAWs requires λ_{SAW} of around $8\,\mu m$ [83]. Thus, the modulation frequency is $f_{SAW} = 370\,MHz$. The corresponding maximal total modulation ΔE_{GCT} is calculated to be $\pm 3.2\,meV$ for the linear SAW power density $P_{SAW} = 300\,W/m$ (P_{SAW} is the SAW power per unit length perpendicular to the propagation direction). The main contribution to ΔE_{GCT} arises from the modulation of the bandgap energy of the QWs excitons ($\Delta E_G = 2.5\,meV$). The modulation ΔE_C of the MC mode energy is around $\pm 0.6\,meV$ and the modulation ΔE_T of the TP energy is around $\pm 0.1\,meV$. The origin of ΔE_T lies in the change of the thickness of the metal layer as well as of the upper DBR layers.

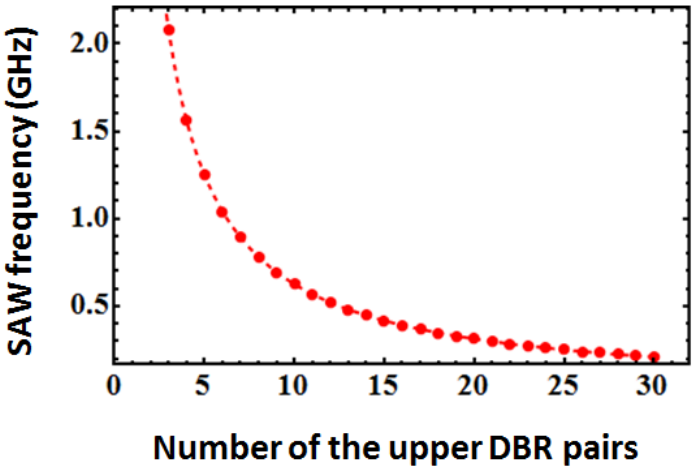

Figure 6.3: Dependence of the optimal SAW frequency f_{SAW} on the number N of upper $\lambda_C/(4n_i)$-thick DBR pairs of the MC structure (cf. Fig. 6.1(a)) for maximal modulation by SAWs. For f_{SAW} in the GHz range, the condition $N \leq 6$ is required.

6.1.2 Parametric TPEP modes

In order to achieve larger modulation frequencies f_{SAW} in the GHz range, i.e. shorter λ_{SAW}, and bigger ΔE_{GCT}, the above proposed MC structure needs to modified to a structure with a reduced number N of upper DBR pairs (structure B described in the caption of Fig. 6.1(a)) [83]. f_{SAW} in the GHz range is only feasable, if the total number N of the upper DBR pairs, i.e. pairs of $\lambda_C/(4n_i)$-thick layers, is $N \leq 6$ as shown in the Fig. 6.3.

In the design of the MC structure B (cf. caption of Fig. 6.1), the energies of the TP and the MC modes were tuned in resonance, i.e. $E_T = E_C$, and the QW exciton energy E_X is shifted by $-\hbar\Omega_{T-C}/2$ with respect to $E_{T/C}$, i.e. $E_X = E_{T/C} - \frac{\hbar\Omega_{T-C}}{2}$. Thus, first the TP and MC modes strongly couple with each other resulting in the formation of the upper and lower optical branches (TC) with the Rabi-splitting Ω_{T-C}. Figure 6.2(b) shows the numerical results of the coupling between the two optical modes (blue dashed line). $\hbar\Omega_{T-C}$ amounts $80\,meV$ and is huge in comparison to $\hbar\Omega_{C-X}$. Furthermore, the energy of the lower TC mode, i.e. $E_{T/C} - \frac{\hbar\Omega_{T-C}}{2}$, is in resonance with the energy E_X of the QW excitons. Thus, the lower TC branch strongly couples to the QW excitons. This results in the formation of exciton-polariton states mediated by strongly optically coupled TP and MC modes which can be seen as parametric TPEP modes (cf. Fig. 6.2(b)). In this case, the TPEP modes are parametric since the TC modes oscillate with Ω_{T-C} between the lower and upper TC branch and thus, the formation of exciton-polaritons is driven by variation of the TC modes.

The advantage of the MC structure B over structure A is the larger Rabi-splitting

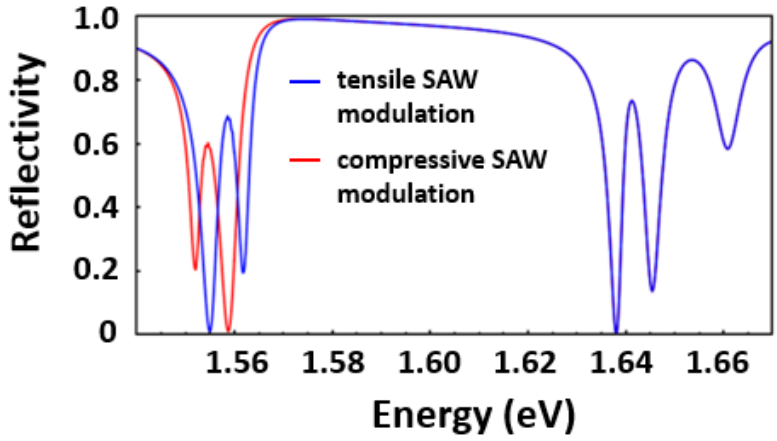

Figure 6.4: Calculated reflectivity spectra of MC structure B under acoustic modulation introduced by SAW with a power density $P_{SAW} = 300\,W/m$ at $f_{SAW} = 1.4\,GHz$. The reflectivity dips above $1.64\,eV$ represent the DBR stop band. There is no modulation of the upper TPEP state at $1.637\,eV$.

Ω_{T-C}, the reduced light absorption by the gold layer and the possibility of applying SAWs at gigahertz frequencies for the modulation of the TPEP modes. Figure 6.4 displays the calculated acoustic modulation of TPEP states for the MC structure B at SAW frequency of $1.4\,GHz$, i.e. $\lambda_{SAW} = 2\,\mu m$. SAWs creating compression in the MC structure shift the TPEP states to higher energies (red curve in Fig. 6.4), whereas tensile strain induced by the SAWs affects more the lower TPEP state. This is due to an increase of the QW bandgap energy ΔE_G as well as of ΔE_C and ΔE_T if compressive strain is applied on the MC structure and to a decrease of ΔE_G, ΔE_C and ΔE_T in the case of the tensile strain [102]. Since $\Delta E_{GCT} \ll \hbar\Omega_{T-C}$, the acoustic modulation mainly influences the lower and middle TPEP states, where the modulation of the excitonic component is of the same order of magnitude as the Rabi-splitting, $\Delta E_{GCT} \approx \hbar\Omega_{C-X}$. The maximal SAW induced modulation is $\pm 4\,meV$, which bigger than the linewidth of the TPEP modes ($4\,meV$).

Bibliography

[1] H. Simon, The Oxford Solid State Basics, Oxford University Press (2013)

[2] P. Yu and M. Cardona, Fundamentals of Semiconductors, Springer Verlag (2010)

[3] V. Jain and A. Verma, Physics of Semiconductor Devices, Springer Verlag (2014)

[4] W. Chow and S. Koch, Semiconductor-Laser Fundamentals: Physics of the Gain Materials, Springer Verlag (1999)

[5] S. Adachai, GaAs and Related Materials: Bulk Semiconducting and Superlattice Properties, World Scientific Publishing (1994)

[6] C. J. Hwang et al., Phys. Rev. B 8, 646 (1973)

[7] H. Deng et al., Rev. Mod. Phys. 82 (2010)

[8] D. Munzar et al., Phys. Status Solidi (b) 175, 395 (1993)

[9] J. Blakemore, Gallium Arsenide, American Institute of Physics (1987)

[10] F. Peters et al., Electron. Lett. 29, 200 (1993)

[11] K. Iga, IEEE J. Sel. Top. Quantum Electron. 6, 1201 (2000)

[12] C. Schneider et al., Nature 497, 348 (2013)

[13] S. Christopoulos et al., Phys. Rev. Lett. 98, 126405 (2007)

[14] D. Ballarini et al., Nat. Commun. 4, 1778 (2013)

[15] K. Vahala et al., Nature 424, 839 (2003)

[16] F. Ding et al., Phys. Rev. B 87, 161116 (2013)

[17] H. Macleod, Thin-Film Optical Filters, Institute of Physics Publishing (2001)

[18] C. Sheppard, Pure Appl. Opt. 4, 665 (1995)

[19] M. Skolnick et al., Semicond. Sci. Technol. 13, 645 (1998)

[20] J. Gerard et al., Phys. Rev. Lett. 81, 1110 (1998)

[21] P. Dirac, Proceedings of the Royal Society A 114, 243 (1927)

[22] D. Englund et al., Phys. Rev. Lett. 95, 013904 (2005)

[23] P. Michler, Single semiconductor quantum dots, Springer Verlag (2009)

[24] E. Purcell, Phys. Rev. 69, 681 (1946)

[25] J. Hopfield, Phys. Rev. 112, 1555 (1958)

[26] V. Savona et al., Solid State Commun. 93, 733 (1995)

[27] L. Andreani et al, Superlattices Microstruct. 15, 453 (1994)

[28] E. Raab et al., Phys. Rev. Lett. 59, 2631 (1987)

[29] C. Foot, Atomic Physics, Oxford University Press (2005)

[30] E. Daif et al., Appl. Phys. Lett. 88, 061105 (2006)

[31] K. Winkler et al., New J. Phys. 17, 023001 (2015)

[32] E. Cerda-Mendez et al., Phys. Rev. B 86, 100301 (2012)

[33] D. Tanese et al., Nat. Commun. 4, 1749 (2013)

[34] L. Landau and E. Lipshitz, Course of Theoretical Physics: Theory of elasticity, Pergamon Press (1959)

[35] M. Sadd, Elasticity: Theory, Applications and Numerics, Elsevier Inc. (2005)

[36] J. Nye, Physical Properties of Crystals, Oxford University Press (1957)

[37] B. Auld, Acoustic Fields and Waves in Solids, Krieger Publishing Company (1990)

[38] T. Aono et al., Phys. Rev. B 58, 4838 (1998)

[39] H. Morkoc and Ü. Özgür, Zinc Oxide: Fundamentals, Materials and Device Technology, Wiley-VCH Verlag (2009)

[40] D. Royer and E. Dieulesaint, Elastic Waves in Solids, Springer Verlag (2000)

[41] I. Sayago et al., Synth. Mater. 148, 37 (2005)

[42] K. A . Ingebrigtsen, J. Appl. Phys. 40, 2681 (1967)

[43] S. Rupp, Hochempfindliche Oberflächenwellen-Sensoren für die Medizinische Diagnostik, PhD Thesis, Ruprecht-Karls-Universität Heidelberg (2004)

[44] E. Dieulesaint and D. Royer, Elastic Waves in Solids, Wiley-VCH Verlag (1980)

[45] A. A. Oliner, Acoustic Surface Waves, Springer Verlag (1978)

[46] S. Hatch, Surface Acoustic Waves on Piezoelectric Media - Applications to Acoustic Charge Transport, B.Sc. Thesis, University of Western Australia (2000)

[47] T. Aono and S. Tamura, Phys. Rev. B 58, 4838 (1998)

[48] M. M. de Lima et al., Rep. Prog. Phys. 68, 1639 (2005)

[49] M. Cardona et al., Phys. Rev. B 35, 6182 (1987)

[50] R. Mair et al., Phys. Lett. A 239, 277 (1998)

[51] E. Cerda-Mendez et al., Physica E 42, 2548 (2010)

[52] L. Milstein and P. Das, IEEE Communications Magazine 17, 25 (1979)

[53] D. Pozar, Microwave Engineering, Third Edition, John Wiley and Sons (2005)

[54] M. Kaliteevski et al., Phys. Rev. B 76, 165415 (2007)

[55] M. Kaliteevski et al., Appl. Phys. Lett. 95, 251108 (2009)

[56] J. Gessler et al., Appl. Phys. Lett. 105, 181107 (2014)

[57] J. Kasprzak et al., Nature 443, 409 (2006)

[58] L. S. Dang et al., Phys. Rev. Lett. 81, 39203923 (1998)

[59] J. Bloch et al., Phys. Rev. B 71, 155311 (2005)

[60] M. Richard et al., Phys. Rev. Lett. 94, 187401 (2005)

[61] S. Schmitt-Rink et al., Phys. Rev. B 32, 6601 (1985)

[62] S. Schmitt-Rink et al., Adv. Phys. 38, 89188 (1989)

[63] L. Andreani et al., Phys. Rev. B 41, 7536 (1990)

[64] C. Schindler et al., Phys. Rev. B 78, 045313 (2008)

[65] A. Kavokin and J. Baumberg, Microcavities, Oxford University Press (2011)

[66] P. Savvidis et al., Phys. Rev. Lett. 84, 1547 (2000)

[67] D. Sanvitto and V. Timofeev, Exciton Polaritons in Microcavities: New Frontiers, Springer Verlag (2012)

[68] A. Kavokin and G. Malpuech, Thin Films and Nanostructures: Cavity Polaritons, Elsevier Inc. (2003)

[69] R. Butté et al., Phys. Rev. B 68, 115325 (2003)

[70] E. Cerda-Mendez et al., Phys. Rev. Lett. 105, 116402 (2010)

[71] T. Byrnes et al., Nat. Phys. 10, 803 (2014)

[72] E. Cerda-Mendez et al., New J. Phys. 14, 075011 (2012)

[73] E. Cerda-Mendez et al., AIP Conf. Proc. 1399, 1031 (2011)

[74] D. N. Krizhanovskii et al., Phys. Rev. B 87, 155423 (2013)

[75] E. Cerda-Mendez et al., Phys. Rev. Lett. 111, 146401 (2013)

[76] B. Eiermann et al., Phys. Rev. Lett. 92, 230401 (2004)

[77] W. Heisenberg, Z. Phys. 43, 172 (1927)

[78] K. Li, Springer Series in Synergetics 61, 245 (1994)

[79] G. Amelio et al., Bell Syst. Tech. J. 49, 593 (1970)

[80] G. Nardin et al., Appl. Phys. Lett. 94, 181103 (2009)

[81] J. V. T. Buller et al., New J. Phys. 18, 073002 (2016)

[82] J. V. T. Buller et al., Phys. Rev. B 94, 125432 (2016)

[83] J. V. T. Buller et. al., Acta Physica Polonica A 129, A-26 (2016)

[84] A. C. Berceanu et al., Phys. Rev. B 92, 035307 (2015)

[85] I. Carusotto and C. Ciuti, Rev. Mod. Phys. 85, 299 (2013)

[86] D. M. Whittaker, Phys. Status Solidi (c) 2, 733 (2005)

[87] J. Rogel-Salazar, Eur. J. Phys. 34, 247 (2013)

[88] L. P. Pitaevskii, Sov. Phys. JETP 13(2), 451 (1961)

[89] S. Das, Int. J. Mod. Phys. D 24, 1544001 (2015)

[90] C. J. Pethick and H. Smith, Bose-Einstein Condensation in Dilute Gases, Cambridge University Press (2001)

[91] L. P. Pitaevskii and S. Stringari, Bose Einstein Condensation, Oxford University Press (2003)

[92] E. A. Ostrovskaya et al., Phys. Rev. Lett. 90, 160407 (2003)

[93] X. Wang et al., Phys. Rev. Lett. 99, 243901 (2007)

[94] J. K. Chana et al., Phonon assisted polariton scattering in semiconductor microcavities subjected to surface acoustic waves, unpublished

[95] L. Novotny and B. Hecht, Principles of Nano-Optics, Cambridge University Press (2006)

[96] A. Amo et al., Nat. Phys. 5, 805 (2009)

[97] K. G. Lagoudaki et al., Nat. Phys. 4, 706 (2008)

[98] S. Maier, Plasmonics: Fundamentals and Applications, Springer Verlag (2007)

[99] T. C. H. Liew et al., Phys. Rev. B 82, 033302 (2010)

[100] I. M. Georgescu et al., Rev. Mod. Phys. 86, 153 (2014)

[101] X. Ben et al., Appl. Phys. Lett. 102, 041909 (2013)

[102] J. Novak et al., Appl. Phys. Lett. 79, 2758 (2001)

[103] R. H. Ritchie, Phys. Rev. 106, 874 (1957)

[104] E. Ozbay et al., Science 311, 189 (2006)

[105] C. Yeh, Handbook of Fiber Optics, Academic Press (1990)

[106] D. Gloge, Appl. Opt. 10, 2252 (1971)

[107] G. Lheureux et al., SPIE Newsroom (2013)